UNIVERSITY
OF TRENTO - Italy
DEPARTMENT OF INDUSTRIAL ENGINEERING

Doctoral School in Materials, Mechatronics and Systems Engineering

Polymer composites for sustainable 3D printing materials

Rigotti Daniele

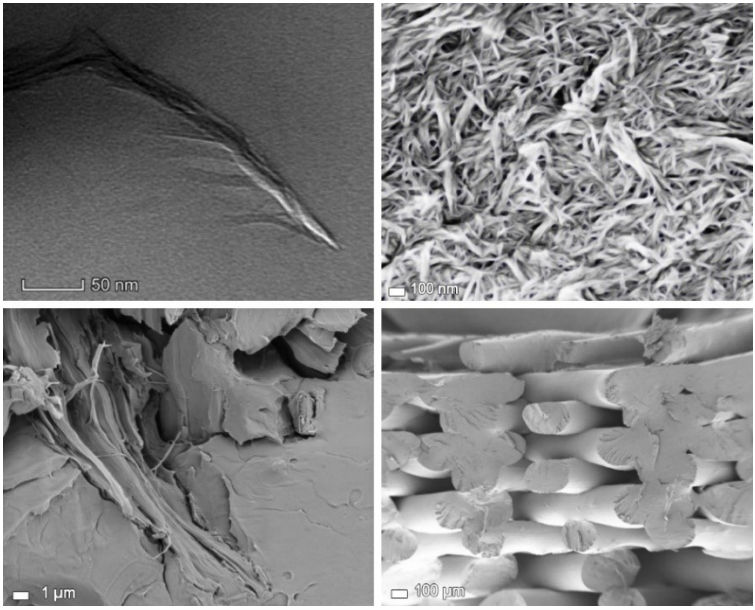

October 2019

POLYMER COMPOSITES FOR SUSTAINABLE 3D PRINTING MATERIALS

Rigotti Daniele

E-mail: daniele.rigotti-1@unitn.it

Approved by:	Ph.D. Commission:
Prof. Alessandro Pegoretti, Advisor Department of Industrial Engineering *University of Trento, Italy.* Prof. Luca Fambri, Advisor Department of Industrial Engineering *University of Trento, Italy.*	Prof. Katharina Resch-Fauster, Department of Department Polymer Engineering and Science *University of* Montanuniversitaet Leoben*, Austria.* Prof. Gerald Pinter Department of Department Polymer Engineering and Science *University of* Montanuniversitaet Leoben*, Austria.* Prof. Massimo Messori, Department of Engineering "Enzo Ferrari" University of Modena and Reggio Emilia, Italy Prof. Andrea Dorigato, Department of Industrial Engineering *University of Trento, Italy.*

University of Trento,
Department of Materials, Mechatronics and Systems Engineering.

October 2019

University of Trento - Department of
Materials, Mechatronics and Systems Engineering

Doctoral Thesis

Rigotti Daniele - 2019
Published in Trento (Italy) – by University of Trento

I want to say one word to you. Just one word.

Yes, sir.

Are you listening?

Yes, I am.

Plastics.

Exactly how do you mean?

There's a great future in plastics. Think about it. Will you think about it?

Conversation between Mr. McGuire and Benjamin Braddock
in "The Graduate" 1967

Cover image from top left clockwise: TEM picture of lauryl functionalized nanocellulose, SEM image of nanofibrillated cellulose, SEM image of 3D printed PLA, SEM image of microcellulose in PLA grafted maleic anhydride.

Abstract

Biodegradable and bio-based polymers have raised great attention since sustainable development policies tend to become more and more important with the growing concern for the environment and the decreasing reserve of fossil fuel [1]. The increasing demand for environmentally friendly materials attracted the attention on biopolymers reinforced with cellulose, that is a virtually inexhaustible source of raw material [2] and on new manufacturing ways such as additive manufacturing (AM) [3]. The most diffused AM technology for polymers is Fused Deposition Modelling (FDM), a technique where a filament of thermoplastic polymer is extruded through a nozzle and deposited layer by layer to form the final object with the support of computer aided design.

The aim of this work is the development of different kind of thermoplastic biodegradable composites based on commercially available polymers reinforced with cellulose and to study their applicability in fused deposition modeling (FDM). The final goal is the production of plastic filaments suitable to feed a commercially available FDM 3D-printing machine.

Starting from microcrystalline cellulose (MCC), two different types of nanocellulose: crystalline nanocellulose (CNC) and nanofibrillated cellulose (NFC) were produced and studied to be applied as natural reinforcing fillers for selected types of biopolymers. Cellulose nanocrystals in water solution were prepared from micro-cellulose through a sulfuric acid hydrolysis while the fibrillated nanocellulose was obtained with high energy ultrasonication. The commercial grade polymer matrices selected in this research were:

i. polyvinyl alcohol (PVA), a water-soluble biodegradable material;
ii. poly(lactic acid) (PLA), a biodegradable polymer that comes from the fermentation of agricultural waste;
iii. poly(3-hydroxybutyrate-co-3-hydroxyhexanoate) (PHBH) that belongs to the family of polyhydroxyalkanoates (PHA) and it is entirely synthesized by microorganism as an intracellular storage product under particular growth conditions.

Composite materials containing various amounts of cellulose fillers produced by solution or melt mixing were grinded and extruded through a single screw extruder to

obtain filaments. With the aid of a desktop 3D printer, dumbbell specimens were fabricated, and their mechanical properties determined. Several characterization techniques were used in order to assess the effect of micro- and nanocellulose on the physical and thermo-mechanical behavior of these thermoplastic composites.

According to SEM analysis, CNC particles appear homogeneously dispersed in PVA without noticeable aggregates. Thermal degradation of PVA was shifted towards higher temperatures with the increase of filler content, enhancing the thermal stability of the composites as compared with neat PVA. An enhancement in the storage modulus with the amount of CNC was observed in both filament and 3D printed specimens. In particular, an increase of about three times in the storage modulus at room temperature was reached in 3D samples with a CNC concentration of 10wt%. An improvement of the dimensional stability was observed with a reduction of the creep compliance with the filler content. Quasi-static tensile tests evidenced an increase of the stiffness and the strength of PVA due to the CNC introduction. A comparison between the reinforcing effect of nanocellulose and microcellulose in 3D printed samples highlighted the higher efficiency of CNC over MCC in reducing the rubber-like behavior of polyvinyl alcohol.

Maleic anhydride (MAH) was employed to improve the interaction between hydrophilic microcrystalline cellulose and the PLA matrix. Infrared spectroscopy confirmed the grafting of maleic anhydride on the PLA backbone during melt mixing and SEM analysis revealed that microcellulose was well dispersed in PLA and maleic anhydride was able to enhance the interface between the two components. Thermal degradation of PLA was not affected by the presence of MAH. On the other hand, glass transition temperature, crystallization temperature and melting temperature were lowered by the increasing amount of MAH. Glass transition temperature at 10wt% of MAH decreased from 70°C to 48°C. Tensile tests highlighted that microcellulose in low concentration was able to improve the stiffness and the stress at break of 3D printed specimens. The maximum in term of stiffness and strength is reached for composite at 1wt% of MCC and at 5 wt% with the presence of MAH.

NFC was dispersed in PLA by solution mixing and nanocomposites were printed and characterized. The creep compliance curves of the 3D printed samples were well fitted by a power law model and resulted that NFC was able to reduce the time-dependent linear response under constant load conditions, improving the geometrical stability. Static tensile test on plates obtained by solution casting displayed an increase in stiffness of the filament samples with increasing amount of nanocellulose. The same

effect was not observed on 3D printed samples where a poor adhesion between subsequent layers was evidenced from SEM analysis upon the introduction of NCF.

Lauryl functionalized nanocellulose was incorporated in PLA with solution mixing technique but the limited quantity of materials did not permit to go further with the production of filaments. Scanning electron microscopy indicated that up to a filler content of 6.5 wt. %, LNC was well dispersed. Nanocomposites with 3 and 5 wt. % of LNC showed the highest strain at break and a large amount of plastic deformation due to a strong interfacial adhesion between the PLA and filler particles while for higher LNC fractions the presence of aggregates weakened the nanocomposite. A decrease in stiffness was measured upon the introduction of LNC related to the low stiffness of the short aliphatic chains attached to the surface of the cellulose and so the formation of a soft phase between filler and the matrix as highlighted also by gas permeability tests.

Finally, poly(3-hydroxybutyrate-co-3-hydroxyhexanoate) was successfully extruded and 3D printed. PHBH and NCF were mixed in solution and extruded in form of filaments used to feed a 3D printing machine. The reinforcing effect of the nanocellulose in terms of stress at break and of elongation at break showed a maximum at a content of 0.5 wt%. An increase in stiffness for filament with increasing amount of nanocellulose was measured but also in this case it was not observed in 3D printed samples. Anyway, the presence of NCF did not affect the thermal behavior of the materials.

Table of contents

List of abbreviation and acronyms

Ø	Permeability
3DP	3D printing
3HB	3 hydroxybutyrate
3HH	3 hydroxyhexanoate
A	Absorptance
ABS	Acrylonitrile-styrene-butadiene
AFM	Atomic force microscopy
AGU	Anhydroglucose unit
AM	Additive manufacturing
CAD	Computer aided design
$CHCl_3$	Chloroform
CMM	Coordinate Measuring Machines
CNC	Crystalline nanocellulose
CO_2	Carbon dioxide
D	Creep compliance
D	Diffusivity
D_2	Deuterium
DCP	Dicumyl Peroxide
DLP	Digital light processing
DMA	Dynamic Mechanical Analysis
DMLS	Direct metal laser sintering
DSC	Differential scanning calorimetry
DTG	Derivative thermogravimetric
E	Elastic modulus
E'	Storage modulus
E''	Loss modulus
EBM	Electron beam melting
EPDM	Ethylene-Propylene Diene Monomer
EPR	Ethylene propylene rubber
FDM	Fused Deposition Modeling
FESEM	Field emission scanning electron microscopy
FFF	Fused Filament Fabrication
FTIR	Fourier-transform infrared spectroscopy
H_2SO_4	Sulfuric acid

HDPE	High density polyethylene
HDT	Heat distortion temperature
HPS	High pressure side
IR	Infrared spectroscopy
$j_{exp}(t)$	Permeation flux
LA	Lactic acid
LDPE	Low density polyethylene
LMD	Laser metal deposition
LNC	Lauryl functionalized nanocellulose
LOM	Laminated object manufacturing
LPS	Low pressure side
MAH	Maleic anhydride
MCC	Microcrystalline Cellulose
MFI	Melt flow index
MJM	Multi-jet modeling
MMM	Mixed matrix membranes
MVI	Melt volume index
N_2	Nitrogen
NC	Nanocellulose
NFC	Nanofibrillated cellulose
NMR	Nuclear magnetic resonance
PA	Polyamide
PBIH	Powder bed and inkjet head
PC	Polycarbonate
PEEK	Polyether ether ketone
PEI	Polyetherimide
PET	Polyethylene terephthalate
PHA	Polyhydroxyalkanoate
PHBH	poly(3-hydroxybutyrate-co-3-hydroxyhexanoate)
PLA	Poly(lactic acid)
PLAgMAH	Poly(lactic acid) grafted Maleic anhydride
PP	Polypropylene
PPS	Polyphenylene sulfide
PPSU	Polyphenylsulfone
PS	Polystyrene
PU	Polyurethane
PVA	Poly vinyl alcohol

RE	Reverse Engineerin
Rep-Rap	replicating rapid prototype
ROP	Ring-opening polymerization
RP	Rapid Prototyping
RPM	Round per Minute
SEM	Scanning electron microscope
SHS	Selective heat sintering
SLS	Selective laser sintering
STL	Stereolithography
tan δ	Loss tangent
Tc	Crystallization temperature
Tcc	Cold crystallization temperature
TEB	Tensile energy at break
Tg	Glass transition temperature
TGA	Thermogravimetric analysis
Tm	Melting temperature
UC	Ultrasonic consolidation
UTS	Ultimate tensile stress
Xc	Crystallinity fraction
δ_B	Stress at break
ε_B	Strain at break

List of tables

List of figures

Chapter I

1. Introduction

The prevention of climate changes and ecological catastrophes require actions to preserve our environment [4-6]. Also, raw materials and the manufacturing processes may play a role. The widespread of new technologies like additive manufacturing could contribute to reduce the human footprint [7]. In fact, the intrinsic nature of this process leads to material saving since no scraps are produced like in subtractive process. Additive manufacturing gives the possibility of producing an object in any place where it is really required, in our home, inside the International Space Station or on the ground of another planet [8-10]. This will also lead to a reduction in CO_2 emissions due to transportation. One of the most diffused additive manufacturing technologies is Fused Deposition Modeling (FDM). FDM is a technique used to build up objects where a filament of thermoplastic polymer is extruded through a nozzle at a specific temperature, usually higher than the glass transition temperature or melting temperature, and deposited layer by layer to form the final object. The ever-growing accomplishment of FDM is due to its benefits over traditional manufacturing such as free design, no need to use mold in manufacturing, ability to obtain complex parts. In principle, with FDM it is possible to manufacture light weight parts for the automotive and aerospace industry. Furthermore, waste material can be turned easily in final products with a low amount of energy and chemicals treatment [3]. The use of biopolymers is the natural step to improve the “green” benefits of 3D printing. According to the European Bioplastics Association, in 2017, the so-called bioplastics represented only 2.06 million tons of the 320 million tons of plastics produced annually [11]. The global production capacity is expected to increase up to 2.62 million tons in 2023. This growth is pushed forward by the demand of more sophisticated biopolymers, new applications and products. Bioplastics are used in an increasing number of applications from packaging, agriculture, consumer electronics, textile to automotive. In fact, biopolymers offer several additional advantages if compared to conventional plastics, such as a reduced carbon footprint and additional waste management options.

The use of natural or synthetic fibers is well contemplated to obtain specific characteristics and major improvements of the final properties of biopolymers [12]. Natural fibers offer several advantages over synthetic fibers due to their characteristics of renewability and biodegradability. This makes natural fibers a good candidate as fillers in composite made by biopolymers. Nanocellulose fibers have attracted significant interest in the scientific community over the past 20 years due to outstanding mechanical properties [13, 14], high specific surface area and interesting optical characteristics [15]. Cellulose was found to be one of the most interesting

reinforcing agents for producing green nanocomposites, due to their size and the ability to chemically modify the surface. So, they could be used in a wide variety of applications such as foams, adhesives and protective coatings [16-18].

The aim of this research is the investigation of the effects of the addition of different amounts of cellulose micro and nanocellulose on the physical and thermo-mechanical properties of different types of commercial biopolymer, already in use in 3D printing like poly(lactic acid) and polyvinyl alcohol but also some materials never applied in this kind of application such as polyhydroxyalkanoates. Two types of nanocellulose: crystalline nanocellulose (CNC) and nanofibrillated cellulose (NFC) were prepared starting from commercial crystalline micro cellulose and had been used as filler in biopolymer matrices. Different types of composite materials were considered:

- Micro and nano composite made by solution mixing of hydro soluble and biodegradable polyvinyl alcohol and microcrystalline cellulose and crystalline nanocellulose.
- Micro composite obtained with melt-mixing of poly(lactic acid), grafted and not grafted with maleic anhydride, and microcrystalline cellulose.
- Nanocomposite obtained through solution mixing of poly(lactic acid) and nano fibrillated cellulose.
- Nanocomposite obtained through solution mixing of poly(lactic acid) and lauryl functionalized nanocellulose.
- Nanocomposite obtained through solution mixing of poly(3-hydroxybutyrate-co-3-hydroxyhexanoate) and nanofibrillated cellulose.

These composites were used to produce filaments to feed a 3D printer operating according to the Fused Deposition Modeling technology. Scanning electron microscopy was employed to evaluate the fillers dispersion into the matrices and the structural morphology of printed samples. Thermogravimetric and calorimetric analyses were conducted to evaluate the effect of the various fillers on the thermal stability, the glass transition temperature, the crystallinity and the melting behavior of the polymeric matrices.

Mechanical properties were determined through quasi-static tensile tests, for the evaluation of the elastic modulus, while viscoelastic properties were studied through

dynamic mechanical analysis in tensile and creep conditions. The possible changes in the chemistry of polymers due to the presence of compatibilizer agents were investigated by UV-vis spectroscopy analysis and in some cases the structure of the material was studied with nuclear magnetic resonance. A detailed analysis on the barrier effect of composite films made with PLA and lauryl functionalized nanocellulose was conducted by determination of permeability and diffusivity of different gaseous species.

Chapter II

2. Background

2.1. *Additive Manufacturing*

Additive manufacturing (AM) is an increasingly popular manufacturing techniques that allows the production of solid objects in a new and disruptive way. It can be defined as one of the most important tools of a new industrial revolution because it changes completely the way objects are formed. It allows people to make customized products without using expensive tools or molds and so drastically decreasing costs and accessibility to manufacturing items [19]. This technology consists in the production of 3D objects starting from a digital model. It is gradually introduced in many fields, from the aerospace to the automotive and bioengineering with traditional materials such as polymers, metals and ceramics, but also food [20], tissue engineering [21] and nanocomposites [22-24]. It can e used to produce many objects, even with complex shape and in a relative short time, a direct consequence of this ability is that is useful for the construction of concept models and functional prototypes. The first 3D printer was developed by Chuck Hull in 1984 [25] (Figure 1a) when, working for the company 3D Systems Corp, he developed the stereolithography (STL) that is able to cure selective parts of a liquid photopolymer layer by using a laser. Together with the apparatus Hull was able also to develop the STL file format that is now the most used format for exchange of 3D models and can easily be processed by software for filling, slicing and cutting such as Slic3r. In the following years, many other AM devices were created and also the media interest increases in particular when the first open-source extrusion-based plastic printer was developed at the University of Bath (Figure 1b). The Rep-Rap (**rep**licating **rap**id prototyper) opens the door for a market of low-cost 3D printers that were the perfect tool for a widespread design [19].

(a)

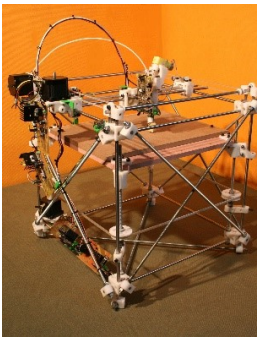

(b)

Figure 1. The first stereolithography machine invented by Hull in 1984 (a) and the first FDM machine of the project RepRap by Bowyer (b).

2.1.1. Benefits of Additive Manufacturing

Additive manufacturing has the potential to vastly accelerate innovation, compress supply chains, minimize materials and energy usage, and reduce waste [26]. Below, we list some benefits of AM technology [27]:

- *Lower energy consumption:* AM can contribute in saving energy by eliminating production steps, using substantially less material, enabling reuse of by-products, and producing lighter objects [25]. There is a large reduction in energy consumption from traditional process such as casting, that requires large-scale heating and cooling cycles. It has been calculated that AM has the potential to reduce the global energy supply from 9.3 to 2.4 MJ and CO_2 emissions from 525 to 130 Mt of industrial manufacturing by 2025 [28]
- *Less Waste:* due to its additive characteristic, AM can reduce material needs and costs by up to 90% compared to conventional subtracting techniques. AM can also reduce the costs and the disposal at the end of life of machine component through avoidance of the tools, dies, and materials scrap associated with classic manufacturing processes [26].

- *Reduced time to market:* items can be fabricated as soon as the 3-D digital model of the part has been created, eliminating the need for expensive and time-consuming part tooling and prototype fabrication.
- *Innovation:* AM enables designs with novel geometries that would be difficult or impossible to achieve using CM processes, which can improve a component's engineering performance. Novel geometries enabled by AM technologies can also lead to performance and environmental benefits in a component's product application.
- *Part Consolidation:* AM permits to design products with fewer, more complex parts so reducing the number of components. Fewer parts means less time and labor is required for assembling the product, again contributing to a reduction in overall manufacturing costs.
- *Lightweighting:* with the elimination of tooling and the ability to create complex shapes, AM enables the design of parts that can often be made to the same functional specifications as conventional parts, but with less material.
- *Agility to manufacturing operations:* additive manufacturing enables quick response to markets. Spare parts can be produced on demand, reducing or eliminating the need for stockpiles and complex supply chains [3, 26].

2.1.2. Additive Manufacturing steps

All the AM processes have some steps in common that are needed for each AD machine from the desktop one to the most expensive. A summary of these techniques is reported in Figure 2.

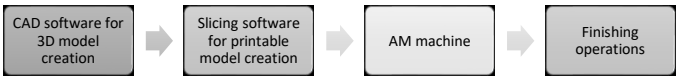

Figure 2. Fundamental steps required to produce an object with additive manufacturing.

The starting point of each type of AM technology is a 3D CAD model that is used to design the shape of the product. Many software are available for this aim that can be commercial software such as SolidWorks, Inventor, ProENGINEER and open software like OpenSCAD.

When the reconstruction of an existing object is needed, a previous step called Reverse Engineering (RE) is required which consists in obtaining a geometric model from the real part by acquiring the points belonging to the surface of the real part. This is possible by using 3D scans or Coordinate Measuring Machines (CMM). The output of a 3D CAD software is a .stl file that can be easily read and processed by a 3D printing processing software. The file format .stl derives from the STereoLithography (STL) and it was created by 3D systems [25]. It is widely used for rapid prototyping in computer-aided manufacturing preprocessing software such as: Slic3r, OctoPrint, CraftWare, KISSlicer. These softwares are able to generate a gcode file, that is a programming language to instruct the machine how to reproduce the 3D model, layer by layer. Using these tools, it is also possible to design the filling of the object by selecting pattern and filling density or to generate support material that is usually necessary for overhanging parts.

After that, the gcode is transferred to the AM machine that physically build the real object layer by layer with the previously set up settings according with the selected technology. Finally finishing operations can be needed in order to remove scrap, supporting material or to decrease the surface roughness [29]. Examples of post-processing methods are manual sanding, abrasive flow machining, sand blasting, manual dipping, acetone dipping and vapor smoothing [88].

2.1.3. Applications

The main application of AM in the industry was for Rapid Prototyping (RP). In fact, it is very important to perform a preliminary form and fit evaluation directly from the 3D model. Nevertheless, due to a decrease in manufacturing costs and to the development of new, fast and precise AM machines the process is gradullay introduced also final products.

The most important industrial success stories for final part production are [30]:

- *Automobile components:* right now, AM cannot compete with the traditional methods for mass production but is used more and more frequently for high-end, specialized automobiles components such as Formula 1 race cars.
- *Aircraft components:* the potentiality in the aircraft industry is mainly due to the low volume of production and to the possibility of printing complex

components that with traditional manufacturing have to be separated in smaller parts and then assembled.

- *Custom orthodontics, hearing aids, prosthesis and other biomedical parts*: using 3D scan data it is possible to create tailor-made biomedical objects that perfectly fit the patient. Using AM it is also possible to build shoes or insoles that perfectly fit the customer's foot and that can modify bad postural habits.

Nowadays, with the decreasing of the cost of desktop-scale 3D printers and with the increasing interest in the open-source technology.

2.1.4. Materials

Polymers due to their low costs and easier manufacturability in respect of most traditional building materials are represent the greatest market penetration and user accessibility [31]. In Figure 3 is shown the repartition of materials used in AM printing by tonnage used in 2013. Although plastic materials are not involved in the development of structural mechanical components like metals, they still represent the 99% of the market. Polymers in AM will represent a greater choice over metals in many fields from consumer products, sustainable applications, advanced manufacturing to biomedical devices [32]. Liquid monomers or polymers in form of solid material, such as filaments in FDM, represent the largest part of the market over powders due to difficulties in handling of the latter by most non-manufacturing consumers [33].

There are several polymeric materials available for additive manufacturing and selections are dependent on the method used and the mechanical properties to be achieved. Some of the most important polymers for AM are acrylonitrile-styrene-butadiene (ABS), polycarbonate (PC), polylactide (PLA), polystyrene (PS), polyamide (PA), and polyurethane (PU). These materials are mainly used for low performance components or for prototyping designs, but the demand for new higher performance polymer materials and composites is growing. High temperatures and chemically resistant polymers such as polyphenylene sulfide (PPS), polyetherimide (PEI), polyphenylsulfone (PPSU), and polyether ether ketone (PEEK) are studied in the last few years to be applied in AM due to their high performances [34, 35]. A lot of interest is emerging in the use of composite and nanocomposite materials in additive manufacturing to improve the mechanical properties or introduce new functions to commercially-available polymers like thermal and electrical conductivity [36].

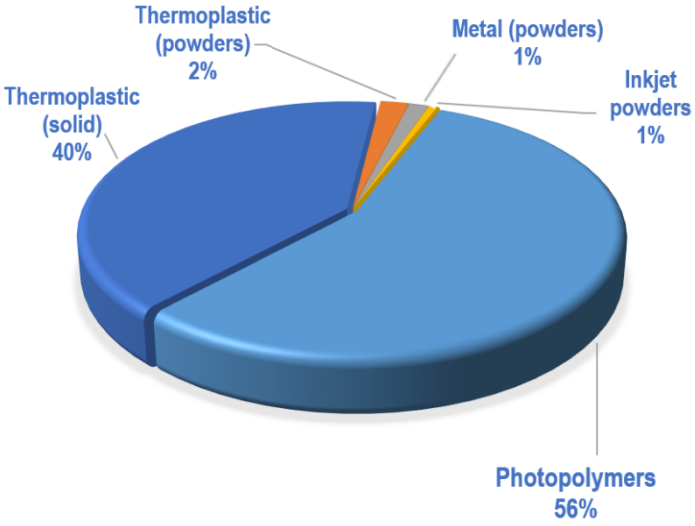

Figure 3. Materials used in AM as fraction of weight material consumed in 2014 [33].

2.1.5. Summary of most important AM techniques

AM techniques have many points in common, as an example each technique is based on adding one layer over the other, but there are also important differences among the methods of layer-by-layer manufacturing [37]. There are several possibilities for the classification of AM processes, the one proposed by the ASTM Committee classifies the AM processes into seven areas [38].

Table 1. Classification of the principal AM processes.

Process Type	Brief Description	Related Technologies
Powder Bed Fusion	Thermal energy selectively fuses regions of a powder bed	Electron beam melting (EBM), selective laser sintering (SLS), selective
Directed Energy Deposition	Focused thermal energy is used to fuse materials by melting as the material is being deposited	Laser metal deposition (LMD)
Material Extrusion	Material is selectively dispensed through a nozzle	Fused deposition modeling (FDM)
Vat Photopolymerization	Liquid photopolymer in a vat is selectively cured by light-activated polymerization	Stereolithography (SLA), digital light processing (DLP)
Binder Jetting	A liquid bonding agent is selectively deposited to join powder materials	Powder bed and inkjet head (PBIH), plaster-based 3D printing (PP)
Material Jetting	Droplets of build material are selectively deposited	Multi-jet modeling (MJM)
Sheet Lamination	Sheets of material are bonded to form an object	Laminated object manufacturing (LOM), ultrasonic consolidation (UC)

2.1.6. Fused Deposition Modeling

Fused deposition modeling (FDM) or fused filament fabrication (FFF) is one of the fastest spreading technology among additive manufacturing (AM) techniques due to the continuous decrease of the related costs. The FDM technology was first develop by Scott Crump and commercialized in 1990 (Figure 4) [39]. But it is only after 2008, with the expiration of the FDM patent by Stratasys, that it is possible to observe a rise in the production and so in the diffusion of cheap FDM machines. The development of new smart materials, nanocomposites and biomaterials could boost the growth of this additive manufacturing technology [40].

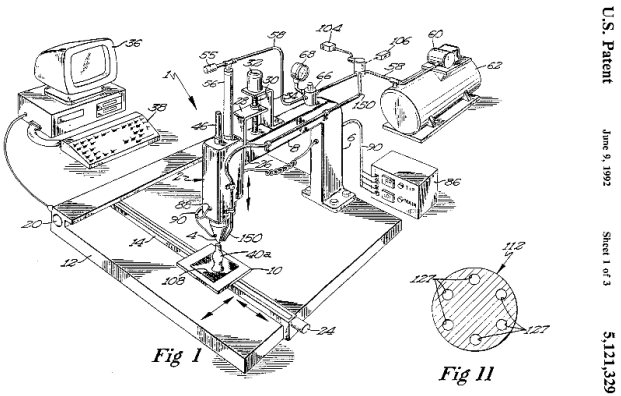

Figure 4. Artwork from US Patent 5,121,329: Apparatus and method for creating three-dimensional objects by S. Scott Crump, Stratasys Ltd, June 9, 1992.

In the FDM process, a nozzle is mounted on a support that can move horizontally in two dimensions, the material, usually in form of filament, is forced to pass through a nozzle that is heated to a temperature that is variable on the basis of the printing material. The pressure needed to force the filament through the nozzle is given by a mechanical system: two opposite rolls, with knurls for a proper filament grip, are connected to an electric motor and can rotate to generate the required pressure. The extruded filament is deposited in a thin layer on a build platform where it can solidify quickly upon contact with substrate or on the layers already deposited. Solid layers are generated by following a rasterizing motion where the material is deposited side by side within an enveloping domain boundary. Once a layer is deposited the build platform is lowered in the z direction and another layer is deposited over the previous one. This process continues until the fabrication of the object is completed. Although as a printing technology FDM is very flexible and capable of dealing with small overhangs by the support from lower layers, FDM generally has some restrictions on the slope of the overhang and cannot produce unsupported stalactites. The adhesion between different layers is possible because the material is in a range of temperature where molecular movement are allowed leading to a thermal healing of the adjacent layers inside the printed object. For successful bonding an accurate control of the thermal environment is necessary for high temperature processable materials. Therefore, the deposition process is generally performed inside a chamber, maintained at a temperature just below the melting point of the material being deposited.

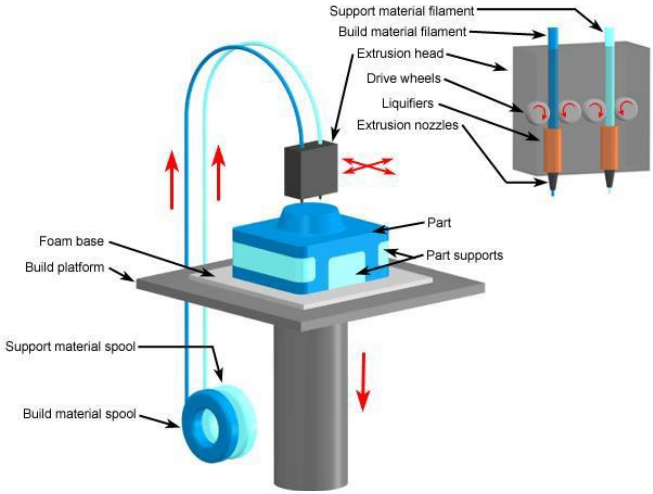

Figure 5. Fused Deposition Modeling machine layout.

2.2. Biopolymers

Giving a clear definition of the term biopolymer is not an easy task. According to the standard ASTM 6866-16 [41], a bio-based material is defined as a material that contains carbon of renewable origin, or it is biodegradable, or features both properties.

The normative also describe the method for evaluate the "bio-based content", which uses a radiocarbon analysis to count the number of carbon atoms that comes from the short CO_2 cycle, by evaluating the level of carbon-14 isotopes. In fact, the presence of C^{14} is indicative that a material derives from natural sources, C^{14} is formed in the upper atmosphere due to the interaction of cosmic radiations and atmospheric nitrogen; once formed, C^{14} combines with oxygen to form carbon dioxide, which is then assimilated and metabolized by living being. Biopolymers can be derived from biological system like plants, wood, microorganisms, parts of animals, or can be synthetized from biological starting materials like sugar, starch, etc. The feedstocks for biopolymers production are essentially of two types: the so-called first-generation feedstocks, which include edible biomass such as sugar, starch, plant oils, and non-edible sources such as natural rubber and the second-generation feedstocks, which include food waste products and lignocellulose [42].

Also, the term biodegradable can lead to misunderstanding. According to the definition given by the standard ASTM D6400 [43], a biodegradable material, in order to be considered as such, has to fulfil three key points [44]:

- the material must be related to a specific disposal pathway, such as composting, sewage treatment, denitrification, etc.;
- the degradation must develop at an appreciable rate, consistent to the disposal method;
- the final products of degradation should be CO_2, water, inorganic compounds and biomass, without the presence of any toxic compounds.

So, biopolymers can be characterized according to the source of the raw materials or according to their ability to biodegrade. In this way, they are distinguished in three main categories:

- biopolymers coming from renewable resources and *biodegradable*. Examples of polymers belonging to this category are PLA and PHA.

- biopolymers coming from renewable resources and *not biodegradable*. Polyamide 11 from castor oil or natural occurring biopolymers such as natural rubber.
- biopolymers coming from not renewable resources but *biodegradable*. They are produced from fossil fuel and are certified biodegradable, for example PCL or PVA.

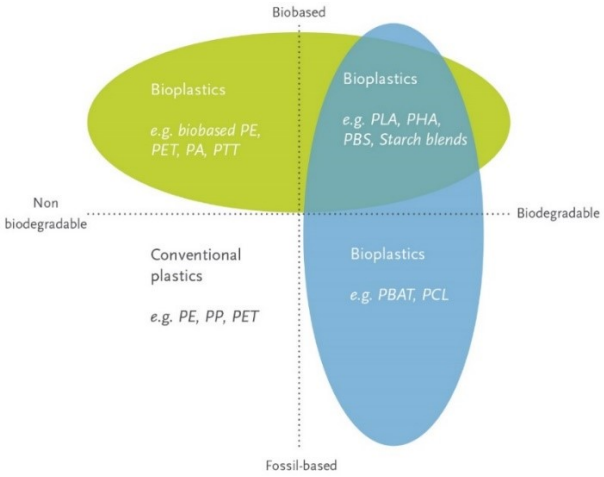

Figure 6. Bioplastics vs conventional plastics.

European bioplastics [45] identified the main applications with the respective market share and the main bioplastic produced. In 2017 the biopolymers production amounted at around 2.05 millions of tons, which corresponds to less than 1% of the total amount of polymers produced annually (estimated around 320 millions of tons) [45]. The market is dominated by bio-based polyethylene terephthalate (bio-PET), bio-based PE, bio-based polyamides (PA), polylactic acid (PLA), polyhydroxyalkanoates (PHAs) and plasticized starch blends. This great number of biopolymers with different chemical composition allows one to target a wide number of applications. However, this does not mean that biopolymers can easily replace conventional plastics. In fact, their application should involve benefits for the environment like an efficient use of resources and the elimination of waste. Industry and institutions start just nowadays to select stringent quality rules to guarantee, biodegradability in different environments, a low environmental impact for the whole product life cycle and

continuous improvements programs in order to improve the two previous aspects. For these reasons, biopolymers do not represent yet a complete alternative to the common polymers and therefore their application is limited to specific sectors.

2.2.1. Polyvinyl alcohol

Polyvinyl alcohol (PVA) is a hydrophilic, water soluble synthetic polymer, prepared by hydrolysis or alcoholysis of polyvinyl acetate, widely used in adhesive, paper-coating, textile industries and biodegradable polymer products [46]. PVA is also a water-soluble polymer, its water solubility derives from the presence of the hydroxyl groups that are able to establish hydrogen bonds with water molecules [47]. In fact, the balance between functional groups and the overall hydrocarbon content, combined with their arrangement in homopolymers or copolymers, is the key aspect for the water solubility [48]. PVA is non-toxic with a high barrier to oxygen and resistance to oil, grease and organic solvents and, thanks to its highly polar nature, it has also antifouling properties (prevents the attachment on its surface of sea life, like clams) [49].

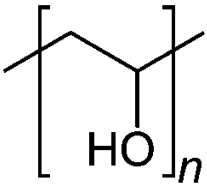

Figure 7. Chemical representation of Polyvinyl Alcohol.

Synthesis

The main problem related to PVA production is that the vinyl alcohol monomer is highly unstable. A possible path is to perform the hydrolysis of polyvinyl acetate through a two-step process such as that schematized in the following figure.

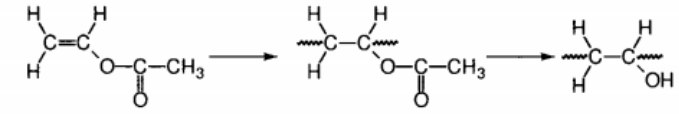

Figure 8. Chemical representation of the polymerization of PVA.

The first step is the polymerization of vinyl acetate monomer that takes place through free-radical polymerization. This process, consisting in initiation, propagation and termination, is started by an initiator, which can be an hydroperoxide, a persulfate or a redox system. The next step involves the substitution of the acetate groups [OCOCH3] with the hydroxyl ones [OH] through hydrolysis. The hydrolysis reaction takes place in a methanol solution, which not only acts as a chain transfer agent, but also, through the evaporation, removes the heat generated by the reaction. A small amount of a catalyst (either acid or basic) is then added in order to have an ester exchange reaction between the polyvinyl acetate and the methanol with the conversion of the acetate groups into hydroxyl ones [50, 51]

During the hydrolysis process some residual acetyl groups are generally not substituted by the hydroxyl ones. The molar percentage of those residual groups it's known as the "degree of hydrolysis" and this value strictly depends on the concentration of the catalyst used during the reaction. The concentration of acetyl groups can be quantitatively evaluated with spectroscopy, melting point or iodin color reaction. Therefore, it is possible to have three commercial grades of PVOH:

- Fully hydrolyzed, with a degree of hydrolysis between 98-99% and a molar concentration of residual acetyl groups between 0.6-1.5%;
- Intermediate, with a degree of hydrolysis between 93-97% and 2.7-6.9% of residual groups;
- Partially hydrolyzed, 85-90% of degree of hydrolysis and 10-15% of acetyl groups.

Properties

Thermal and water solubility properties of PVA are affected by the degree of hydrolysis of the polymer [52]. Increasing the degree of hydrolysis leads to an increase of the water and solvent resistance, the crystallinity, the tensile and adhesive strength. The glass transition temperature is located between 70 °C and 90 °C, depending on both the thermal history of the polymer and on the water content. The partial hydrolysis leaves some acetate residues which allows the polymer to be dissolved even in cold

water (but it has a decreased biodegradability); fully hydrolyzed PVOH are, vice versa, only soluble in hot water but possess a higher biodegradability level [50]. Even the crystallinity affects the solubility in water of PVA, increasing the crystallinity (through a heat treatment or a cyclic treatment) increases the dissolution temperature [53].

Mechanical properties are strongly affected by the relative humidity, as shown in *Figure 9*. An increase of relative humidity makes the polymer to become less rigid, with a consequent decrease of tensile strength and elastic modulus and an increase of the elongation at break [50]. For commercial PVA grades, these properties are usually found between 37-45 MPa for the elastic modulus, 44-64 MPa for the tensile strength and an elongation at break between 150-400% [47].

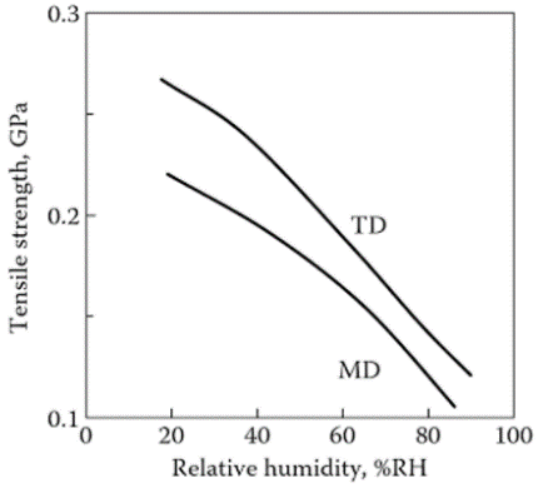

Figure 9. Tensile strength vs relative humidity of PVA [51].

The most important drawback regarding the processability of PVA is the thermal degradation starting at around 150°C, i.e. below the melting temperature (of about 230°C). From 150°C to 400°C dehydration reactions and formation of volatile products take place and they are the main causes of mass loss. At temperatures higher than 400°C the decomposition of carbonaceous species occurs [54]. Due to this problem, PVA is processed with difficulty through traditional processes like

extrusion with the addition of some plasticizers which decrease the melting temperature to 180°-190°C and allows only a slight decomposition during extrusion or other forming processes. The possibility of improving the thermal stability of PVA by adding proper nanofillers has been demonstrated in many literature articles. The role of nanofillers to thermal resistance has commonly been described as a barrier model, which proposes that the thermal resistance is enhanced due to the formation of a strong char on the surface of the polymer [55]. This char forms a barrier against the transfer of mass and heat limiting the passage of degradation products from the matrixes. This effect was well documented both for inorganic fillers [56-58] both for natural nanofiller such as nanocellulose [59, 60].

Degradation

Despite PVA is a biodegradable polymer, its biodegradation is quiet difficult in natural environment and this polymer should be removed from the wastewater before its discharge [48, 61]. The reason lies on the fact that PVA's degrading microorganisms are not spread throughout the environment, they are very limited in respect the species able to degrade other polymers and they need a period of acclimatization of days or weeks [62]. In any case, the degradation takes place by the oxidation of the polymer by specific enzymatic systems with the evolution of hydrogen peroxide and a consumption of oxygen, with the result of producing carbonyl groups [CO] along the polymer chain [63].

Applications

Thanks to its water solubility and biodegradability, PVA has a great potential in many fields, from the biomedical to the agricultural and water treatment [64]. It is usually used in papermaking to improve the quality of printed matter as surface sizing agent, under-sizing agent, dispersant for fluorescent dyes and filler binder for inkjet recording materials [50]. PVA is used in packaging application as a water-soluble film or in food packaging application. The first use derives from the fact that it can slowly dissolve in contact with water and release a series of products during time; the second one involves its great oxygen barrier properties useful to protect food. The excellent adhesion properties of PVA make it suitable to create adhesives which are able to absorb water or work as a barrier against this solvent [49]. Hydrophilicity and hydro solubility of PVA generated also increasing interest in the biomedical field especially in tissue engineering[65] and drug delivery [66-68]. PVA finds also application in FDM

technology as vanishing support material for overhanging parts because it can be easily removed from the object just by water immersion without any machining process (Figure 10).

Figure 10. Printing a complex structure with overhanging parts with PVA supports that are then dissolved in water.

2.2.2. Poly lactic acid

Polymers from lactic acid (PLA) are a quite large category of polymers from renewable resources. They are not only compostable and biocompatible, but also processable with most standard processing equipment [69, 70]. PLA is a compostable polymer derived from renewable sources; it has been viewed as a potential material to reduce the societal solid waste disposal problem. Its low toxicity, along with its environmentally benign characteristics, has made PLA an ideal material for food packaging and for other consumer products. PLA is the front runner in the emerging bioplastics market with the best availability and the most attractive cost structure. The production of the aliphatic polyester from lactic acid, a naturally occurring acid and bulk-produced food additive, is relatively straightforward. PLA is a most promising biopolymer, since it offers unique features of biodegradability as well as thermoplastic processability. It is a thermoplastic material with stiffness and light transmissibility similar to polystyrene or poly(ethylene terephthalate). PLA is used for many different applications, from packaging to agricultural products and disposable materials, as well as in medicine, surgery and pharmaceutical fields [69-71].

Synthesis

Starting point for the production of PLA is lactic acid (LA). Lactic acid is the most widely occurring hydroxycarboxylic optical active acid. It was first discovered in 1780 by the Swedish chemist Scheele. LA is a naturally occurring organic acid that can be produced by fermentation or chemical synthesis [72]. LA consists of two enantiomers, one is known as L-lactic acid and the other, its mirror image, is D-lactic acid (Figure 11). A mixture of the two in equal amounts is called DL-lactic acid.

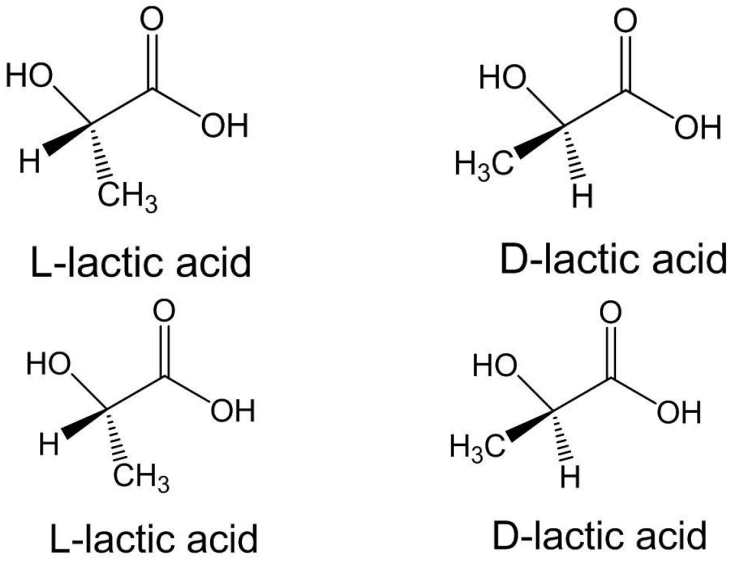

Figure 11 - Structure of L- and D- acids

PLA can be obtained using different routes as shown in Figure 12. In general, there are three methods which can be used to produce high molecular mass PLA of about 100 000 Daltons: direct condensation polymerization; azeotropic dehydrative condensation and polymerization through lactide formation, the ring-opening polymerization (ROP). Currently, direct condensation and ring-opening polymerization are the most used production techniques.

- Polycondensation of lactic acid is a relatively simple process to produce PLA. Lactic acid monomers with the presence of hydroxyl and carboxyl groups can undergo self-esterification, which leads to reversible step-growth polymerization and production of water as by-product. High temperatures and vacuum are used to remove produced water from bulk solution to reduce reversibility of reaction, but usually it still results in low molecular weight polymers mainly because of the presence of water and impurities. Other disadvantages of this route are the requirement of relatively large reactors and huge energy consumptions to reach high temperature and vacuum leading to expensive final product [73].

- Azeotropic dehydrative condensation for synthesis of PLA was first reported by Kimura and coworkers [74]. During the melt polycondesation, aqueous L-Lactic Acid (LLA) solution is dehydrated and oligomerized to obtain LLA oligomers, which then are melt polycondensed to produce a PLA prepolymer. This prepolymer is then crystallized during the solid-state polycondesation process and finally polycondensed at solid state below melting temperature to achieve high molecular weight PLA [70]. The azeotropic dehydrative polycondensation brought a breakthrough in increasing the molecular weight of the polycondensation of LA. This method can afford PLA with a high molecular weight after a relatively long reaction.
- While direct polycondensation of LA should be the cheapest route to PLA, the ring-opening polymerization of lactide is the method used commercially. The resulting polymer is formed from an intermediate of lactic acid polycondesation, the lactide. Lactide is a cyclic dimer of lactic acid, which is formed by removal of water from the reaction mixture during oligomerization of lactic acid. Formed lactide is the starting monomer for ROP usually using metal alkoxides as catalysts resulting in high molecular weight polyester. Most commonly used catalyst is Stannous Octanoate due to its efficiency and low toxicity, making it one of the best choices to use for production of biodegradable and environment-friendly polymers [73].

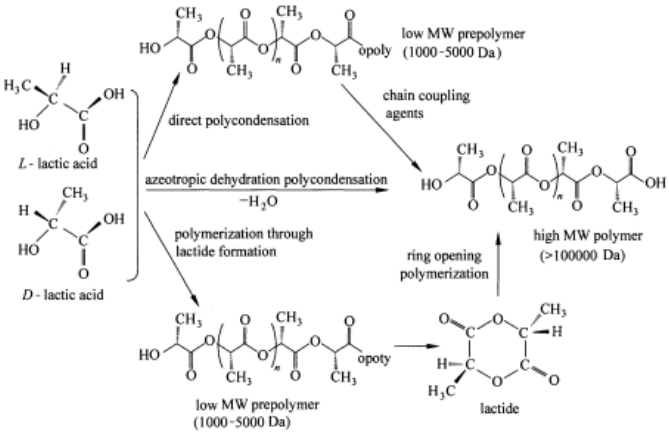

Figure 12. Synthesis of PLA from L and D latic acids [75].

Properties

The thermal, mechanical and biodegradation properties of PLA are largely dependent on the initial mixture of lactic acid enantiomers. Usage of racemic mixture will lead to meso-lactide thus resulting in the poly-DL-lactide and then to an amorphous polymer. Many important properties as the degree of crystallinity can be controlled by the ratio of D and L enantiomers used in the initial mixture. Polymers with high L-isomer concentration produce crystalline products, while higher D-isomer levels, more than 15%, result in an amorphous final product. However, the degree of crystallinity depends on many factors, such as molecular weight, thermal and processing history, and the temperature and time of annealing treatments. Thus, commercial PLA products are semi crystalline polymers with a high melting point ca. 180 °C and a glass transition temperature in the range 55–60 °C.

Physical properties are very important as they reflect the highly ordered structure of the polymer and influence mechanical properties and degradation kinetics. In general, for a particular use, the mechanical, physical and biodegradability properties of PLLA must be considered. Some significant properties of PLA are given in Table 2.

Table 2. Physical properties of PLA produced by DURECT Corporation, Cupertino CA (USA).

	PLLA	PDLA
Glass transition temperature	60 – 65 °C	50 – 60 °C
Melting point	184 °C	Amorphous
Specific gravity	1.24	1.25
Tensile strength (MPa)	55 – 82	27 – 41
Elongation at break (%)	5 – 10	3 – 10
Tensile modulus (MPa)	2758 – 4137	1379 – 2758

Polylactic acid can be processed into fiber (for example, using conventional melt spinning processes) and film. PLA has interesting mechanical properties compared with common thermoplastics such as PS and PET, but the crystallization rate is extremely slow which results in a low heat-distortion temperature (HDT) and limits the application in high temperatures. Several technologies such as annealing, addition of nucleating agents, formation of composites with fibers or nano-particles, chain extension and introduction of crosslinking bridges have been used to enhance the mechanical properties of PLA. One of the most efficient methods to improve the crystallization behavior of PLLA is the addition of the nucleating agents, that provide more nucleation sites thus shortening the induction time for crystallization and increasing the heat distortion temperature and tensile strength [70]. Mechanical orientation is another method for improving the mechanical properties of PLA due to its morphological change upon drawing. This process converts the otherwise fragile polymer into a versatile and useful material for packaging and biomedical applications [70, 71].

Biodegradation

The main challenge to widespread diffusion of bio-based polymers is to achieve properties similar to conventional synthetic polymers while retaining biodegradability. In nature, polymer degradation is induced by thermal activation, hydrolysis, biological activity, oxidation, photolysis, or radiation mediated lysis. PLA degradation has been

found to be dependent on a range of factors, such as molecular weight, crystallinity, purity, temperature, pH, presence of terminal carboxyl or hydroxyl groups, water permeability, and additives acting catalytically that may include enzymes, bacteria or inorganic fillers. PLA is efficiently degraded in soil, compost or in human body. It finds great interest for short time applications. Degradation of PLA in soil is relatively slow due to the slow rate of hydrolysis at low temperatures and water contents [76]. In this first stage, with the presence of water, PLA undergoes to hydrolytic degradation through the random cleavage of the ester bond, which is controlled by: the rate constant, the amount of absorbed water, the diffusion coefficient of chain fragments within the polymer and the solubility of degradation products [77]. PLA can be hydrolyzed into oligomers after 45 – 60 days at around 50 °C in a composting environment. These smaller molecules are then degraded into CO_2 and H_2O by microorganisms in compost [78]. PLA can degrade into lactic acid, a normal human metabolic by-product, which is broken down into water and carbon dioxide [79].

Applications

Being able to degrade into innocuous lactic acid, PLA is used as medical implants in the form of anchors, screws, plates, pins and rods. Depending on the exact type used, it breaks down inside the body in a controlled time that can goes from months to years. This gradual degradation is desirable for a support structure, because it gradually transfers the load to the body as that area heals [79]. Thanks to its bio-compatibility and biodegradability, PLA has also found ample interest as a polymeric scaffold for drug delivery purposes [80]. PLA can also be used as a decomposable packaging material, either cast, injection-molded, or spun. Cups and bags have been made from this material. In the form of a film, it shrinks upon heating, allowing it to be used in shrink tunnels. It is useful for producing loose-fill packaging, compost bags, food packaging and disposable tableware [81]. PLA is used as a feedstock material in desktop fused filament fabrication 3D printers due to its good processability and relatively low melting temperature. PLA printed solids can be encased in plaster-like molding materials, then burned out in a furnace, so that the resulting void can be filled with molten metal. This is known as "lost PLA casting", a type of investment casting.

2.2.3. Polyhydroxyalkanoates (PHAs)

Polyhydroxyalkanoates are a large family of thermoplastic polymers belonging to the polyesters category and they are synthetized by several types of bacteria, through the fermentation of organic substances. The general structure of PHAs is reported in Figure 13, where *m* can be equal or greater than zero and *R* can be a hydrogen atom or an alkyl substituent, depending on the type of PHAs.

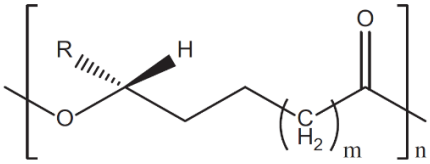

Figure 13. Chemical structure of polyhydroxyalkanoates.

Synthesis

Microorganisms, in normal conditions, usually assimilate carbon which is then converted and stored as nutrients in various forms, like glycogen, polyamino acids, polyphosphates and lipids. In particular conditions, however, some kinds of microorganisms can accumulate it as PHAs: the carbon sources are chemically converted in hydroxyalkanoate units that are polymerized through different biosynthetic pathways and stored inside the cell cytoplasm.

The first to identify the synthesis of PHAs from bacteria was Maurice Lemoigne, a French microbiologist, in the 1920s. He used a culture of Bacillus megaterium and he was able to isolate poly(3-hydroxybutyrate) [82]. Nowadays the most common bacteria species able to produce PHAs belong to the genera Alcaligenes, Azotobacter, Bacillus, Cupriavidus, Chromobacterium, Delftia, Pseudomonas, Ralstonia and Staphylococcus. This great variety of species allows the possibility to extract many different types of PHAs depending on the microorganism used [83].

It is believed that the conditions for the PHAs biosynthesis occurs when microorganisms are subjected to an environmental stress, i.e. to a lack of essential nutrients such as sulfur, nitrogen, ammonium, phosphate, potassium, iron, magnesium or oxygen [44]. Therefore, the production of PHAs involves, first, a cell growth phase, where bacteria are fed with the essential nutrients. Then the nutrients

are depleted to stimulate the polymer biosynthesis. PHA is accumulated in the form of granules in the bacterial cell cytoplasm. The average size of the PHA granules is approximately 0.2– 0.5 μm [84]. In Figure 14 a transmission electron micrograph of *Pseudomonas putida* cells containing PHA granules is reported.

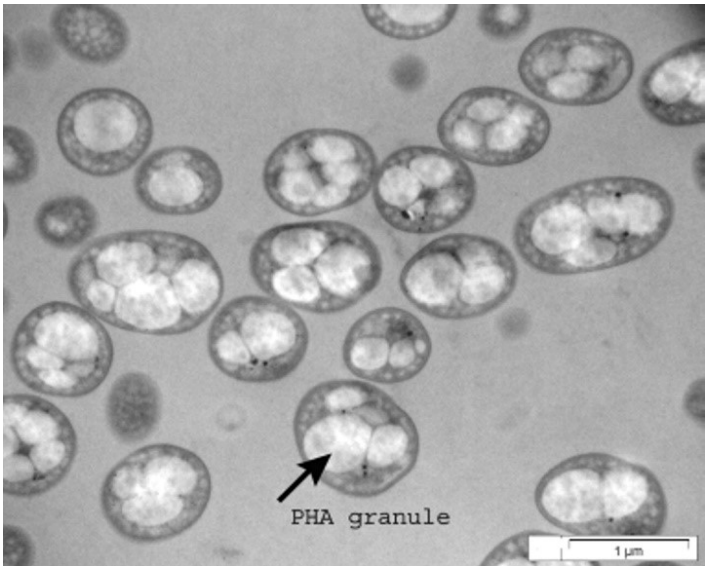

Figure 14: Pseudomonas putida cell containing PHA granules.

Carbon sources for the PHAs production, i.e. substrates for bacteria fermentation, derive from renewable resources of animal or vegetable origin, which imply the indirect utilization of atmospheric CO_2. Substrates could be monosaccharides such as sucrose, lactose, starch and ligneocellulose [85-88]. Triacylglycerols, that are the main components of animal fats and plant oils and are metabolized only by some bacterial species, generally belonging to the *Pseudomonas* genera [89, 90]. The use of hydrocarbons as substrates, instead, is not relevant from an economic point of view because only few species of bacteria are capable to synthetize PHAs from this sources and the process tends to be slow [91]. Not only the right choice of the bacteria species but also the correct carbons sources has to be applied to produce the wanted type of PHAs. Therefore, a correct combination of bacteria and substrate, allows the control of the composition of the accumulated polymer.

After the biosynthesis, PHAs have to be extracted from the cell through a recovery process. This is a fundamental step because the system used can affect the extraction yield and the quality of the final product. Moreover, extraction may imply high energetic costs and the use of dangerous solvents, thus reducing the environmental benefits of PHAs and their economic applicability. The recovery methods depend on several factors such as the microbial strain, the type of PHA, the intercellular load of PHA, the required purity of the final product and the availability of chemicals. The approaches for polymer recovery can be distinguished in 5 main categories [92]:

- Dissolution and precipitation of PHA by solvent: this direct method for the extraction of the polymer from biomass is the most used for commercial PHA production. The extraction is performed using halogenated solvents like chloroform and dichloromethane that are able to dissolve the lipid part of the non-PHA cell mass. The harmful character of chloroform, that is used in an amount of 20 times the mass of the extracted polymer, represents the major drawback of this method and reduce the aspect of green technology related to the PHA biosynthesis [93]. In order to increase the sustainability of the process alternatives have been found: the use of non-halogenated solvents or industrial waste streams or the use of supercritical CO2 as solvent thanks to the high solubility for various compounds [94].
- Digestion of the cell membrane by enzymes: this method consists in removing the non-PHA cell mass through the conversion of the same in water-soluble substances and then after filtration, floatation or centrifugation recover the PHA granulates. [95]
- Digestion of the cell membrane with chemicals: same procedure adopted in the previous method but carried out in different ways. Disintegration of the biomass using sodium hypochlorite at high pH values so most cell components become water soluble due to oxidation and can be removed.
- Mechanical disruption of the cell: the microbial cell are disintegrated by high-pressure homogenization or ultrasonication.
- Disruption of osmophilic microbial cells: the rupture of the cell is caused by the high internal pressure in hypotonic media like desalted water due to osmotic absorption, that causes the release of the intracellular content.

Properties

Nowadays, more than 150 different type of hydroxyalkanoic acids monomers have been found [96]. This multitude of different monomers leads to a great number of PHAs types, which can cover a wide range of physical properties. From a commercial point of view, the most important PHAs are the homopolymer poly(3-hydroxybutyrate) (P(3HB) or simply PHB) and copolymer of 3HB with a second monomer unit including poly-(3-hydroxybutyrate-co-3-hydroxyvalerate) (PHBV), poly(3-hydroxybutyrate-co-4-hydroxybutyrate) (P3HB4HB), and poly(3-hydroxybutyrate-co-3-hydroxyhexanoate) (PHBH) [42].

This great variety allows having a wide range of properties, so there is, the possibility to have some grades with the same physical characteristics of polypropylene and others with elastomeric features or to produce block copolymers with different monomers units to engineering the final properties of the material. Physical properties are greatly influenced by the monomer composition, i.e. the length of the backbone chain and the nature of the pendant groups. Generally, PHAs are characterized by [97]:

- Low thermal properties with a glass transition temperature between -50 °C and 0 °C and a melting temperature generally lower than 200 °C
- Relatively good resistance to hydrolytic degradation and UV radiation;
- Solubility in chlorinated hydrocarbon.

Biodegradation

One of the main features that make PHAs interesting in many fields of application is their ability to biodegrade both in aerobic and anaerobic environments, without forming toxic compounds. As in the case of other biodegradable polymers, PHAs undergo first to a depolymerization induced by enzymes (PHA depolymerizes) secreted by microorganisms such as bacteria or fungi, which hydrolyze the solid polymer in water-soluble monomers and oligomers. Then, this low molecular weight molecules are transported into the cell, where are metabolized as carbon sources and energy sources [44].

Depolimerization of PHA can be executed by many species of bacteria, allowing the biodegradation in many terrestrial and aquatic ecosystems (Figure 15) [98, 99]. The rate of biodegradation depends on the microbiological activity, the moisture content of the environment, the temperature, the pH, the shape of the exposed material, the

chemical composition of the PHA. The crystallinity content is also important because the degradation in the amorphous regions is much faster compared to the crystalline regions. Moreover, it is also affected by the crystal size and lamellar thickness [100]. In any case, PHA based material can lose their weight completely in a few months. A study, for example, demonstrated that PHA strips completely degrade in only 10 weeks if they are exposed to favorable conditions [101].

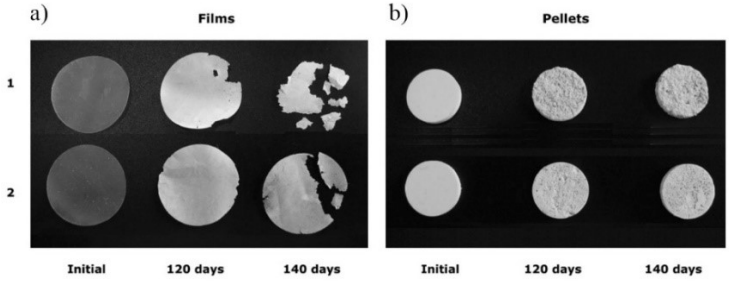

Figure 15: biodegradation effects on a) films and b) pellets made by PHA and exposed to tropical coastal waters [98]

Applications

The similarity in mechanical and thermal properties of some PHAs with polypropylene and other commodity polymers along with their bio-based nature and biodegradability, lead to a great interest for possible applications in various fields.

PHAs are used in biomedical field since the mid-1960s, thanks to versatile physical and chemical properties. In fact, monomers of PHAs are not toxic and not carcinogenic and for an extended period up to one year after intramuscolar implantation, they did not cause any acute vascular reaction or any adverse events, such as suppurative inflammation, necrosis, calcification of the fibrous capsule or malignant tumor formation [102]. Moreover, PHAs have proven to have good biocompatibility, i.e. the abilities to support cell adhesion and growth [103]. This features, make them suitable for the production of absorbable surgical sutures and drug carriers [104, 105] (Figure 16).

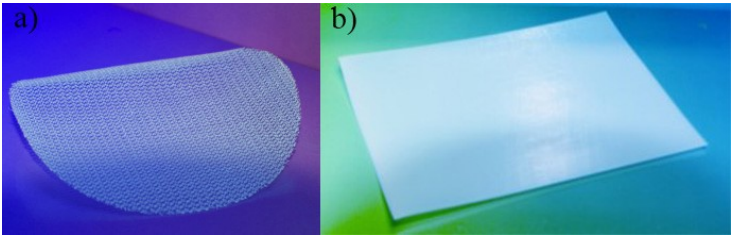

Figure 16. Example of surgical mesh (a) and surgical film (b) made by polyhydroxyalkanoate produced by Tepha [106].

Regarding industrial applications, PHAs could be a potential replacement of conventional polymers as packaging materials and household items. However, their high costs make them noncompetitive in the current market compared to the fossil fuel-based polymers. The thermal properties of PHAs, such as glass transition temperature below 0 °C and melting temperature higher than 60 °C, are suitable for packaging In addition, the oxygen and water barrier properties are comparable or even better than polyethylene and polystyrene and they can be further improved by developing nanocomposites with the addition, for example, of nanoclays. In a similar strategy, PHAs can be used as additives for conventional polymer to improve their barrier properties [107]. P(3HB) was studied and tested as a substitute for polypropylene in injection molded packaging products and showed promising results, proving to be suitable for food packaging, although it is characterized by more fragility and less flexibility respect to PP [108]. To improve flexibility, P(3HB) can be synthetized with various co-polymers such as poly(3-hydroxyvalerate), that leads to a decrease in glass transition temperature and melting temperature. As biodegradable material, PHA finds application as herbicide carriers thanks to the ability of biodegrade in soil, releasing gradually the herbicide [109].

Figure 17. Example of products made by polyhydroxyalkanoates with the trade name Mirel™ [110].

The main factor that limits the commercialization and industrialization of PHAs is their price. In fact, PHAs are more expensive than traditional commodity polymers. While polyolefins like polyethylene and polypropylene nowadays have prices lower than 1 €/Kg [111], PHAs can range from 4 €/Kg to 16 €/Kg depending on the purity grade [112]. Their higher prices depend mainly on the high cost of carbon sources, substrates and on the low extraction yield at industrial scale. For this reason, the key point for decreasing the PHAs costs is the increase in the use of high carbon waste streams from the agro-industry, i.e. cane and beet molasses, cheese whey, plant oils and hydrolysates of starch, cellulose and hemicellulose, etc. [113, 114].

2.3. Cellulose

Cellulose is the most abundant natural polymer, whose repeat unit is derived from glucose. It is such a crucial component of the cell wall of different plants. Along with plants, cellulose is also present in a large variety of living species, like algae, fungi, bacteria, and even in sea animal such as tunicates. Although widely found in nature, at industrial scale cellulose is derived almost entirely from cotton and wood.

Cellulose was discovered in 1838 by the French chemist Anselme Payen, who isolated it from plant matter after a treatment with acids and ammonia, and a subsequent extraction with water, alcohol, and ether. He was able to determine also its chemical formula, but the polymer structure of cellulose was only described in 1920 by Hermann Staudinger. Cellulose was used to produce the first successful thermoplastic polymer by Hyatt Manufacturing Company in 1870. [115]. However, in its almost pure form, such as cotton and flax fibers, cellulose had also been used since a long time ago, as clothing and writing material going back to the time of Egyptian pharaohs [116].

2.3.1. Hierarchical structure of cellulose

Cellulose is a long chain linear semicrystalline homopolymer consisting of glucose repeating units (Figure 18). The degree of polymerization of cellulose varies depending on its source. Since a molecule of water is lost when an alcohol and a hemiacetal react to form an acetal linkage, each glucose molecule in cellulose is referred to as anhydroglucose (AGU) unit. Each repeating unit contains two anhydroglucose units. In each AGU unit there is one primary hydroxyl (OH) group at the carbon 6^{th} position, and two secondaries OH groups at the 2^{nd} and 3^{rd} positions. Owing to these OH groups, cellulose has a highly hydrophilic behavior, although the strong inter- and intramolecular hydrogen bonds restrict the solubility of cellulose in water.

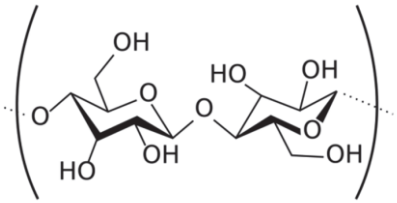

Figure 18. Chemical structure of cellulose.

Parallel stacks of cellulose chains form the smallest fibril constituents of cellulose fibres, known as cellulose nanofibrils. An individual cellulose nanofibril consists of both amorphous and crystal structural domains. In the amorphous region the cellulose chains have a disordered arrangement, whereas in the crystalline regions cellulose chains are tightly arranged in ordinated structures to form strong, stiff crystal domains. Different polymorphs or allomorphs of the cellulose crystalline structure can be identified depending on the hydrogen bonding and molecular orientation that changes from the source of the cellulose.

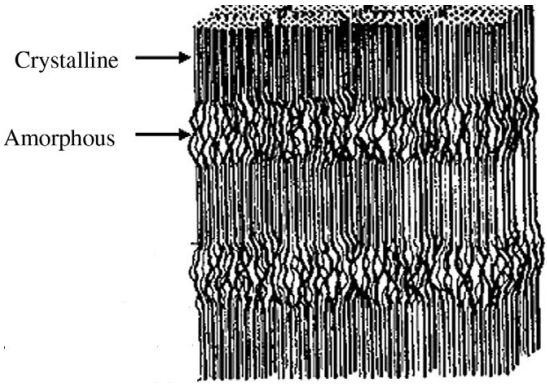

Figure 19. Cellulose organization [117]

Wood cellulose nanofibrils have a typical width of 3-5 nm and length of several micrometres and wrap around each other with strong hydrogen bonds, forming aggregates of larger microfibrils. Microfibrils have a typical width of 5-50 nm, which in turn aggregate to larger cellulose fibrils. The microfibrils reinforce the wood structure with an intra-chain and inter-chain hydrogen bond network [118]. The plant fibers can be considered as naturally occurring composites due to their unique structure, in which the semi crystalline cellulose microfibrils act as reinforcing elements in an amorphous matrix mostly made up of lignin and hemicellulose. While the matrix performs as a natural barrier to microbial degradation and serves as mechanical protection, the cellulose microfibrils have the function to provide rigidity and structural stability to the cell wall of the fibers [119].

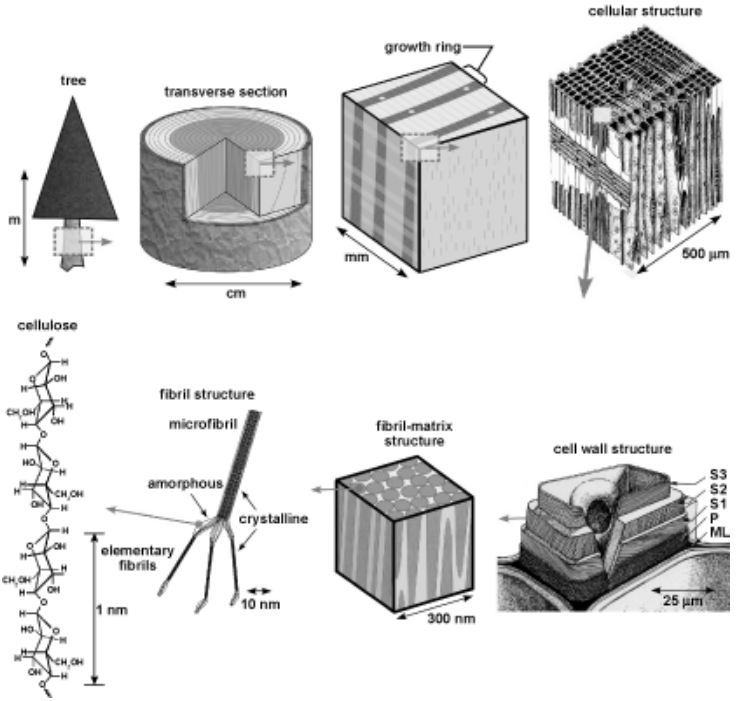

Figure 20. Hierarchical structure of wood from tree to cellulose molecules.

Cellulose fibers are the main load-bearing component in trees and plants due to the high modulus of its crystalline part, which can reach 140 GPa [120]. The most important variables that determine the overall properties of the wood material are the structure, microfibrillar angle, cell dimensions, defects, and the chemical composition of fibers [121]. In combination with its low density, cellulose has a potential reinforcing capability comparable to that of inorganic and synthetic fibers such as aramid and glass. The mechanical properties of natural fibers differ mostly depending on the processing method used to break down the lignocellulosic material to the fiber level. However, isolation of cellulose in the nano-size range, is required in order to take full advantage of its inherent properties. When the crystalline regions of cellulose nanofibrils are isolated though an acid treatment, a nanocellulosic material referred to as cellulose nanocrystals (CNCs) is produced while the one obtained mainly by mechanical disintegration is called cellulose nanofibrils (CNF). The two types of cellulose nanofibers that can be liberated from cellulose fibers are described in the two next sections.

2.3.2. Nanofibrillated cellulose (NFC)

Nanocellulose fibrils were firstly exctracted by Turbak and its group in 1983, who produced cellulose with lateral dimensions in the nanometer range by subjecting a wood pulp slurry to high shear forces several times through a high-pressure homogenizer [122]. Some of the first nanocomposites containing NFC were prepared in 1983 by Boldizar et al. [123]. After several passes through the homogenizer or inside an ultra-fine friction grinder, cellulose fibers can be disintegrated by high shearing forces to flexible NFC having both crystalline and amorphous domains with diameters starting from *around* 5 nm to tens of nanometers, which correspond to single microfibrils and length of few micrometers. NFC possess high aspect ratio and form gels in water with shear-thinning and thixotropic behavior [124].

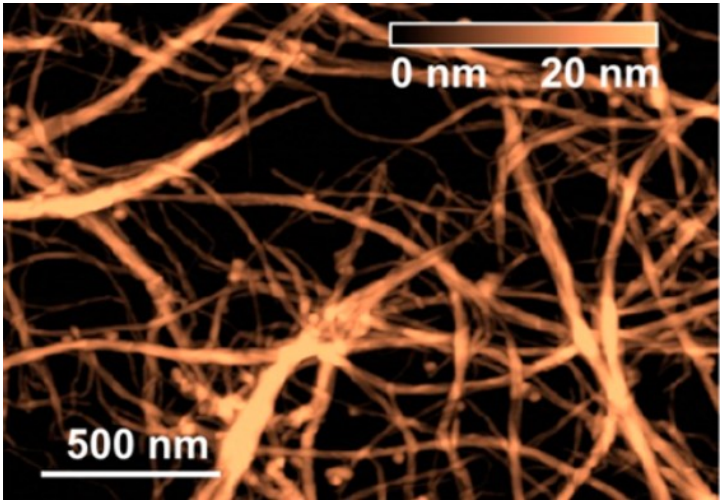

Figure 21. AFM image of cellulose nanofibrils obtained through mechanical disintegration [124].

2.3.3. Cellulose nanocrystals (CNC)

Rånby was the first to describe the preparation of a stable colloid suspension of cellulose nanocrystals *via* sulfuric acid hydrolysis in the early 1950's [125]. In this method, concentrated sulfuric acid is commonly used, which degrades amorphous regions of cellulose while the crystalline regions remain more or less intact. The hydrolysis conditions such as time, temperature and acid concentration strongly affect the yield, size, morphology and crystallinity of cellulose nanocrystals [126]. Commonly, nanocrystals with diameters ranging from 2 nm to 20 nm and length ranging from 100 nm to 2.1 μm are produced [127]. By such treatment, rod-like rigid CNC with negatively-charged sulfate groups at their surface are produced. These groups help the dispersion and colloidal stability of the CNC suspension *via* electrostatic repulsion, but the thermostability of CNC is reduced [128]. Wood and cotton are the principal sources for the extraction of CNC due to their natural abundance and high cellulose content, respectively. The CNC from these sources are 3-70 nm wide and 100-300 nm long [129].

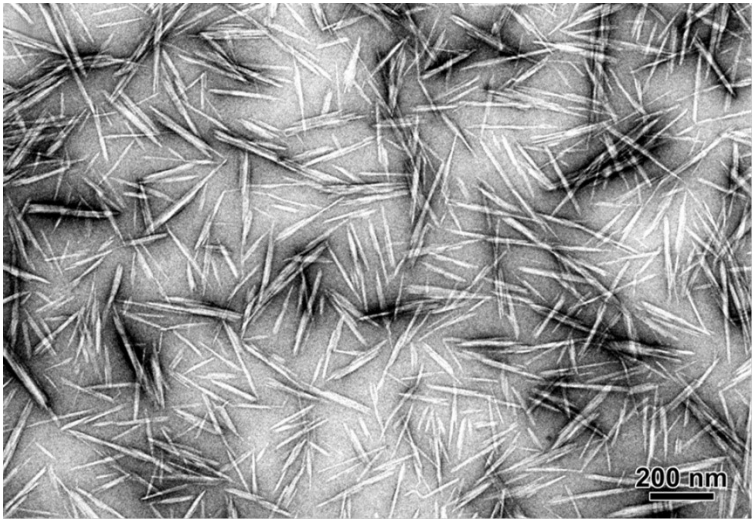

Figure 22. Transmission electron micrographs from a dilute suspension of ramie nanocrystals [130].

Chapter III

3. Experimental

3.1. Materials

3.1.1. Polyvinyl alcohol

Polyvinyl alcohol (PVA) with the trade name of Mowiflex, TC 232 was provided by Kuraray Specialties Europe GmbH (Frankfurt, Germany). It is provided in form of pellets soluble in hot water with a density of 1.27 g/cm3 and a melt flow index (MFI) at 2.16 kg and 190°C of 3.9 g/10 min.

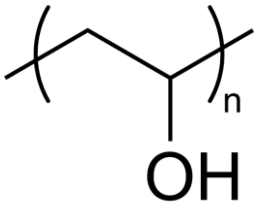

Figure 23. Chemical formula of PVA.

3.1.2. Polylactic acid

Poly(lactic acid) (PLA) code 4032D was provided by Nature Works LLC (Minnesota, USA). According to the datasheet, this polymer has excellent optics, good machinability and excellent twist and dead fold. 4032D is an ideal product for laminations and other packaging applications. It was characterized with a density of 1.24 g/cm3 and a melting point of 155-170°C. According to literature the content of enantiomer D is in the range 1.4-2.0% [131]

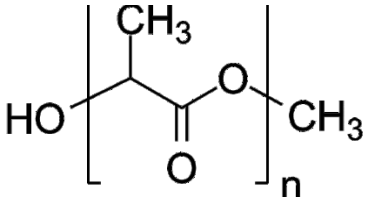

Figure 24. Chemical formula of PLA.

3.1.3. Poly(3-hydroxybutyrate-co-3-hydroxyhexanoate)

Poly(3-hydroxybutyrate-co-3-hydroxyhexanoate) (PHBH) is a natural copolymer belonging to the family of the polyhydroxyalkanoates. It is formed by 3 hydroxybutyrate (3HB) and 3 hydroxyhexanoate (3HH) units. The presence of 3HH units causes a decrease in the melting temperature and in crystallinity but an increase in ductility with respect to PHB due to the increased steric effect given by the side alkyl chain. In Figure 25 the chemical formula of PHBH is reported.

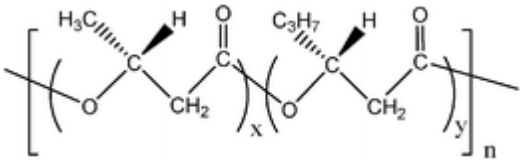

Figure 25. Structural formula of PHBH.

In this study, two different types of PHBH provided by Kaneka Corporation (Osaka, Japan) were used with the trade name of X131A and X151A. They differed for the content of 3HB in the copolymer that changed the thermal and mechanical properties according to datasheet provided by Kaneka (Table 3).

Table 3. Datasheet for PHBH X131A and X151A.

	X131A	X151A
Density (g/cm^3)	1.20	1.19
Tm (°C)	145	126
Tg (°C)	2	0
MFI (g/10min @ 165°C, 5kg)	3	3
Tensile modulus (MPa)	1820	950
Tensile strength (MPa)	36	26
Tensile elongation (%)	4	320

3.1.4. Microcrystalline cellulose

Microcrystalline cellulose, MCC, (specific gravity=1.56 g·cm-3, mean molecular weight= 90000 g/mol) prepared through the reaction of cellulose with a water solution of strong mineral acid at boiling temperature, supplied by Sigma Aldrich (USA), were selected as microscale reinforcing filler. MCC particles consist of elongated flakes with an average length of about 24 μm and a diameter of about 10 μm (average L/D ratio of 2.4).

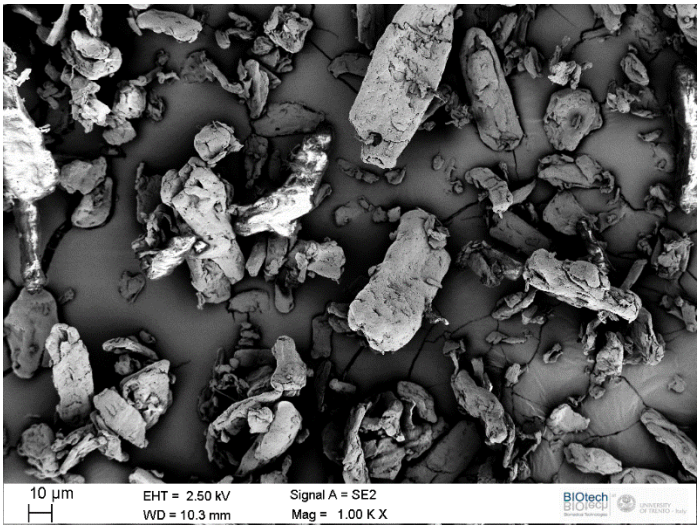

Figure 26. SEM picture of MCC.

3.2. Nanocellulose preparation

Two different approach were followed to isolate nanocellulose from micro-cellulose in this study. The first method was based on a chemical route to dissolve the amorphous regions in between the crystalline ones to obtain highly crystalline nanocellulose (CNC). The other method was based on high intensity ultrasonication to disaggregate the micrometric structure of cellulose in nanofibrillated cellulose (NFC).

3.2.1. Crystalline nanocellulose (CNC)

Microcellulose was the starting point to prepare a water solution of cellulose nanocrystals. The method to dissolve the amorphous regions in between the tiny crystals of nanocellulose through an acid hydrolysis is well described in literature [118, 126, 132]. A solution of microcellulose and sulfuric acid at 64% was prepared with an MCC/H_2SO_4 concentration of 0.10 g/ml. The solution was strong stirred for 120 min in a mechanical mixer at a temperature of 45°C. At the end, the reaction was stopped adding distilled water in a volume excess ratio of 10. The acid was removed by several centrifuge cycles at 6000 rpm for 15 min each. The pH of suspension was neutralized through dialysis using cellulose membranes with a cut-off limit of 3.5 kDa. The suspension was then sonicated for 5 min in a Hielscher 400S sonicator equipped with a sonotrode with a diameter of 3 mm. The obtained aqueous suspension of crystalline nanocellulose was kept at 4°C until further use. As evidenced by observations with atomic force microscopy (AFM) and field emission scanning electron microscopy (FESEM), rod-like particles with a length from 200 nm to 500 nm and a diameter of around 5-10 nm were produced.

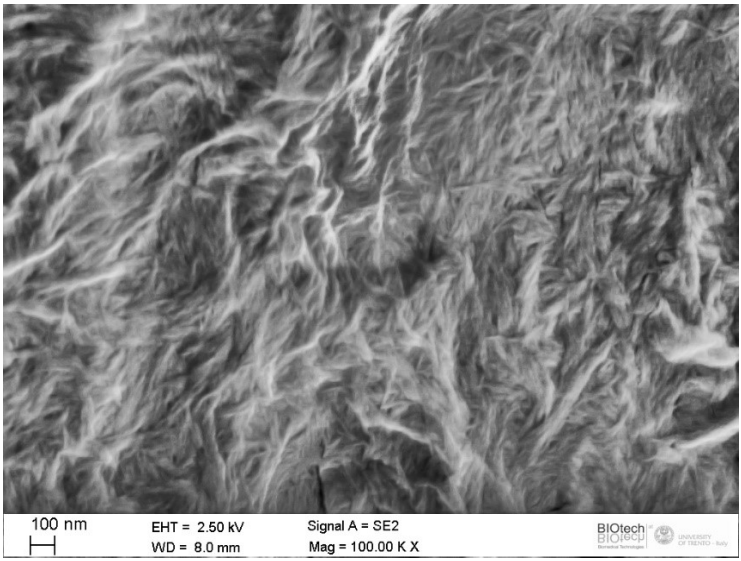

Figure 27. SEM picture of CNC.

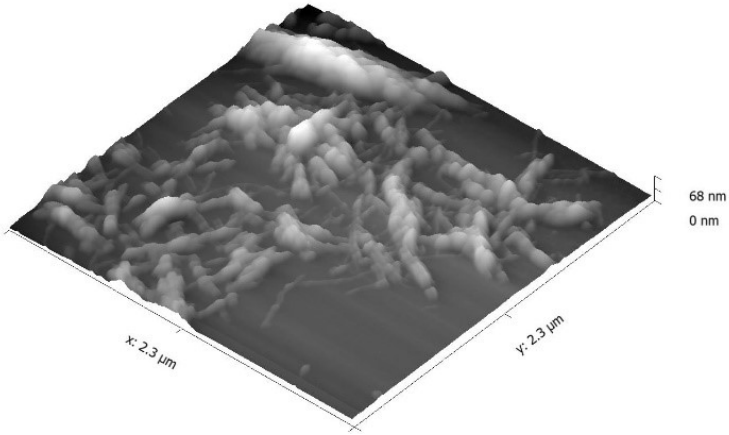

Figure 28. AFM picture of CNC.

3.2.2. Nanofibrillated cellulose (NFC)

Another approach, that was followed in this research to obtain nanosized cellulose from microcellulose, was the defibrillation of the nanofibrils with high energy ultrasonication as reported in literature [60, 133-137]. The starting point was a well dispersed solution of microcrystalline cellulose in double distilled water at 10wt%. This solution was ultrasonicated for 20 minutes in an ice bath with a Hielscher UP400S device (Teltow, Germany), equipped with a cylindrical sonotrode of 3 mm in diameter operating. As reported by Frone et al. [133], the main parameter in this process is the ultrasonication energy, the maximum energy of 400W was used to reach o good yield of nanofibrillated cellulose. The solution was kept at 4 °C for 7 days in order to let the micrometric particles to sediment and the supernatant liquid was collected and frozen at -30 °C. Frozen supernatant was freeze-dried with a LIO-5PDGT device for at least one week to remove completely the water. At the end of the process, nanocellulose was obtained and stored at 4 °C.

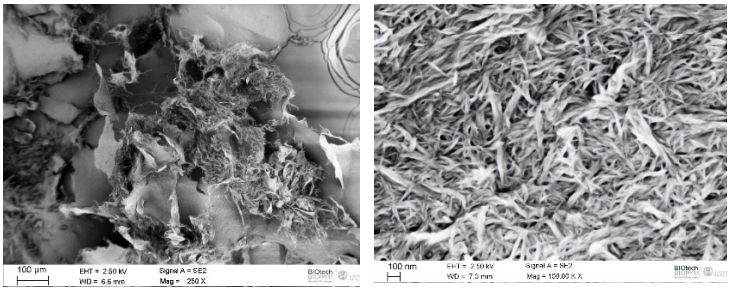

(a) (b)

Figure 29. SEM pictures of freeze-dried NFC.

3.2.3. On the use of CNC and NFC

While carrying out this study, CNC was easily and efficiently applied for the reinforcement of PVA due to the good chemical compatibility and the possibility of mixing together PVA and CNC directly in water without a previous separation of CNC from the aqueous solution. The incorporation of filler in a hydrophobic polymer, such as PLA or PHBH, required to work with non-polar solvents or at high temperature and so the cellulose needed to be separated from the liquid solvent. In the open scientific literature, a wide number of protocols can be found [129, 138], such as solvent exchange or freeze drying. However, these methods highlighted that the main drawback for CNC was its poor thermal stability (Figure 30) which can be attributed due to the presence of sulfate groups grafted onto the cellulose during the hydrolysis process [139].

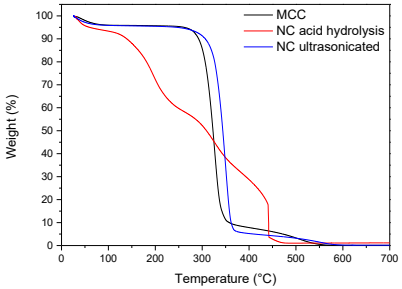

Figure 30. TGA curves for MCC, CNC and NFC.

Experimental evidences of this phenomenon were observed during the melt compounding of freeze-dried CNC and PLA. Nanocellulose degraded immediately inside the heated chamber of the melt-compounder as evidenced in Figure 31. To overcome this problem, a different approach based on ultrasonication was adopted when hydrophobic polymers were chosen as matrices.

Figure 31. Freeze dried CNC degraded during melt compounding at 165°C.

3.3. Filament preparation

The filaments were extruded with a single screw extruder provided by Friul Filiere (Buia, Italy). This extruder was characterized by a screw diameter (D) of 14 mm, a screw length of 25D and a die diameter of 3 mm.

Prior to the extrusion the material was finely grinded to properly feed the extruder screw. The temperature in the feeding zone was set at 100°C for all the materials to avoid the aggregation of the powder and the clog of the feeder. The temperature profile inside the extruder increased from 100°C in the feeding zone to the final temperature in the die zone that was accurately selected for each composition. The speed of the screw was set at 30 rpm to have a good flow of the melted material and it was collected by a rolling belt with a speed of 20 mm/s. Under these selected processing conditions, continuous filaments were obtained with a diameter of 1.7 mm suitable to be used in a commercial 3D printer machine based on FDM technology.

An in-depth description about the preparation of the filaments and the specific temperature profile of the extruder will be given for each material in the relative chapter.

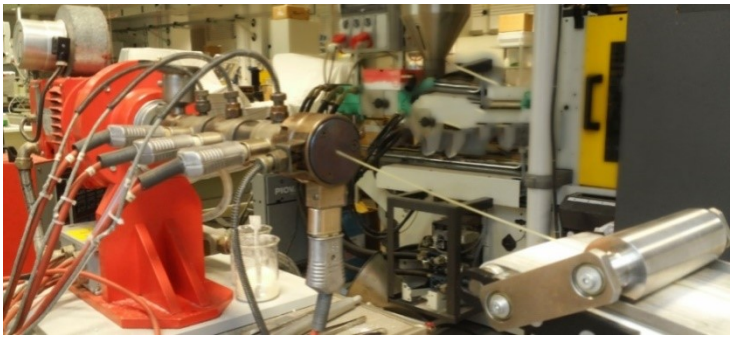

Figure 32. FriulFiliere single screw extruder and rolling belt.

3.4. 3D printing

For the realization of 3D printed samples, a Sharebot Next Generation desktop 3D printer, provided by Sharebot Italy, was used. It was characterized by a printing volume of 200 mm x 200 mm x 200 mm, a nozzle with a diameter of 0.35 mm that can reach 260°C. Dumbbell specimens (ISO 527 1BA) were drawn using SolidWorks software. The 3D model was exported in a rapid prototyping format (.stl) and uploaded to Slic3r software, where the model was treated by a slicing algorithm to generate G-code. Linear infill with an angle of ± 45° between layers and a fill percentage of 100% were chosen to obtain the best mechanical properties without the introduction of stress amplifiers inside the parts due to the infill path. These 2D sliced layers were then built layer by layer by the printer with deposited layers of 0.2mm in height till the final object was physically formed. Other parameters such as nozzle temperature, bed temperature and deposition rate were carefully selected for each material.

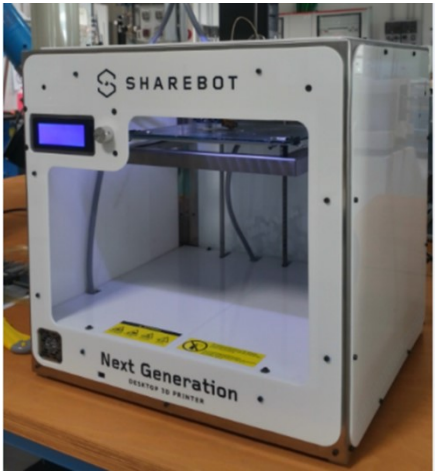

Figure 33. Sharebot NG 3D printer.

3.4.1. Specimen orientation during 3D printing

Due to the high anisotropy of the objects built with a FDM process, the production of specimens made by different polymers and/or different compositions, it was a crucial point in order to allow a comparable characterization. In this study, specimens were printed in the horizontal plane and coded as XYZ where XYZ indicated the three mutually orthogonal directions 123 of the specimen inside the 3D printer according to international standard (see Figure 34).

This particular configuration led to an easy fabrication of dumbbell specimens without the introduction of supports for overhanging parts, no thermal distortions were observed and a good reproducibility of the mechanical properties of the same sample was obtained.

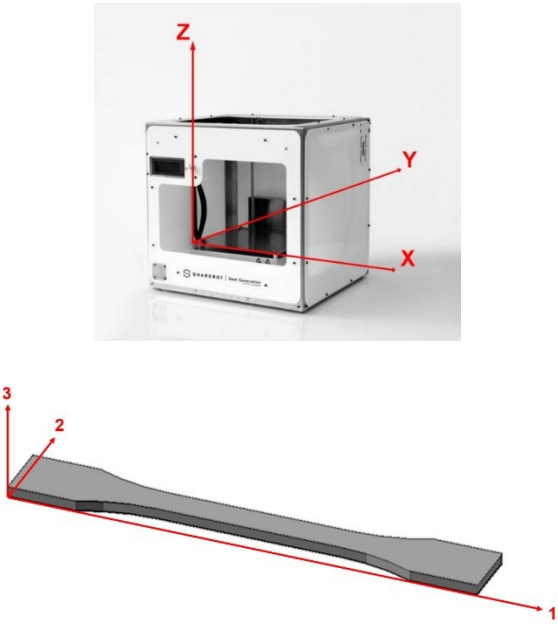

Figure 34. Axes orientation of the 3D printing machine according to ASTM F2971 and axes orientation of a dumbbell specimen 1BA.

3.4.2. Infill orientation and defects

Particular attention was given in the design of 3D printed specimen to obtain a fracture in the middle of the dog bone specimen.

3D printed objects, with a precise geometrical disposition in a 2D space that resembled the structure of fibers in composite, were made by FDM. The geometrical disposition of the material inside 3D printed specimen is generally named as “infill pattern” and it can be changed in angle and in shape layer after layer.

The simplest infill pattern available in the adopted 3D printing software was a rectilinear one that was similar to the orientation of the fibers in a unidirectional continuous fiber reinforced composites and from them it take the nomenclature to indicate the way the filaments were arranged layer by layer. Preliminary studies highlighted that one of the main parameters that affected the fracture behavior was the infill pattern.

In particular, geometrical defects, that acted as stress concentrators, were introduced in the specimens when they were printed with infill pattern 0°/0° or 0°/90°. As it was possible to observe in Figure 35, these defects led to a fracture inside the grip tabs for infill pattern 0°/0° (Figure 35a) and the detachment of the outer part of the specimen for 0°/90°. A good fracture behavior was found with infill orientation ±45°, breakage happened in the gauge length and was quite reproducible through samples with different formulations of all the polymer matrices.

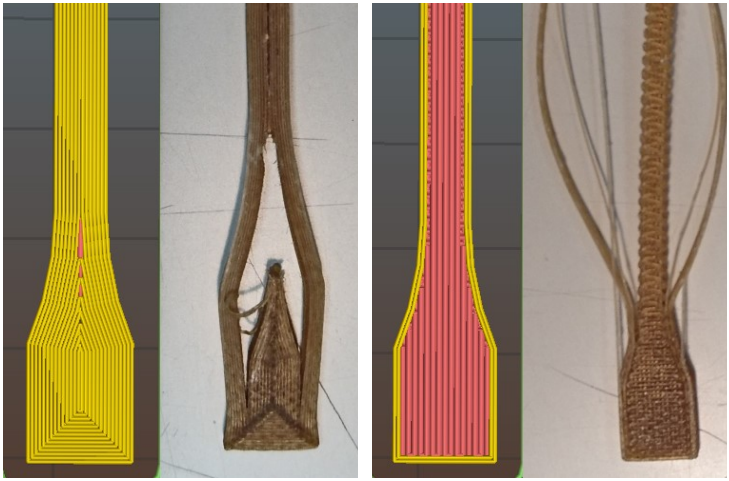

(a) (b)

Figure 35. Pictures of geometrical defects in 3D printed specimen with an infill pattern of 0° (a) and 0°/90° (b). Sample: PVA_10CNC.

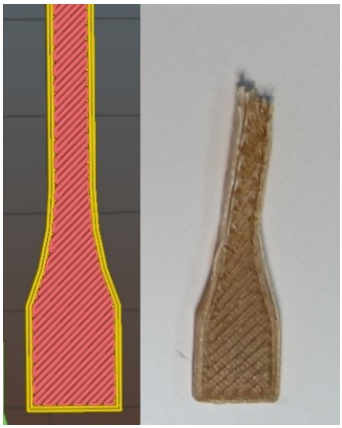

Figure 36. Infill ±45° provided a fracture in the gauge length of the specimen. Sample PVA_10CNC.

3.4.3. Role of the density in the mechanical properties of 3D printed specimens

The apparent density of 3D printed specimens was correlated to the mechanical properties. This approach was adopted to take consider the effects of the voids presence on the mechanical properties of 3D printed sample and to highlight the effects of the fillers introduction.

The apparent density, as shown in Equation III-1, is the ratio between the weight of the specimen and its volume.

$$Apparent\ density = \frac{weight}{volume} \qquad \text{(Eq 1)}$$

The volume was easily evaluated using the Equation III-2, where w is the width of the specimen, b is the width at center (5 mm) of the specimen model with an area A equals to 520 mm^2 and t is the thickness.

$$Volume = \left(\frac{w}{b}\right)^2 A\ t \qquad \text{(Eq 2)}$$

The ratio between apparent density and the real or theoretical density, called R (Eq 3), it was used to link the mechanical properties to the material excluding the presence of voids and porosity, so it was possible to compare different samples with different porosity. Real or theoretical density was calculated experimentally with the aid of a pycnometer.

$$R = \frac{apparent\ density}{theoretical\ density} \qquad \text{(Eq 3)}$$

R-factor was useful to estimate the quality of 3D printed specimen before tensile test. R in the range of 0.8 - 0.9 indicated a good quality without the presence of defects inside the object, instead values lowers than 0.7 were indicators of poor quality and low mechanical properties.

3.5. Materials characterization

3.5.1. Atomic force microscopy

The morphology of nanocellulose obtained via acid hydrolysis was analyzed by Atomic Force Microscope (AFM) technique. AFM measurements were performed with a NT-MDT, Solver Pro instrument in semi-contact mode. A droplet of aqueous CNC suspension was allowed to dry on a silicon surface and a tip of 22nm of curvature and 10 N/m was used to scan the specimen.

3.5.2. Optical transparency

In some cases, the developed material could find some technical application in packaging where an important role is played by the light transmission. The optical transmittance was measured by a Jasco 570 UV-VIS-NIR spectrophotometer determining the energy absorbed in a spectral wavelength range from 250 to 800 nm.

3.5.3. Field Emission Scanning Electron Microscope

Microstructural observations were performed by a Zeiss Supra 40 high resolution Field Emission Scanning Electron Microscope (FESEM) with an accelerating voltage of 2.5 kV, after a platinum palladium conductive coating of the samples. To investigate the dispersion of the filler and its adhesion with the matrix the samples were immersed in liquid nitrogen to perform a brittle fracture that evidenced microstructural architecture of the material.

3.5.4. Rheological experiments

The apparent viscosity was measured as a function of shear rate using an Anton Paar MCR 301 rheometer. Before experiments, the samples were dried at 40 °C for 24 h. The rheometer was operated in the rotational mode with parallel plate geometry at 190°C, over a shear rate range of 10 to 1000 s^{-1}.

3.5.5. Thermo Gravimetric Analysis

Thermal degradation is a very important parameter to understand the maximum processability temperature of the composite material. It was investigated by thermogravimetric analysis (TGA). The analysis was performed by a TGAQ500 (TA Instruments, USA), at a constant heating rate of 10°C/min in the range between 40°C

and 700°C. All the tests were conducted in an inert atmosphere of N2 at a constant flux of 10 ml/min. Specimens of about 10mg were tested.

3.5.6. Differential Scanning Calorimetry

Together with TGA, Differential scanning calorimetry (DSC) is able to highlight the processability window of the composite material giving information about phase transitions. DSC was performed by a Mettler DSC 30 calorimeter. Tests were performed from -10°C to 250°C at a heating and cooling rate of 10°C/min under a nitrogen flow of 150 ml/min on specimens of about 10 mg. Glass transition temperature T_g, melting temperature Tm were evaluated. The degree of crystallinity (X_C) was evaluated with:

$$X_C = \frac{\Delta H_m - \Delta H_C}{\Delta H_0 (1 - x_f)} \qquad \text{Eq 4}$$

where ΔH_m was the enthalpy of fusion per gram of the polymer's matrix, ΔH_0 was the heat of fusion for the 100 % crystalline and x_f is the weight fraction of filler.

Table 4. Values of the heat of fusion for the polymer matrix used in this research.

Polymer's matrix	ΔH_0 (J g^{-1})
Mowiflex TC 232 (PVA)	161 [140]
Natureworks 4032D (PLA)	93.6 [141]
Poly(3-hydroxybutyrate-co-3-hydroxyhexanoate) (PHBH)	146 [142]

3.5.7. Infrared Spectroscopy

Fourier-transform infrared spectroscopy (FTIR) analysis can clarify if the chemical structure of the material is modified by the presence of the fillers or by the processing stages. It was carried out by a Spectrum One from Perkin-Elmer. Spectra were obtained in a wavenumber range from 4000 to 640 cm^{-1} by averaging 4 scans.

3.5.8. Humidity sorption test

Some of the materials used in this research presented a strong capacity to absorb humidity and therefore a dependence of the mechanical properties from their humidity containt. The humidity sorption of the material was evaluated by controlling the

change of weight of at least 5 samples for each composition during time. The specimens with dimensions of 20x5x1 mm^3 were kept under vacuum at 50°C for 2 days to reach their complete drying and then stored into a container at 23°C with 55% of relative humidity. The value of the water sorption was measured, according to ASTM D570 standard, by the change of weight of the samples.

3.5.9. Melt Flow Index

Viscosity of composite materials was investigated by melt flow index (MFI) tests according to ASTM 1238-04 standard. MFI tests were performed using a Kayeness 4003DE capillary rheometer at a temperature of 210°C for PVA and 190°C for PLA with a load of 2.16 kg. Before testing, the samples were kept under vacuum at room temperature for 24 hours to remove completely the humidity.

3.5.10. Dynamic Mechanical Analysis

Visco-elastic properties are very significant in the characterization of polymer composite materials. Visco-elastic behavior was investigated through Dynamic mechanical analysis (DMA), carried out in tensile configuration using a TA Instrument DMA Q800 device, in a proper range of temperature for each material, with a heating rate of 3°C/min, a strain amplitude of 0.05% and a frequency of 1Hz. Specimens with dimension of 20x5x1 mm^3 were tested. In case of filaments lenght of 20mm and diameter of 1.75mm were selected. Through this analysis it was possible to evaluate the storage modulus (E'), the loss modulus (E") and the loss tangent (tan δ) as a function of the temperature.

3.5.11. Quasi Static Tensile Test

Quasi-static tensile test allows to collect information on both the elastic behavior and the failure properties of the specimen type 1BA produced by 3D printing FDM. It was performed using an Instron 5969 electromechanical testing machine equipped with a 50 kN load cell. The measurement of the elastic modulus (E) were carried out at a crosshead speed of 0.25 mm/min. The strain was monitored by using an Instron model 2620 resistance extensometer, having a gauge length of 12.5 mm. The elastic modulus was measured as secant modulus between strain levels of 0.05% and 0.25% according to ISO527. In case of rubbery materials such as PVA, where the blade type extensometer couldn't be applied to the specimen, the deformation was measured with a long travel extensometer Instron 2603 and the elastic modulus was calculated

from 1% to 10% of strain. Tensile tests at break were performed without any extensometer to avoid possible damages to it; the stress at break and the deformation at break were determined. At least five specimens for each sample were tested and the experimental conditions are reported in Table 5.

Table 5. Experimental conditions for quasi static tensile test for the evaluation of the mechanical properties at break.

Sample	Crosshead speed
F_PVA	100 mm/min
3D_PVA	100 mm/min
F_PLA	10 mm/min
3D_PLA	10 mm/min
PLA_LNC (film samples)	100 μm/min
F_PHBH	10 mm/min
3D_PHBH	10 mm/min

3.5.12. Creep test

Creep measurements are of great practical importance in any application where polymeric materials must sustain loads for long periods of time and maintain their dimensional stability. The creep test permitted to evaluate the effect of the fillers on the resistance to deformation under constant stress and temperature. The analysis was performed with a TA Instrument DMA Q800 with an applied stress of 1 MPa at a temperature of 30 °C for a period of 60 minutes on 3D printed specimens with dimensions of 20x5x1 mm^3 or on filaments with diameter of 1.75mm and length of 20 mm.

The total creep compliance in isothermal tensile creep in the linear viscoelastic region, D(t), is generally considered as consisting of two components, D_{el} that represents the elastic response that it is instantaneous and reversible and $D_{ve}(t)$ that denotes the time-dependent viscoelastic answer, if no plastic deformation is produced during the creep test [143]:

$$D(t) = D_{el} + D_{ve}(t) \qquad \text{Eq 5}$$

To model the viscoelastic creep response, Findley's model is frequently adopted to fit the experimental data. This model can be obtained by expanding the Kohlrausch–Williams–Watts (KWW) model, generally described by a Weibull-like function as a series and ignoring all but the first term [47]:

$$D(t) = De + k\, t^n \qquad \text{Eq 6}$$

where D_e is the elastic instantaneous creep compliance, *k* is a coefficient related to the magnitude of the underlying retardation process and *n* is an exponent tuning the time dependency of the creep process.

Chapter IV

4. Polyvinyl alcohol reinforced with cellulose

Part of this chapter has been published in:

Cataldi, A.; Rigotti, D.; Nguyen, V. D. H.; Pegoretti, A.,

"Polyvinyl alcohol reinforced with crystalline nanocellulose for 3D printing application",

Materials Today Communications, 15, (2018), 236-244.

4.1. Introduction

This chapter is focused on the production of hydro soluble and fully biodegradable composite filaments and their usage in fused deposition modeling. Poly (vinyl alcohol) (PVA) is recognized as one of the very few vinyl polymers soluble in water also susceptible of ultimate biodegradation in the presence of acclimated microorganisms [48]. PVA could be used in a wide range of applications. However, PVA is highly hygroscopic and this feature spoils its mechanical properties thus limiting its possible applications [144]. PVA is used in FDM technology as vanishing support material for overhanging parts because it can be removed easily from the object by water dissolution without any machining process. Hydrophilicity and hydro solubility of PVA, in particular, triggered also increasing interest in the biomedical field. Polyvinyl alcohol / hydroxyapatite scaffolds made with FDM technology exhibited a suitable porosity for promoting osteo-conduction and osteo-integration as reported by Cox et al. [65]. The research on PVA in 3D printing is manly focused on pharmacology application in the last few years due to the opportunity of producing 3D structured tablets with tailored geometries and density, thus the release concentration profile can be finely tuned [66-68]. In this way, the introduction of 3D printing for drug delivery can represent a revolution for customizable dosage drug-delivering devices [145].

To improve the mechanical properties and limit the rubber-like behavior of PVA, cellulose was chosen as a reinforcing agent to enhance the stiffness, dimensional stability and thermal properties of PVA. At the same time the aim was to preserve its biodegradability in order to expand the field of applications of this green polymer. In this chapter, the extrusion and subsequently the 3D print of biodegradable nanocomposite made of polyvinyl alcohol and nanocellulose are presented. At the end of the chapter, the main properties of 3D printed PVA-CNC composite samples are compared to a simpler biodegradable composite material made by PVA – micro-cellulose.

4.2. Experimental

4.2.1. Preparation of 3D printable filaments

PVA and PVA / cellulose composite were prepared by solution casting. PVA was dissolved under magnetic stirring in distilled water at 80°C for 2 hours to obtain a 6 wt% solution. The obtained PVA / water solution was mixed with increasing amount of micro or nano cellulose solution in water by mechanically mixing with a homogenizer (Dispermat® FI SIP) for 5 min at 2000 rpm and sonication for 3 min using a 14mm tip at 30% of the maximum power. The so obtained solutions were degassed before poured into silicon molds at 50°C for 72 hours to remove the water. At the end, plates were obtained with an increasing content of cellulose from 0 to 10 wt%. These plates were reduced in a powder form with a Piovan RN166 grinder and dried at 50°C for 24 hours. The so obtained powder was used to feed a single screw extruder (Estru 13, Friul Filiere SpA, Buia, Italy). The temperature profile was increased from 100°C in the feeding zone to 175°C in the die zone. Under these selected processing conditions, continuous filaments were obtained with various concentration of cellulose and with a diameter of 1.7 ±0.1 mm suitable to be used in a commercial 3D printer machine based on FDM technology.

4.2.2. 3D printing by fused deposition modeling

The specific printing parameters selected for this material were i) a nozzle temperature of 230°C, ii) a bed temperature of 40°C, and iii) a deposition rate of 40 mm/s chosen to provide a good flowability of PVA even with a 10 wt% concentration of CNC. For as the use of MCC is concerned, it was not possible to print specimen with a content higher of 5wt% due to increase in viscosity.

4.2.3. Sample designation

All micro- and nanocomposites were designated indicating the type of sample (filament or 3D print), the matrix, the type of filler and its amount.

Table 6. Sample designation.

Sample	Type	Filler	Filler (wt. %)
F_PVA	Filament		0
F_PVA_02CNC	Filament	Crystalline nanocellulose	2
F_PVA_05CNC	Filament	Crystalline nanocellulose	5
F_PVA_10CNC	Filament	Crystalline nanocellulose	10
F_PVA_01MCC	Filament	Microcellulose	1
F_PVA_03MCC	Filament	Microcellulose	3
F_PVA_05MCC	Filament	Microcellulose	5
3D_PVA	3D print		0
3D_PVA_02CNC	3D print	Crystalline nanocellulose	2
3D_PVA_05CNC	3D print	Crystalline nanocellulose	5
3D_PVA_10CNC	3D print	Crystalline nanocellulose	10
3D_PVA_01MCC	3D print	Microcellulose	1
3D_PVA_03MCC	3D print	Microcellulose	3
3D_PVA_05MCC	3D print	Microcellulose	5

4.3. Results and Discussions

4.3.1. Morphology analysis

Morphological features of the cryo-fractured sections of neat PVA and CNC nanocomposite filaments were investigated by FESEM. For the neat PVA matrix (Figure 37a) a smooth and uniform surface can be observed, while for PVA–CNC composites (Figure 37b, Figure 37c and Figure 37d) a high degree of surface corrugation, proportionally to the filler content, can be noticed.

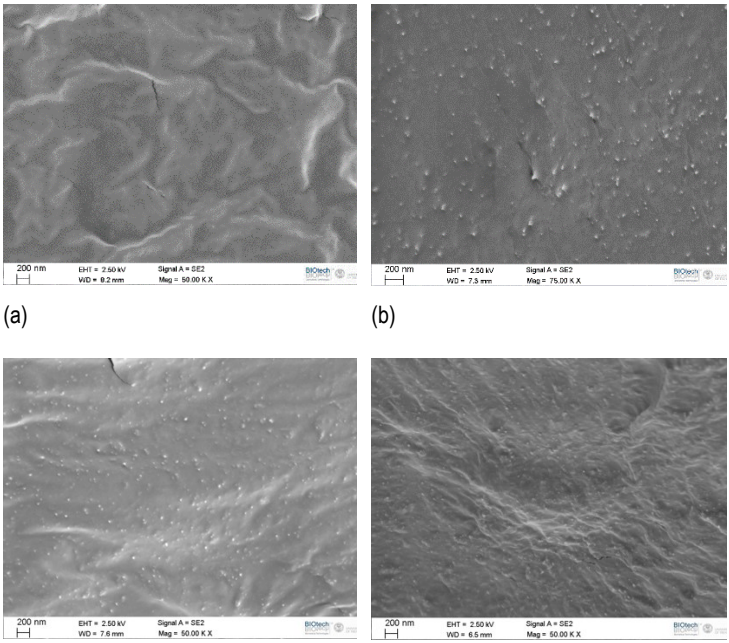

Figure 37 SEM pictures of cryo fractured surface of PVA filaments with the addition of (a) 0 wt%, (b) 2 wt%, (c) 5 wt% and(d) 10 wt% of CNC.

CNC nanoparticles appear homogeneously and evenly dispersed. No appreciable aggregation has occurred during the extrusion process, apart for the sample with 10 wt% of CNC content where a certain filler agglomeration can be noticed. In the latter case, the fracture surface turns from a smooth flat surface to a corrugated one due to the stress concentration of these aggregates leading to a localized early brittle rupture [146, 147]. Lower magnification pictures of cryo-fracture surfaces of neat PVA and nanocomposite are shown in Figure 38, to appreciate the effects of nanocellulose incorporation on the morphology of the printed structure.

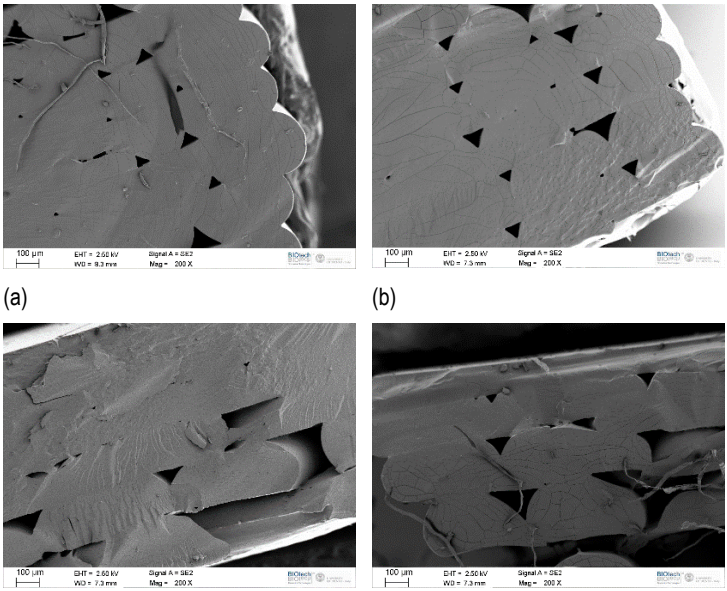

Figure 38. Low magnification SEM pictures of cryo fractured surface of PVA filaments with the addition of (a) 0 wt%, (b) 2 wt%, (c) 5 wt% and(d) 10 wt% of CNC.

Aspect ratio of printed filaments inside the sample decreases with the amount of CNC. Filaments cross section changes from circular to oval, this could be due to decrease in the viscosity of the material as confirmed by MFI (Figure 41). Samples printed with the neat polymer show a good spread of the filament and a good adhesion between each other's resulting in a coherent fracture surface with small pores.

Increasing the amount of CNC inside the matrix leaded to an increase in the pore size and a decrease of the contact area of the filament inside the specimen. The effect of nanocellulose incorporation in the fracture behavior of printed structure can be clearly observed in Figure 39, where the fracture surfaces of 3D printed samples after tensile test are shown. With the increasing of filler fraction, a fracture surface was detected that went from a flat one of the neat PVA sample to a disorder one where the filaments are spread and detached from each other. The activation of new fracture mechanisms could be the cause of an enhancement in the stress at break with the increase of CNC as we measure in paragraph 4.3.4.

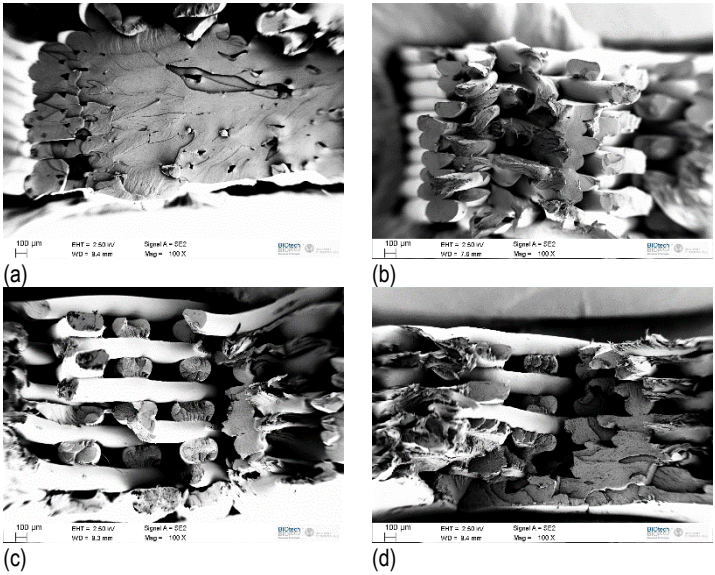

Figure 39. Fracture surface of 3D printed specimen made by neat PVA (a) and with the addition of 2 wt% (b), 5 wt%(c) and10 wt%(d) of CNC respectively.

4.3.2. Moisture absorption

The moisture uptake of neat PVA and corresponding nanocomposite filaments with different amount of filler loading is reported in Figure 40. The kinetic of moisture sorption followed a typical Fickian behavior in all the samples. Analyzing the obtained data, it was possible to evaluate a diffusivity coefficient by considering the slope of the curve of the mass gained by the specimen in function of the square root of time in the first part of the test where the relationship was linear. Diffusion coefficient ranges from 0.0078 $mm^2\ s^{-1}$ for neat PVA to 0.0054$mm^2\ s^{-1}$ for the sample at 10wt% of CNC. Comparing the moisture sorption limit between neat PVA and nanocellulose composite, it is worthwhile to note that the introduction of this filler resulted in a decrease of the final moisture content in all specimens. The equilibrium moisture content of the sample of neat PVA decreased from 9.80 wt% to 7.15 wt% for the sample containing 10 wt% of CNC. Cellulose exhibits hydrophilic behavior and it is obviously prone to absorb water when exposed to humid atmosphere nevertheless a more tortuous path is offered for the diffusion of the water molecules through the polymer matrices after the introduction of nanocellulose. These results are in good agreement with other studies on the effects of addition of CNCs on the moisture sorption of PVA film [148].

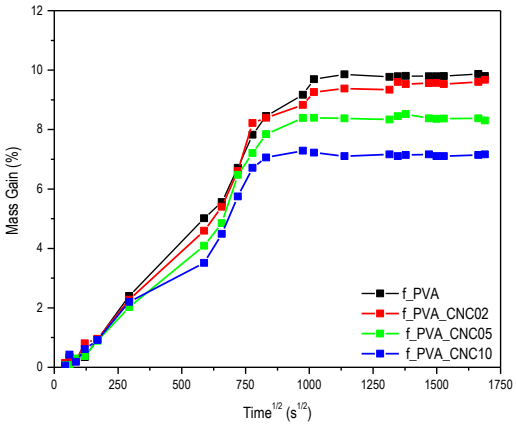

Figure 40. Water absorption for filaments made of PVA and different amount of CNC at room temperature.

4.3.3. Melt flow and thermal properties

Figure 41 represents melt flow index data of neat PVA and nanocomposite filaments at different concentrations of CNC. The results reveal the influence of addition of CNCs on the viscosity of the nanocomposites filaments. MFI decreases drastically as the nanofiller content increases. This behavior is obviously due to the strong interaction of nanocellulose with the PVA matrix. The almost linear dependence is an indication of homogeneous dispersion even at high CNC content.

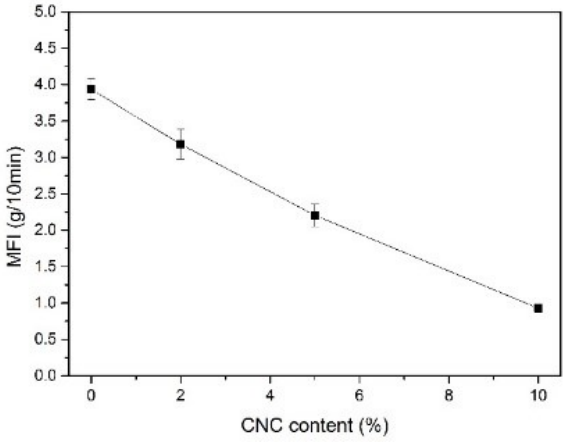

Figure 41. Melt flow index as a function of CNC content.

The effect of CNC on thermal stability of PVA and its composites was evaluated through thermogravimetric analysis (TGA). In Figure 42, TGA curves and derivative (DTG) curves for filaments of neat PVA and nanocomposites are presented.

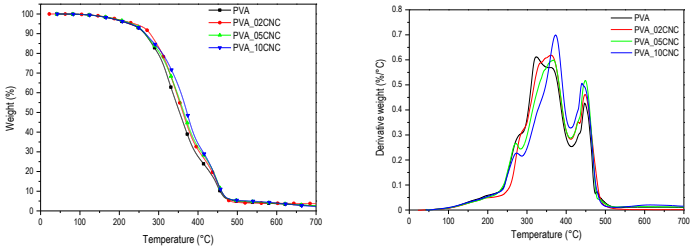

(a) (b)

Figure 42. Thermogravimetric curves (a) and derivative thermogravimetric curves for neat PVA and its nanocomposites filaments.

An initial mass loss can be noticed, and it is related to the evaporation of absorbed water. In the curve of the neat polymer we can clearly distinguish two different steps in the degradation kinetics. From 250°C to 400°C dehydration reactions and formation of volatile products are the main causes of mass loss. The peak for neat PVA at 320°C is shifted to higher temperatures, 360°C – 370°C, with the increase of filler content, enhancing the thermal stability of the composites as compared with the neat PVA. At temperatures higher than 400°C the decomposition of carbonaceous species occurs [54] with a peak in the derivative thermogravimetric curves located at about 440°C for all the composition. This behavior is a positive factor for the subsequent processing step of 3D printing for which high nozzle temperatures are needed to ensure a good quality of final product to overcome the increase in viscosity. It is possible to observe an increase of the thermal stability to degradative mechanisms played by the addition of CNC also if the TGA is done in air. In Figure 43, the results of TGA in air atmosphere are shown regarding filaments made of PVA and PVA_10CNC. In the printing range of temperature (around 240°C), the effect of CNC addition is slightly visible however at higher temperature the thermal resistance to degradation is quite improved by CNC.

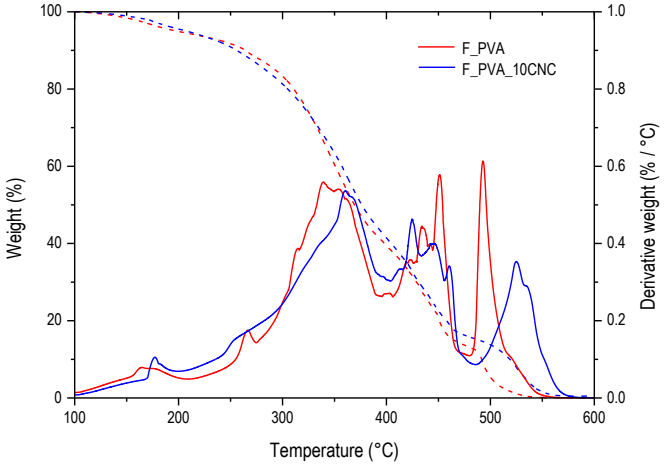

Figure 43. Thermogravimetric curves and derivative curves for neat PVA and PVA_10CNC filaments exposed to a continuos flow of 10ml/min of air (80% N_2, 20% O_2).

Thermal properties of the PVA and PVA/CNC composites filaments were determined using differential scanning calorimetry (DSC). Calorimetry curves of the second heating and the cooling are shown in Figure 44, first heating curves are discarded due to the presence of moisture in the specimen also upon the dehydration process. The glass transition temperature, the melting temperature, the crystallization temperature and degree of crystallinity obtained from the DSC are reported in Table 7. The reference enthalpy of fusion of 100% crystalline PVA was taken equal to 161 J/g [140].

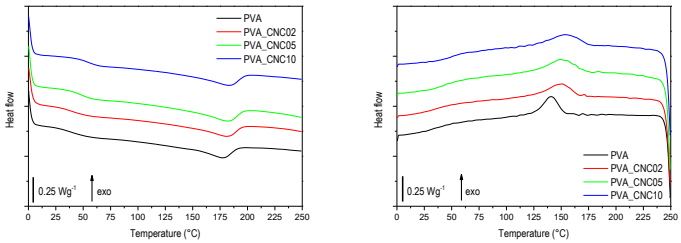

(a) (b)

Figure 44. Differential scanning calorimetry curves on second heating (a) and cooling (b) cycle for neat PVA and PVA nanocomposite filaments.

Table 7. Glass transition temperature, melting temperature and crystallinity content for polyvinyl alcohol and relative nanocomposite from DSC results.

Sample	T_g (°C)	T_M (°C)	T_{CC} (°C)	Crystallinity content (%)
F_PVA	40.7	178.9	143.6	20.9
F_PVA_CNC-02	41.6	180.5	149.5	19.6
F_PVA_CNC-05	41.1	181.4	151.8	17.0
F_PVA_CNC-10	42.1	180.1	150.2	16.9

Similar behavior between the thermal properties of 3D printed samples and composite filaments during the heating and cooling stages is found through DSC. Thermal stability of the material, in terms of transitions temperatures, was increased by the introduction of nanocellulose in the matrix. Glass transition temperature increased during the second heating scan. Melting temperature was not affected by the filler content while the crystallinity fraction decreased as the nanofiller content increased in good agreement with the findings or Roohani et al. [149]. The results of DSC test performed on filaments were properly used to select/optimize the conditions for the following 3D printing

4.3.4. Mechanical properties

Storage modulus, loss modulus and tan delta curves obtained from dynamic mechanical analysis of filament and 3D printed samples are reported in Figure 45. It is evident that the introduction of the nanocellulose leads to an increase of both the storage and the loss modulus in the glassy and in the rubbery region. It is interesting to note that at room temperature an increase of E' and E" of respectively 280% for E' and 250% for E" is observed for a 10 wt% CNC content for the filament samples. 3D printed samples showed the same behavior with an increment in E' and E'' of 290% and 250% respectively with the same amount of nanocellulose. Figure 45c and Figure 45d show the tan δ of the nanocomposites reinforced with various amounts of nanocellulose as a function of temperature for filaments and 3D printed samples respectively. Tan δ decreases with the increasing amount of CNC until glass transition temperature where the trend is reverted with the increase of the values with the increase of filler content. This effect could be explained with the fact that crystalline nanocellulose has a more relevant role on the elastic components than on the viscoelastic behavior of neat PVA at low temperature while this effect is switched at higher temperatures. The increase of CNC content had only a little effect on the transition temperature as revealed by the slightly increase in the temperature of of tan δ peak.

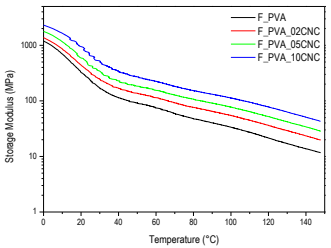

(a)

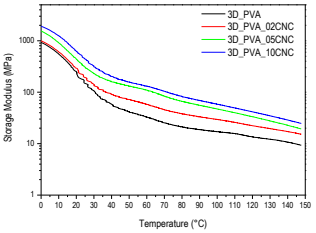

(b)

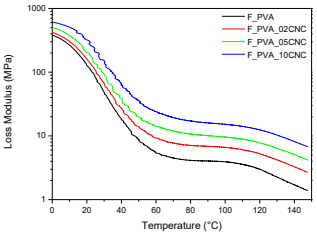

(c)

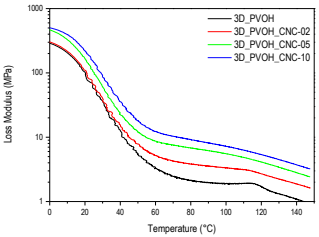

(d)

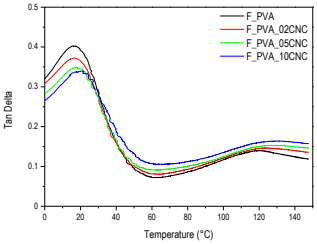

(e)

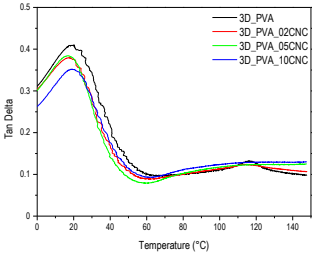

(f)

Figure 45 E' (a), E''(c) and tan delta (e) curves for PVA filaments at different concentration of CNC.

The representative stress-strain curves of examined nanocomposites in form of filaments and 3D printed specimens are reported in Figure 46.

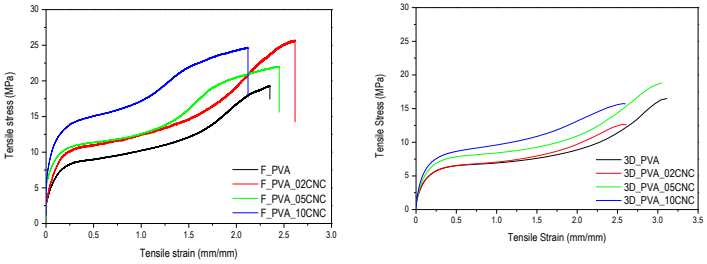

(a) (b)

Figure 46. Representative curves for filament (a) and 3D printed samples (b) of PVA/CNC composites.

The effect of CNC on the elastic modulus (E), tensile strength (σ_B) and strain at break (ε_B) of neat PVA and PVA nanocomposite filaments and 3D-printed specimens are summarized in Table 8.

Both filaments and 3D printed samples manifest an increase in the elastic modulus proportional to the amount of nanofiller. Therefore, despite a decrease in crystallinity content, the stiffening effect played by CNC is prevailing.

Ultimate mechanical properties (stress and tensile energy to break) are improved due to the strong interaction between the matrix and the filler as confirmed by SEM analysis. The maximum reinforcement effect was found for filament at 2 wt% of nanocellulose for which an increase of 81% in the values of TEB and 45% in the stress at break can be observed. An enhancement in tensile properties was observed for 3D printed samples at 5 wt% of CNC where the stress at break shows an increase of 73%.

Table 8. Mechanical properties of filaments and 3D printed components.

	$E_{10\%}$ (MPa)	σ_B (MPa)	ε_B (mm/mm)	TEB (MJ/m^3)
F_PVA	5.6±0.2	17.8±1.01	2.1±0.2	23±3
F_PVA_CNC-02	6.7±0.4	25.8±3.21	2.6±0.1	42±3
F_PVA_CNC-05	9.1±0.6	20.1±2.49	2.0±0.3	28±8
F_PVA_CNC-10	11.6±0.7	21.7±3.82	1.7±0.3	28±8
3D_PVA	2.8±0.1	11.1±0.58	2.9±0.1	25±3
3D_PVA_CNC-02	4.2±0.2	11.6±0.67	2.6±0.1	20±1
3D_PVA_CNC-05	4.9±0.2	19.3±0.69	2.5±0.1	25±6
3D_PVA_CNC-10	5.7±0.2	15.4±0.55	2.3±0.1	24±3

In Figure 47 the isothermal creep compliance curves for filaments (a) and 3D printed samples (b) are presented.

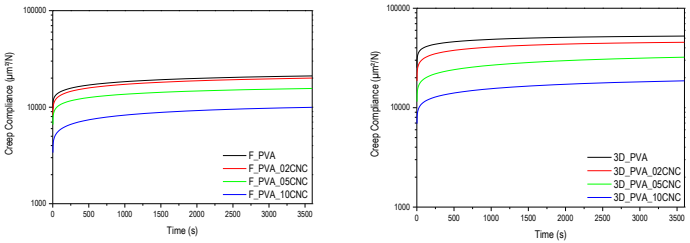

(a) (b)

Figure 47. Creep compliance curves for filament (a) 3D print (b), relative creep compliance value at 3600s (c).

A proportional reduction of the creep compliance with the increase of filler content confirms an improvement of the dimensional stability. A decrease of the creep compliance at 3600 s of 47% for filaments and 35% for 3D printed samples can be observed after the introduction of 10wt% of CNC.

These curves were well fitted by a power law model as confirmed by an R-square higher than 0.99. From the values of the fitting parameters, resumed in Table 9, it was possible to notice a different behavior for the filament and the 3D printed specimen.

Table 9. Fitting parameters of Findley's model on the creep behavior of filament and 3D printed samples nano-composite.

	De (μm²/N)	k (μm²/N)	n
F_PVA	5708 ± 597	4208 ± 493	0.158 ± 0.010
F_PVA_CNC-02	5245 ± 226	3516 ± 166	0.177 ± 0.004
F_PVA_CNC-05	3679 ± 75	3358 ± 62	0.156 ± 0.001
F_PVA_CNC-10	1703 ± 173	1702 ± 131	0.194 ± 0.007
3D_PVA	1724 ± 289	26094 ± 272	0.085 ± 0.001
3D_PVA_CNC-02	2639 ± 1116	16539 ± 952	0.121 ± 0.004
3D_PVA_CNC-05	3824 ± 820	8085 ± 749	0.144 ± 0.008
3D_PVA_CNC-10	5503 ± 68	2100 ± 47	0.226 ± 0.002

The decrease of the creep compliance due to the addition of crystalline nanocellulose was associated to a decrease of the values D_e and k for the filament while for 3D printed samples the reduction was mainly related to a decrease of the coefficient k, that tuned the time-dependent response to the applied stress. This different behavior between filaments and 3D printed samples could be explained by the different structure of printed specimen compared to filaments, that was characterized by a complex 3D structure, made by filaments attached one to each other. In fact, with the increasing amount of CNC the 3D printing became challenging and the interphase between layers and filaments became weaker.

4.3.5. Comparison between 3D printed micro- and nano-composite

In this paragraph, the main properties of 3D printed samples made with PVA reinforced with both micro- and nano-cellulose are presented and compared.

Microcellulose is capable of a lower reinforcing effect if compared to crystalline nanocellulose. This effect could be explained by the lower surface area of a micro filler with a low geometrical ratio with respect to a nano filler with a high surface to volume ratio. In Figure 48, the cryogenic fracture surface of filaments made by PVA and increasing amount of MCC are shown. Cellulose appears as rounded objects with dimensions around 20 microns. A homogeneous distribution of MCC was observed for all the samples and no aggregation has occurred during the filament's extrusion.

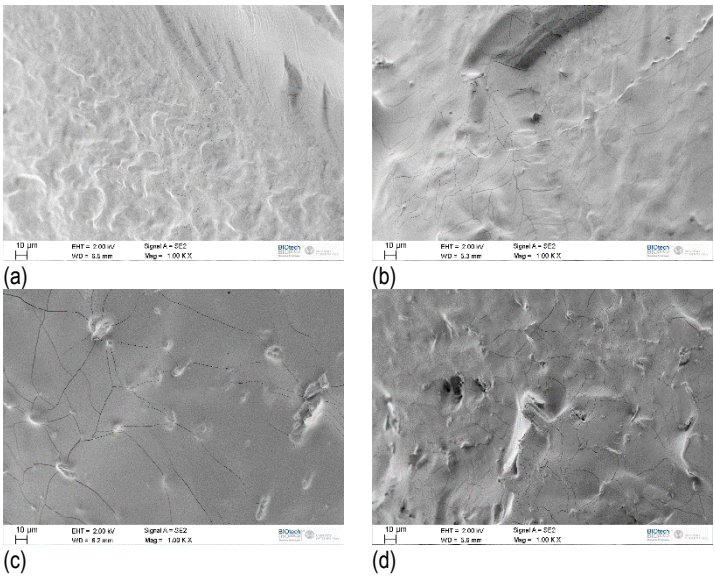

Figure 48. Cryofracture surface of filaments made by neat PVA (a) and increasing amount of MCC: 1 wt% (b), 3 wt% (c) and 5 wt% (d).

Low magnification SEM pictures of the fracture surface of 3D printed specimen with increasing amount of MCC are shown in Figure 49. The overall printing quality decreased with the increasing content of micro filler, due to the increase in viscosity and clogging problems inside the nozzle due to the dimensions of the filler respect to the diameter of the nozzle (0.35 mm).

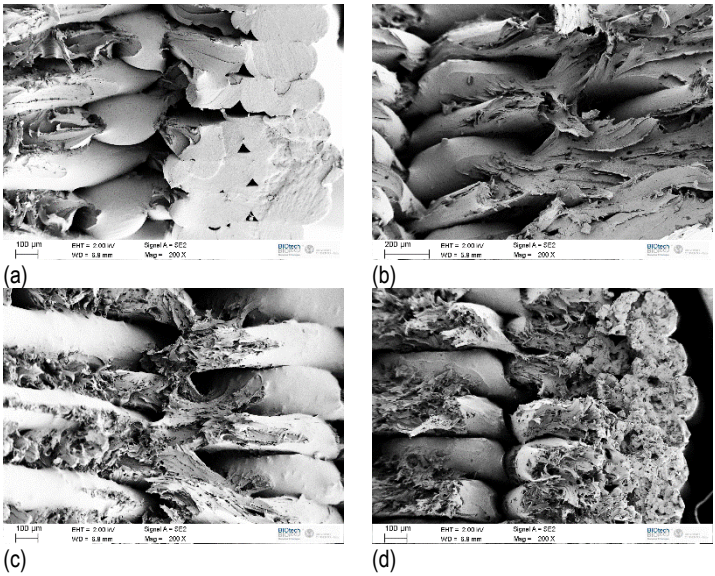

Figure 49. Low magnification SEM pictures of the fracture surface of 3D printed specimen: 3D_PVA (a), 3D_PVA_MCC01 (b), 3D_PVA_MCC03 (c) and 3D_PVA_MCC05 (d).

Viscosity of the PVA filaments is increased with the addition of MCC but not with the same magnitude as found before for CNC. This lower increase in viscosity could be explained by a lower physical interaction between filler and matrix due to the micrometric size of MCC and so to the smaller surface area for same weight fraction compared to CNC.

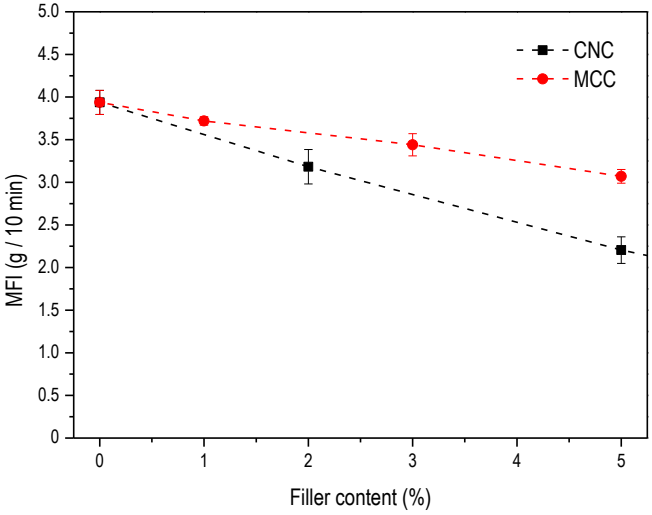

Figure 50. Comparision between Melt Flow Index values for CNC and MCC as a function of filler content.

From DSC analysis on filaments samples, it was possible to observe a pronounced effect on the thermal behavior of the material only at the highest concentration of MCC, as it possible to notice in Table 10. Glass transition temperature went from 40.4°C of the neat PVA to 51.5 of PVA_MCC-05 and the melting temperature from 180.2°C to 186.4°C. Crystallinity of the material remained untouched by the introduction of MCC underlining a poor interaction between MCC and PVA.

Table 10. Glass transition temperature, melting temperature and crystallinity fraction of filaments PVA-MCC from DSC analysis.

	Tg (°C)	Tm (°C)	X c (%)
F_PVA	40.4	180.2	8.4
F_PVA_MCC01	40.5	182.3	8.6
F_PVA_MCC03	41.3	182.1	8.7
F_PVA_MCC05	51.5	186.4	8.7

In Figure 51, it is possible to appreciate the DMA curves for 3D printed neat PVA and MCC composites (a,b,c) and the variation in the values of storage and loss modulus at 23°C induced by the introduction of MCC and CNC (d). Tan delta curves (Figure 51c) confirmed an increase in the glass transition temperature as found in DSC analysis. The tan delta peak shifted from 41°C of the neat PVA to 48°C of PVA_MCC05. This shift to higher temperature with the same magnitude of 7°C was found also for the storage and loss modulus (Figure 51a-b) and it was limited just to the composition with 5wt% of MCC.

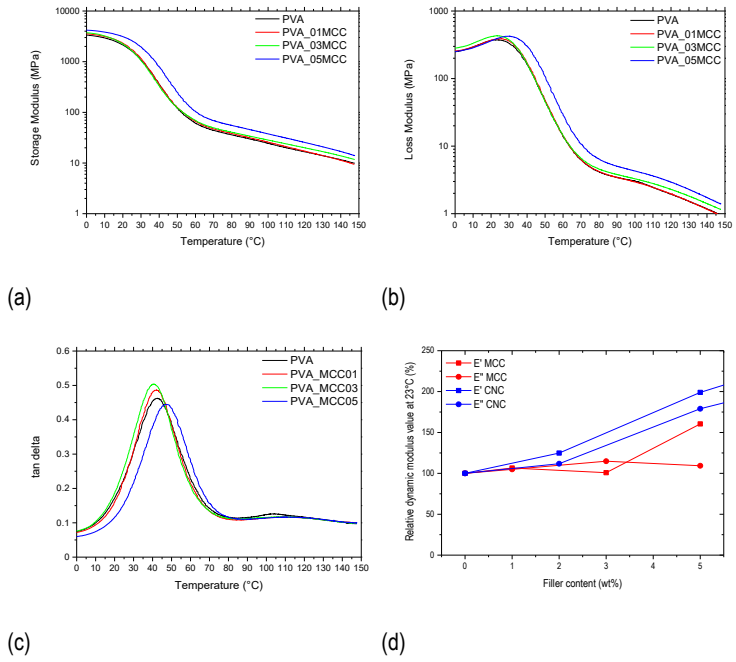

Figure 51. Storage modulus (a), loss modulus (b), tan delta curves for 3D printed micro-composite and comparison of the storage and loss modulus values at 23°c between micro- and nano-composite.

Comparing the values of the storage and loss modulus at 23°C for micro- and nano-composites, it is evident that no changes are visible with low amount of MCC. An increase in storage modulus (60%) is present only with a 5wt% of MCC while an increase (25%) is visible with just 2wt% of CNC.

The relative trend of the modulus chord of 3D printed samples, calculated between 1% to 10% of strain, in function of the amount of micro- and nano-filler introduced in PVA is reported in Figure 52. An increase in stiffness was found also for 3D printed samples with increasing amount of MCC during the tensile test. The stiffening effect is lower compared to the one promoted by CNC and this could be attributed to the lower interaction between micro-cellulose and the matrix in respect with the one between nanocellulose and PVA.

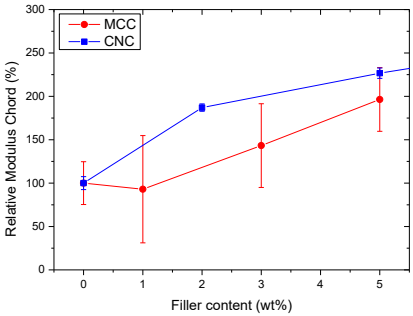

Figure 52. Comparison of the modulus chord measured from 1% and 10% of strain between 3D printed micro- and nano-composite.

As presented in Figure 53, the mechanical properties at fracture of 3D printed samples were slightly affected by the presence of micro-cellulose. At 5wt% of micro-cellulose, the stress at break was increased of 10% while the strain at break was decreased of 20%.

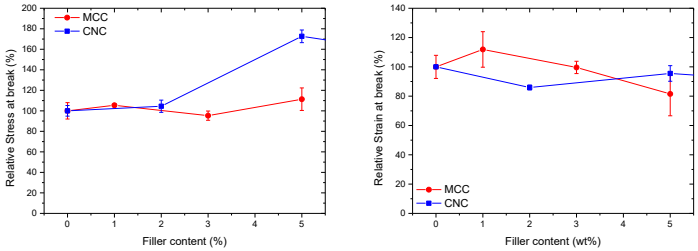

(a) (b)

Figure 53. Comparison of the stress at break (a) and strain at break (b) between 3D printed micro- and nano-composite.

Creep compliance curves of 3D printed PVA-MCC composites were shown in Figure 54. A positive decrease of creep compliance values after 3600s was measured increasing the amount of MCC. This behavior was quite similar as the one reported for the introduction of CNC (Figure 55a) but it differed for the mechanism as the Findley's model suggested. In Figure 55b-53c-53d were reported the parameters of the curves that fitted the experimental data for the micro- and nano-composite 3D printed samples. MCC seemed to influence more the instantaneous creep compliance value (De) in the opposite of CNC. The parameters that related the creep compliance with the time resulted just slightly decreased by the increasing amount of micro filler.

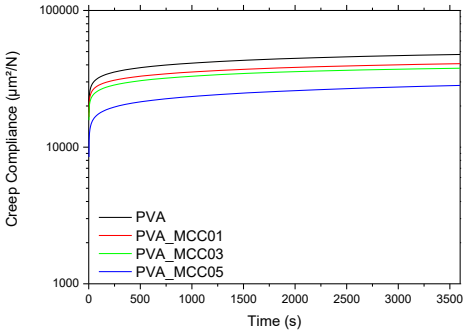

Figure 54. Creep compliance curves for 3D printed PVA/microcellulose composite.

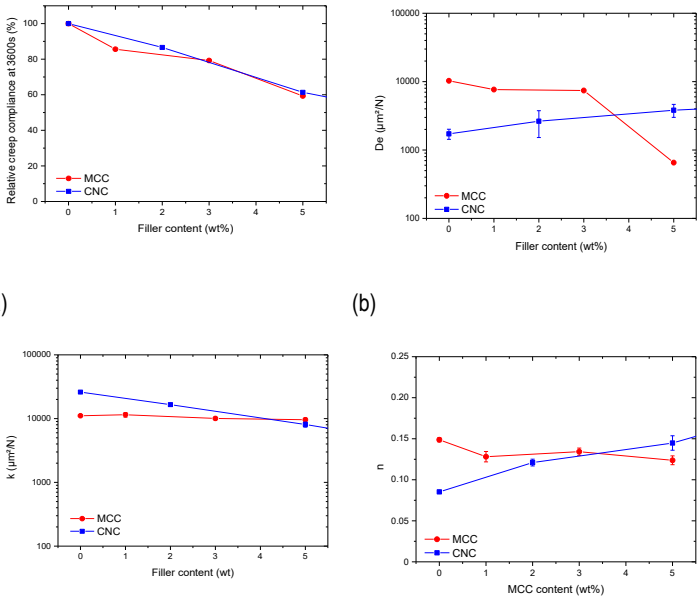

Figure 55. Comparision between PVA-MCC and PVA-CNC 3D printed samples: creep compliance values at 3600s (a), fitting parameters of the Findley's model, De (b), k(c) and n(d).

4.4. Conclusions

The aim of this work was to produce 3D printed biodegradable composites based on poly (vinyl alcohol) (PVA) and cellulose. Different sizes of cellulose were employed: microcellulose and nanocellulose. Microcellulose was mixed with the polymer matrix as received to produce micro-composite and it was the first step to obtain crystalline nanocellulose through a hydrolysis treatment with sulfuric acid. Filaments, suitable to feed a desktop 3D printer, were prepared extruding PVA-cellulose composite materials obtained by solution casting with a single screw extruder. Different compositions were successfully printed despite the high viscosity of the molten filaments that followed the compositions richer in filler.

Electron microscopy revealed that nanocellulose was dispersed well in PVA both in filament and in 3D printed parts. Microstructure of printed sample seems to be highly affected by the viscosity of the material resulting in a non-complete densification when CNC is introduced in the material. CNC was able to lower the humidity absorption of polyvinyl alcohol and to increase the thermal stability of neat PVA shifting the peak of the derivative of TGA curve from 320°C to 370°C at 10 wt% of CNC as seen in TGA. An improve in thermal resistance is confirmed also by DSC which evidenced an increase of the T_g of 3D printed parts from 34°C to 48°C, while the melting temperature remains practically unchanged. The DMA showed that CNC was able to improve the storage and loss modulus of PVA in the temperature range analyzed. In particular, E' and E'' values of 3D printed samples at 23°C increase by 290% and 250% respectively with the 10% of CNC. For both filament and 3D printed specimens, tensile tests highlighted an improvement of the stiffness after the introduction of the CNC. The good adhesion between CNC and PVA increases the toughness of 3D printed material although the lower densification achieved. Stress at break for 3D printed samples increase by 73% when 5 wt% of CNC is added in the matrix and filament at 2 wt% of nanocellulose shows an increase of 81% in the values of TEB and 45% in the stress at break. A decrease in creep compliance corresponding to an increase in dimensional stability was observed with the increase of amount of filler confirm another time the positive behavior on thermal stability. A brief comparation between the reinforcing effect of nanocelloluse and microcellulose in 3D printed samples underlined the less efficiency of MCC respect CNC to limit the rubber-like behavior of polyvinyl alcohol.

Chapter V

5. Polylactic acid grafted maleic anhydride reinforced micro-cellulose in Fused Deposition Modeling

5.1. Introduction

Recently, biodegradable and renewable derived polymers have attracted large attention due to the environmental concerns and sustainability issues associated with petroleum-based polymers. Polymers based on lactic acid (PLA) are the most promising category of plastic materials made from renewable resources due to their good mechanical properties, good workability, excellent barrier properties [71]. PLA is a compostable polymer derived from renewable sources; it has been viewed as a potential material to reduce the societal solid waste disposal problem. Its low toxicity, along with its environmentally green characteristics, could made PLA an ideal material for food packaging and for other consumer products. Nevertheless, some weak points mainly represented by its low ductility, poor toughness, low glass transition temperature, high sensitivity to moisture and relatively low gas barrier should be solved [150, 151].

The use of natural or synthetic fibers is well contemplated to obtain specific characteristics and major improvements of the final properties [12]. Natural materials added to a PLA matrix act mostly as a filler to reduce costs without losing the green benefits of a renewable polymer [152] or to enhance the biodegradability [153]. The incorporation of natural fillers, characterized by a hydrophilic behavior, into hydrophobic thermoplastic polymers typically results in poor dispersion, high viscosity, and low compatibility. The poor interfacial adhesion between the filler and the matrix generally leads to composites with worse mechanical properties [17]. Compatibilizers are widely used to improve the interface between the fillers dispersed in the polymer matrix. Maleic anhydride (MAH) does not homopolymerize under the reaction conditions used in grafting reactions which makes it a god compatibilizing agent. Free radical melt grafting of maleic anhydride on the polymer chains of polyolefins is an efficient and an easy way to improve the compatibility of polymer and different kind of natural fiber from micro to nanometric scale and it is adopted in several studies. Numerous investigations of free-radical grafting of MAH different polyolefins such as: LDPE, HDPE, PP, EPR, EPDM are reported in literature [154]. This reaction is generally achieved in melt processes where the molten polymer is mixed with MAH and with a peroxide initiator, either in an extruder or in an internal mixer. Grafting was effectively performed in an internal mixer at temperature of 190°C and 60 RPM on PLA where dicumyl peroxide was used as initiator at concentration between 0.1 and

0.2 wt% and MAH added at concentration between 0.3 and 3 wt% [155, 156]. Grafting amont of 0.2 – 0.5% was determined by tritation analysis, depending on the content of MAH. A concentration of dicumyl peroxide of 1wt% resulted to be an optimal formulation to maximize the grafting process and minimize the possibility of undesired side reactions [157, 158]. For as concern the maleic anhydride content, it was underlined that a content higher than 5wt% resulted in no significant improvements [159].

Organic clays such as montmorillonite [156], bentonite and hectorite [160] are used to improve the mechanical properties of composite. Most often, a proper compatibilizer is added to PLA to promote a better dispersion of non-polar organoclay. Maleic anhydride is a common choice to produced high values composites starting from PLA and agricultural wastes. For example, rice husk was an interesting opportunity due to its low cost, renewability, biodegradability and low density. Tsou et al. proposed a possible way to recycle it and incorporate this waste material in PLA to produce green composites through the modification of PLA via reaction grafting in the melting state with MAH [161]. Zhu et al. conducted an extensive investigation on the possibility to use soy protein, an agricultural residue of the soybean oil crushing, as a filler to be compounded with PLA grafted MAH to reduce the total cost while increasing the degradation rate of the composites [162]. The hydrophilic functionalization with maleic anhydride was studied to improve the compatibility between PLA and wheat straw by Nyambo et al. [163]. Both PLA and starch are brittle components and lack of chemical compatibility, this results in a brittle composite with low strength, which could be improved by introducing MAH as a compatibilizer as demonstrated by Zhang et al. [164, 165]. They proved that the mechanical properties of PLA/starch composites are improved with just 1wt% of MAH. In fact, PLA/starch (55/45) composite reached a tensile strength of 52.4 MPa, 20% more that the materials without MAH and similar to the neat PLA.

In this chapter, the application of polylactic acid in Fused Deposition Modeling will be discussed. Particular attention will be given to the possibility of producing composite materials with PLA and micro crystalline cellulose (MCC). The first part will be focused on the opportunity of grafting maleic anhydride (MAH) on the PLA backbone to improve the adhesion between PLA and MCC and so the mechanical properties. Two composition, one with just PLA and MCC and another one with PLA grafted MAH plus MCC will be chosen as a starting point to produce filaments suitable to feed a 3D printer. In the second part, the results on 3D printed samples and the effect of presence of MAH will be discussed.

5.2. Experimental

5.2.1. Compounding

Both PLA pellets and microcrystalline cellulose powder were dried in a ventilated oven at 50°C for 24 hours before being processed. PLA with various amounts of microcrystalline cellulose were melt-compounded in a *Thermo Haake* internal mixer at a temperature of 165°C, with a revolution speed of the rotors of 60 RPM and a mixing time of 15 minutes.

Grafting of maleic anhydride (MAH) on the backbone of PLA (PLAgMAH) was performed via radical grafting directly during the melt compounding process with the presence of dicumyl peroxide (DCP) as a radical initiator, following a procedure well described in literature [155]. The PLA was melted for 2 minutes and then DCP was added and mixed for 3 minutes to reach a ratio of 1:10 DCP/MAH. The reaction with MAH in quantities from 1wt% to 10wt% continued during mixing for 5 minutes. At the end, MCC was added and mixed for another 5 minutes. The first step of grafting is the formation of primary radicals via the decomposition of dicumyl peroxide, which then initiates PLA macroradicals (PLA*) by a hydrogen extraction mechanism. The macroradicals subsequently react with maleic anhydride. The grafting reactions are schematically shown in Figure 56.

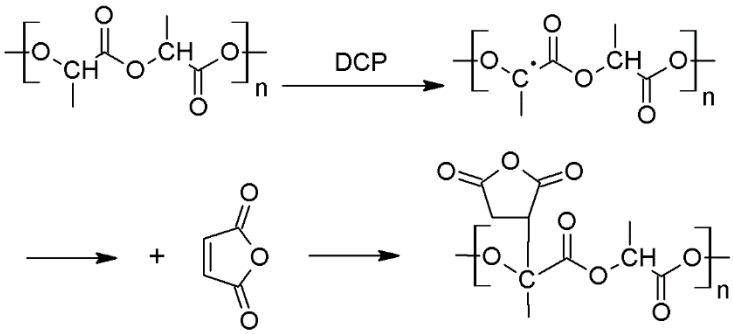

Figure 56. Possible mechanism of grafting MAH on PLA.

A preliminary characterization was done on ISO 527 dumbbell specimen type 1BA obtained by compression molding at 200°C with a pressure of 3.8 MPa for 10 min in a Carver hot press, to produce square sheets of composite samples with an average thickness of 1.0 mm. Specimen 1BA were cut from these sheets with a punch die.

5.2.2. Filament extrusion

PLA compounded with 10wt% of MCC and PLA grafted with 1wt% of MAH compounded with 10wt% of MCC were grinded and used as masterbatch material to be mixed with neat PLA powder to desired microcellulose concentration of in the filaments. The filaments were obtained by using a 3Devo single screw extruder whose scheme is reported in Figure 57. It was characterized by a nozzle of 3 mm in diameter and an optical encoder to measure the diameter of the extruded filament that allowed an automatic adjustment of the drawing speed to maintain a stable diameter. With this feature, an average diameter of 1.75 ± 0.04 mm was obtained (Figure 58). A temperature profile of 170°C, 190°C, 185°C and 175°C in the die zone and a rotation speed of 5RPM were chosen. Neat PLA, PLA compounded with MCC and PLA grafted MAH compounded with MCC filaments containing from 1wt% to 10 wt% of microcellulose were produced via extrusion.

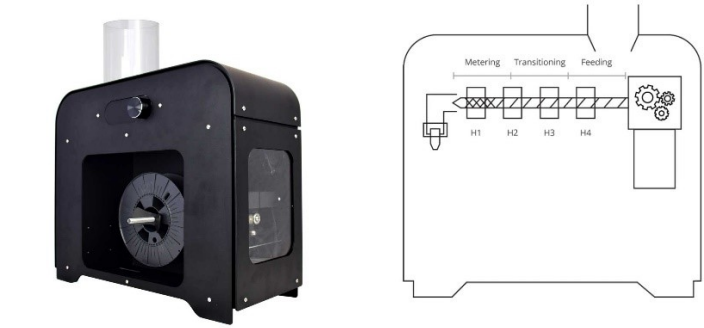

(a) (b)

Figure 57. 3Devo extruder (a) and its scheme (b).

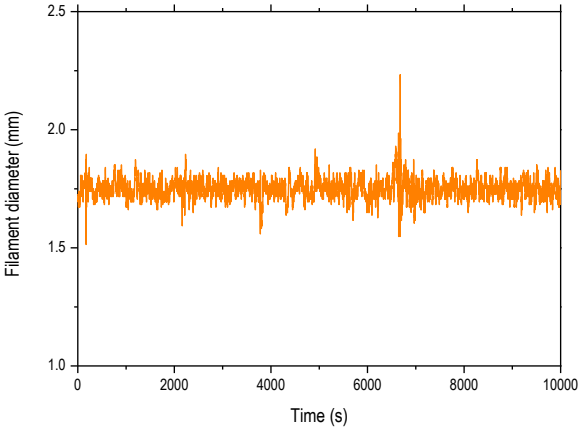

Figure 58. Filament diameter during extrusion.

5.2.3. 3D printing by FDM

Filaments were printed using a Sharebot 3D printer Next Generation based on FDM. The specific printing parameters selected for this material were: a nozzle temperature of 220°C, a bed temperature of 40°C and a deposition rate of 40 mm/s.

5.2.4. Sample designation

As mentioned before, the first part of this experimental work, deals with the research of an optimal ratio between PLA, maleic anhydride and microcrystalline cellulose and the characterization of compression molded samples. The samples are labeled according to Table 11, clearly indicating the amount of MAH and MCC.

Table 11. Compression molded sample codification

	PLA (wt%)	MAH (wt%)	MCC (wt%)	DCP (wt%)
PLA	100	0	0	0
PLAgMAH01	98.9	1	0	0.1
PLAgMAH01_MCC01	97.9	1	1	0.1
PLAgMAH01_MCC02	96.9	1	2	0.1
PLAgMAH01_MCC05	93.9	1	5	0.1
PLAgMAH01_MCC10	88.9	1	10	0.1
PLAgMAH02	97.8	2	0	0.2
PLAgMAH02_MCC02	95.8	2	2	0.2
PLAgMAH02_MCC05	92.8	2	5	0.2
PLAgMAH02_MCC10	87.8	2	10	0.2
PLAgMAH05	94.5	5	0	0.5
PLAgMAH05_MCC05	92.5	5	2	0.5
PLAgMAH05_MCC10	84.5	5	10	0.5
PLAgMAH05_MCC20	74.5	5	20	0.5
PLAgMAH10	89	10	0	1
PLAgMAH10_MCC10	79	10	10	1
PLAgMAH10_MCC20	69	10	20	1

In the second part, micro composite filaments and 3D printed dumbel specimens made of PLA and MCC are compared with the ones of PLA grafted MAH and MCC. These samples are labeled as follow (Table 12), for the sake of simplicity, only the MCC amount is clearly reported and the content of MAH will be 1/10 of the wt% of MCC.

Table 12. Filament and 3D printing codification

	PLA (wt%)	MAH (wt%)	MCC (wt%)	DCP (wt%)
PLA	100	0	0	0
PLA_01MCC	99	0	1	0
PLAgMAH_01MCC	98.89	0.1	1	0.01
PLA_03MCC	97	0	3	0
PLAgMAH_03MCC	96.67	0.3	3	0.03
PLA_05MCC	95	0	5	0
PLAgMAH_05MCC	94.45	0.5	5	0.05
PLA_10MCC	90	0	10	0
PLAgMAH_10MCC	88.9	1	10	0.1

5.3. Preliminary characterization

FTIR is an effective technique to analyze the structures of maleated polyolefins. In fact, the presence of MAH grafted on PLA backbone can be identified by comparing the FTIR spectra of PLA extruded with and without MAH and DCP.

Figure 59 showed the FTIR spectra of neat PLA and PLA grafted with 1wt%, 5wt% and 10wt% of maleic anhydride and the spectra of neat MAH. It is possible to observe the characteristic band signals of PLA at: 1748 cm^{-1} corresponding to the stretching vibration of (-C=O); 1450 cm^{-1}, 1380 cm^{-1}, and 1350 cm^{-1} corresponding to the bending vibrations of -CH_3 and -CH; 1265 cm^{-1} related to the stretching vibration of -C-O-C; 1186 cm^{-1}, 1133 cm^{-1} and 1043 cm^{-1} corresponding to the asymmetric and symmetric bending vibrations of -C-O-C and -CH_3 rocking, 955 cm^{-1} related to the C-C stretching vibration and 870 cm^{-1} corresponding to the stretching vibration of -C-COO [159, 166]. No evidence of free MAH, not chemically bonded with PLA, inside the material has been detected from FTIR since no characteristic peaks of MAH are visible in the blend samples. Comparing the spectra of neat PLA and the ones of PLA with maleic anhydride, it is possible to observe the presence of new band of absorption (Figure 60) in particular at: 695 cm^{-1} corresponding to aromatic C-H bending [155]; 821 cm^{-1} corresponding to the out of plane deformation for carboxyl groups from MAH [167]; 1635 cm^{-1} corresponding to the cyclic C-C stretching that might be a confirmation of the chemical interaction between PLA and MAH [159, 167]; 1790 cm^{-1} (appearing as a shoulder due to the overlapping with the very large peak of the carbonyl -C=O stretching of PLA at around 1748cm^{-1}) and 1850 cm^{-1} are assigned to the symmetric and asymmetric stretching of the carbonyl groups of the saturated cyclic anhydride ring of MAH respectively [155, 157, 159, 166]. The absorption peaks are visible only for the highest amount of MAH which is due to the low MAH in the other two samples (1wt% and 5wt%) [166]. These absorption bands demonstrate the successful grafting of maleic anhydride onto the PLA backbone [167].

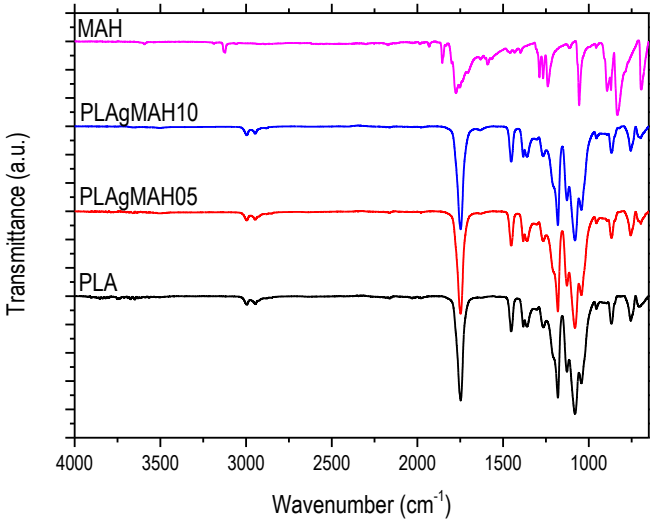

Figure 59. FTIR spectra for neat PLA, PLA grafted with 5wt% and 10wt% of MAH and neat MAH spectra for comparison.

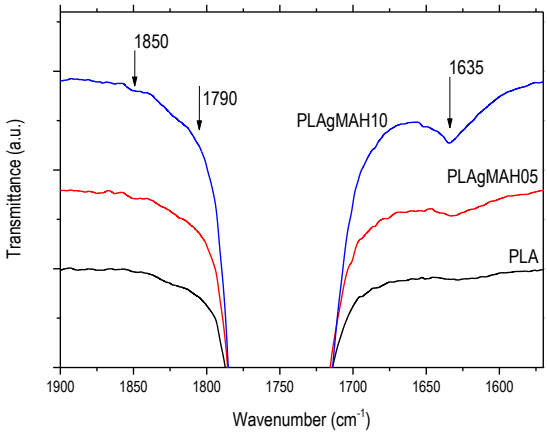

(a)

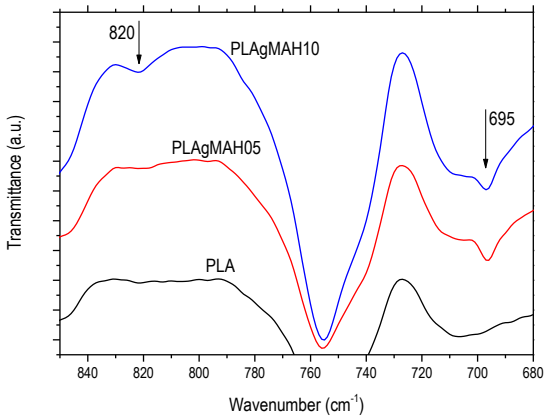

(b)

Figure 60. FTIR spectra for neat PLA and selected PLA grafted MAH focusing on the new peaks related with the grafting of MAH.

The cryogenic fracture surfaces of PLA with 5wt% of MCC and increasing amount of MAH are shown in Figure 61. Figure 61a highlighted a very weak interface between the neat polymer matrix and the micro-cellulose, this behavior was attributed to a poor chemical interaction between the hydrophobic PLA and the hydrophilic cellulose. Maleic anhydride resulted to be very effective in improving the filler – matrix adhesion. In fact, as it can be appreciated in Figure 61b, a positive enhancement is observed with just a low amount (1wt%) of MAH grafted to the PLA. From SEM microstructural observations, increasing the amount of maleic anhydride did not bring visible improvements since a coherent interface is present even at 1wt% of grafted MAH.

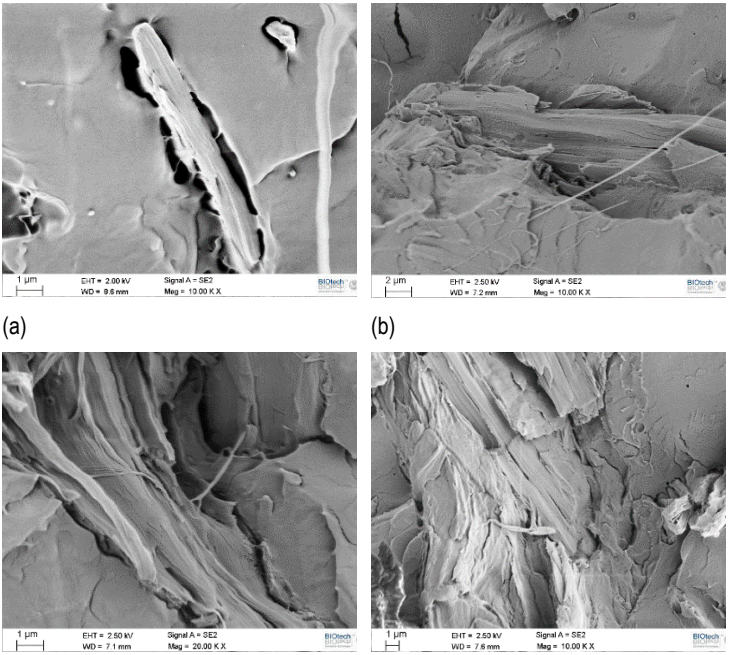

Figure 61. SEM pictures of cryo fractured surface of PLA_05MCC (a), PLAgMAH01_MCC05 (b), PLAgMAH02_MCC05 (c) and PLAgMAH05_MCC05 (d).

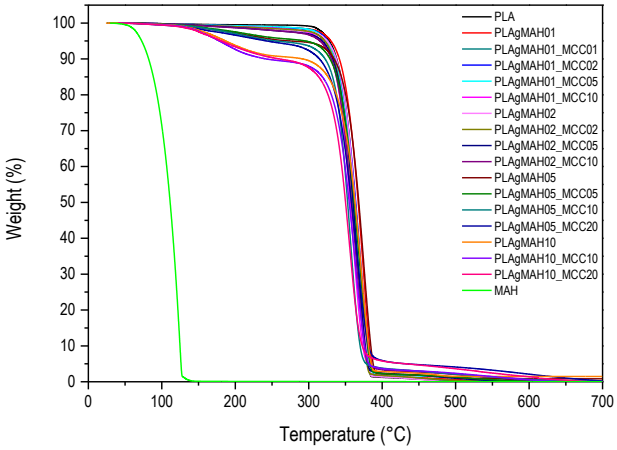

(a)

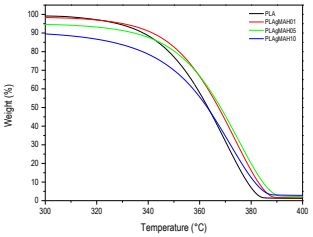

(b)

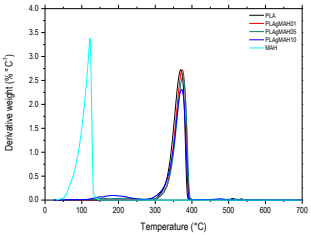

(c)

Figure 62. Thermogravimetric curves (a-b) and derivative curves (c) of neat PLA compared with PLA grafted MAH with different amount of MAH and MCC.

Thermal degradation behavior of the micro composite materials was investigated through thermogravimetric analysis on compression molded specimens. As detected in the TGA thermograms reported in Figure 62. Neat PLA is characterized by a single degradation step centered at 370°C. With the introduction of maleic anhydride, a loss of weight starts to appear at 100°C with the maximum located around 200°C, this effect could be correlated with a lower molecular weight upon the reaction of PLA with DCP. Thermal degradation peak of MAH is centered at 120°C according to Figure 62c, so the step at 200°C for PLAgMAH could also be related to the degradation of free MAH that is not grafted during the melt reaction process since the grafting yield it is reported to be from 0.08% to 0.38% [155]. However, a thermogravimetric – mass spectroscopy analysis should be performed to better investigate this drop in weight. Moreover, Figure 62b evidenced an increase of the onset degradation temperature when MAH was added to PLA, this effect could be explained by chemical crosslink between PLA radicals upon the reaction with DCP as evidenced in literature [155, 157, 166].

Thermal properties of the neat PLA and PLA grafted MAH / MCC composites were determined using differential scanning calorimetry (DSC) and curves for second heating and cooling scan are reported in Figure 63. The glass transition temperature, the cold crystallization temperature, the melting temperature and maximum crystallizable degree values obtained from the DSC are reported in Table 13.

. In Figure 63, the effects of maleic anhydride on the thermal transitions of the micro composite materials can be clearly detected. The reduction of Tg could be attributed to chain branching due to a grafting reaction between PLA and MAH, resulting in an increase of segmental mobility of PLA chains. The decrease of Tg could be also explained by the decrease of molecular weight due to the formation of PLA radicals upon the introduction of DCP as found in a similar study by Hwang et al. [155]. The decrease of Tm at higher content of MAH could be again due to a decrease in molecular weight of the polymer due to radicals' reactions but could be also due to the increase in crystallinity. Because PLA with MAH has crystallized faster, crystals will be less perfect giving a lower melting temperature. MAH and MCC played a synergetic effect in rising the capability to crystallize of the polymer matrix due to a nucleating effect of MCC.

Table 13. Glass transition temperature, cold crystallization temperature, melting temperature and crystallizzation fraction for compression molded samples made of PLA and relative composites as detected by DSC results.

	Tg (°C)	Tcc (°C)	Tm (°C)	Xc (%)
PLA	59.7	109.9	170.7	1.4
PLAgMAH01	58.9	104.2	169.3	2.5
PLAgMAH01_MCC01	58.4	104.7	168.3	2.6
PLAgMAH01_MCC02	58.4	101.6	168.8	2.5
PLAgMAH01_MCC05	58.5	107.6	168.3	2.5
PLAgMAH01_MCC10	58.6	103.2	167.4	6.1
PLAgMAH02	57.9	104.1	168.8	2.2
PLAgMAH02_MCC02	57.2	104.1	167.8	2.1
PLAgMAH02_MCC05	56.4	102.7	167.5	3.0
PLAgMAH02_MCC10	56.2	98.9	167.1	11.2
PLAgMAH05	51.8	99.9	166.8	5.0
PLAgMAH05_MCC05	50.1	94.7	164.5	11.2
PLAgMAH05_MCC10	53.5	95.8	165.3	14.3
PLAgMAH05_MCC20	50.9	90.9	164.7	32.9
PLAgMAH10	46.6	86.8	161.5	6.1
PLAgMAH10_MCC10	40.4	85.9	161.4	19.3
PLAgMAH10_MCC20	43.9	86.9	162.9	39.9

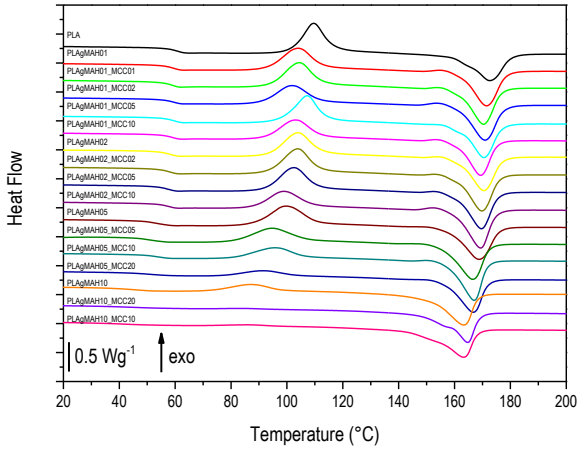

(a)

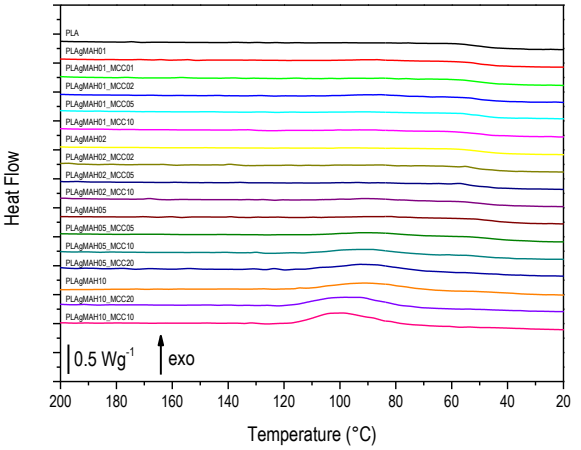

(b)

Figure 63. Differential scanning calorimetry curves on second heating (a) and cooling (b) cycle for neat PLA and PLA microcomposite.

The effect of the incorporation of maleic anhydride on the storage modulus of PLA is shown in Figure 64 evidencing the correlation with DSC. At temperature over the Tg, storage modulus appears slightly higher for low concentrations of MAH while decreases at 5wt% and 10wt% of MAH. The increased crystallinity of material, as found in DSC, raises the stiffness of the material but the possible presence of free MAH and the chain scission in presence of a radical initiator could have lowered the E' for PLAgMAH05 and PLAgMAH10. A first drop in E' is found at glass transition temperature and this step is shifted to lower temperatures as the maleic anhydride content increases due to plasticizing effect. PLA is characterized by a relative difficult to crystallize [168], the presence of a plasticizer, such as in this case MAH, promotes the molecular movements and so the crystallizability of the material. Tcc decreased with the increasing amount of MAH and at this temperature it is possible to notice an increase in the storage modulus of the material.

In Figure 65 are shown the storage modulus and tan delta curves in function of temperature for PLA with and without MAH and relative micro-composite materials while in Table 14 are resumed the main results. The nucleating effect of MCC increases the crystallinity of the material and so the stiffness. However, the introduction of MCC at low amount of MAH is also able to slightly shift towards higher temperature the drop in storage modulus at glass transition temperature. The addition of MAH moves the tan delta peak towards lower values and lower temperatures due to improved molecular mobility. It also enlarges the tan delta peak, this could be due to a broader dispersion of polymer chain lengths after chain scission.

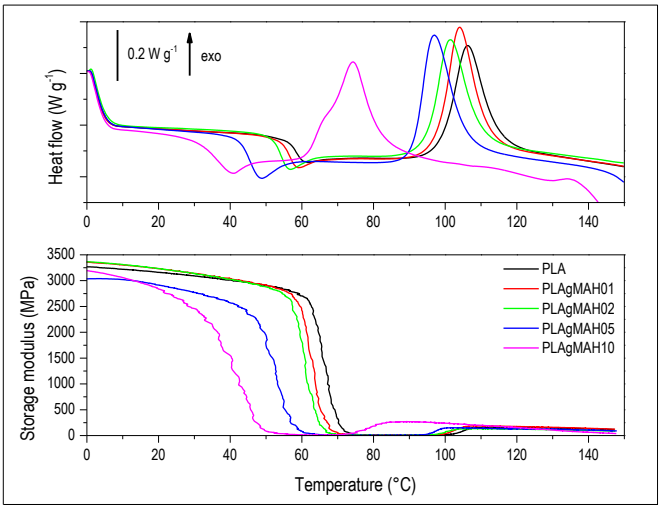

Figure 64. Storage modulus from DMA and DSC curves for PLA grafted with MAH.

Table 14. Storage modulus at 25°C, temperature and value of tan δ peak according to DMA.

	Storage Modulus @ 25°C (MPa)	Tan δ peak (°C)	
PLA	3125	70.9	2.27
PLAgMAH01	3187	70.1	1.73
PLAgMAH01_MCC01	3320	72.6	2.38
PLAgMAH01_MCC02	3194	72.9	1.91
PLAgMAH01_MCC05	3324	73.5	2.07
PLAgMAH01_MCC10	3380	73.1	2.01
PLAgMAH02	3184	68.7	1.95
PLAgMAH02_MCC02	3380	70.5	2.38
PLAgMAH02_MCC05	3287	73.8	2.05
PLAgMAH02_MCC10	3581	70.5	2.03
PLAgMAH05	2846	60.9	1.26
PLAgMAH05_MCC05	3148	63.4	1.21
PLAgMAH05_MCC10	3661	63.7	1.37
PLAgMAH05_MCC20	3805	65.1	1.29
PLAgMAH10	2662	48.8	0.95
PLAgMAH10_MCC10	3072	51.6	0.97
PLAgMAH10_MCC20	3271	60.5	0.88

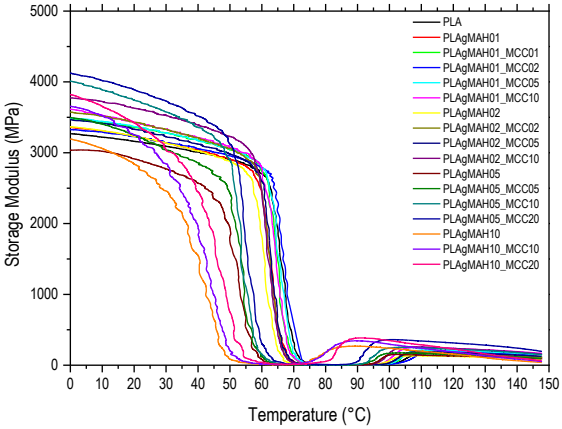

(a)

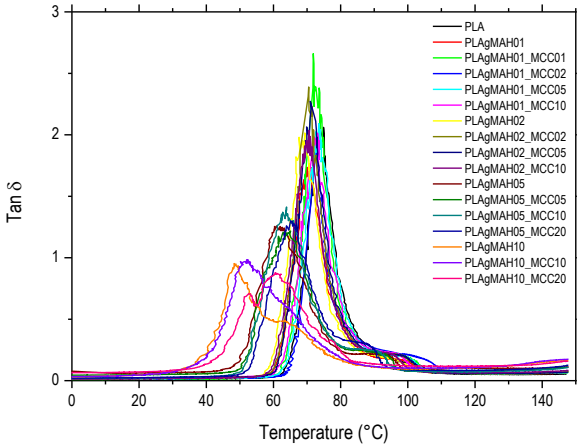

(b)

Figure 65. Storage modulus (a) and tanδ (b) curves for compression molded specimen of PLA and PLA grafted MAH /MCC.

Mechanical properties, such as elastic modulus, stress at break, strain at break and energy at break of neat PLA and micro composite dumbbell specimen were evaluated trough tensile test and the results are graphically summarized in Figure 66. Increasing the amount of maleic anhydride inside the PLA plays the effect to slightly decrease the stiffness of the material. This behavior could be related to the plasticizer effect of MAH. Micro cellulose was able to improve the stiffness of these micro composites and the effect was very noticeable for the samples with the higher content of MAH where the degree of crystallinity is higher. Stress at break was negatively influenced by the presence of MAH as it possible to observe in Figure 66b, where a constant decrease of the strength is recorded, and it is accompanied by an increase in the strain at break. The increase of the amount of microcellulose in the PLA matrix for every concentration of MAH causes an embrittlement of the material, that was clearly evident for samples with the highest concentration of maleic anhydride due to the highest values of deformation at break (Figure 66c).

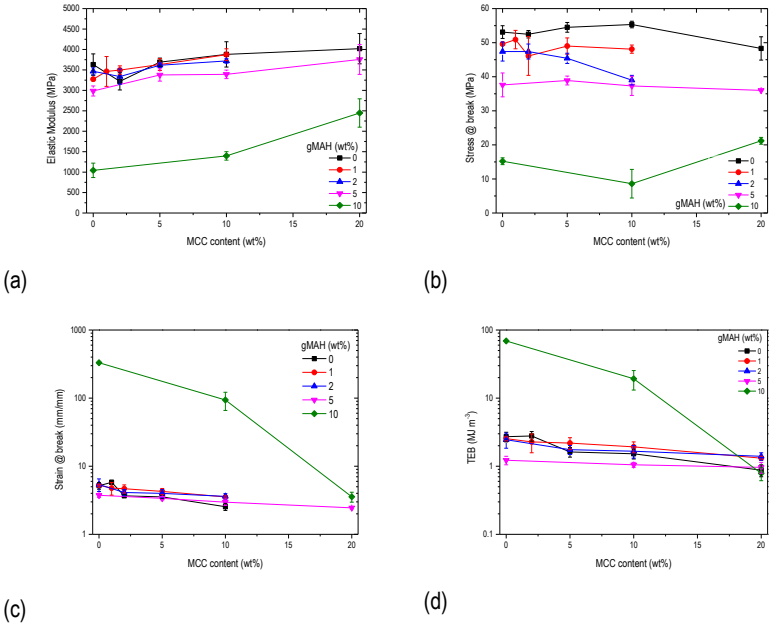

Figure 66. Elastic modulus (a) stress (a) elongation (b) and energy at break (TEB) for different kind of compression molded samples with increasing amount of MCC.

5.4. Results and discussion on filaments and 3D printed samples

Fracture surfaces of 3D printed specimen after tensile tests are shown in Figure 67. Samples of neat PLA and with a low amount of MCC (picture of sample 3D_PLA_MCC01 is not showed for sake of brevity) maintained the shape of the filaments which are constituted and presented a visible deformation prior the fracture with the detachment of the filaments from each other's. Shape of the filaments that compose the 3D printed structure moved from a circular section to an oval and spread one due to the decrease in viscosity as indicated by MFI, this is particular evident for PLA grafted with MAH printed samples. Fracture surface tended to become flat with the increasing amount of MCC, evidencing the transition from a ductile to brittle fracture. This behavior matched with the stiffening effect played by the incorporation of MCC and the increase in crystallinity as found in DSC analysis. MAH, as previously seen, improved the adhesion of PLA / MCC, samples without MAH showed a higher degree of porosity and a poor matrix / filler interphase.

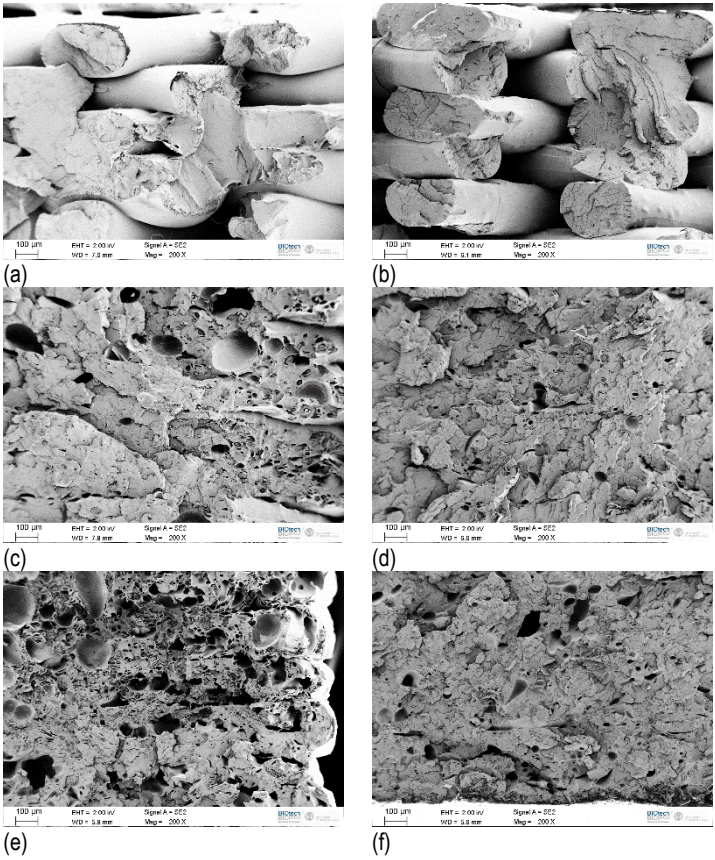

Figure 67. Low magnification SEM pictures of the frature surface of 3D_PLA (a), 3D_PLAgMAH_MCC01 (b), 3D_PLA_MCC05 (c), 3D_PLAgMAH_MCC05 (d), 3D_PLA_MCC10 (e) and 3D_PLAgMAH_MCC10 (f).

A rudimentary evaluation of thermoplastic polymer processing properties is given by the determination of melt flow index (MFI). The results of the MFI evaluation on filaments of PLA and PLA grafted MAH with different amount of microcellulose are presented in Figure 68 and are resumed in Table 15.

The addition of MCC decreased the viscosity of PLA and PLAgMAH. This decrease is related with the amount of MCC, until 3 wt% the values are similar for both PLA and PLAgMAH and then MFI increased rapidly for samples with MAH, suggesting a plasticizer effect of MAH. The increase of MFI with the increase of MCC could be related with the presence of micrometric fillers with a low area over volume ratio and due to the poor interaction between MCC and neat PLA for samples without MAH. Despite the improved interaction between PLA and MCC given by MAH, viscosity still decreased due to the plasticizer effect of MAH that hinder the improved matrix – filler compatibility. However, it is not possible to exclude a decrease in molecular weight of PLA after the reaction with DCP as reported in similar studies [155, 157]. A similar behavior was observed by Barczewski et al., they found an increase in MFI with the increasing content of lignocellulosic material, i.e. micrometric grinded nutshell, in PLA [169]. Yamoum et al. reported an analogous trend when PLA and plasticizers were mixed with carboxymethylcellulose, MFI increased by 5 times with a content of 9wt% of cellulose [170].

According to the work of Shenoy [171], MFI was used to calculate the shear rate inside the capillary rheometer, that was used to measure the MFI. Over this range of shear rate was done a rheometric analysis with a rheometer in plate – plate configuration at 190°C and the results are shown in Figure 69. These results confirmed the decrease of viscosity previously found with MFI with the increasing amount of MCC and MAH. Furthermore, this analysis revealed a shear thinning behavior for neat PLA and the microcomposite materials without MAH at around 100 s^{-1}. Shear rates in the nozzle of 3D printer FDM are commonly in the range of 100 - 200 s^{-1} [172], so the decrease in viscosity played by the incorporation of plasticizer and the shear thinning behavior around 100 s^{-1} are all positive factors that improve the printability of these filaments.

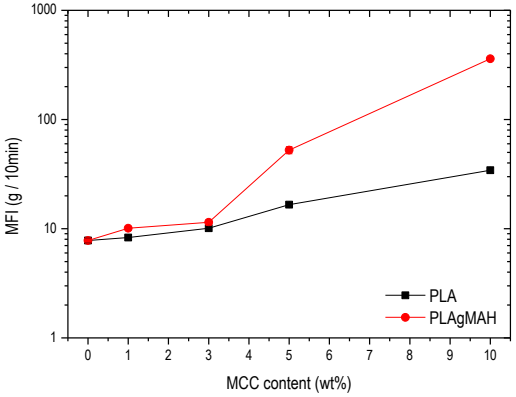

Figure 68. MFI index values for filaments made of PLA and PLA grafted MAH in function of the content of MCC.

Table 15. Density, Melt flow index and Melt volume index values for filaments made of PLA, PLA grafted MAH and MCC.

	Density g / cm^3	MFI g / 10 min	MVI cm^3 / 10 min	Shear rate 1/s
F_PLA	1.24	7.8 ± 0.4	6.3 ± 0.3	15.3 ± 0.8
F_PLA_01MCC	1.24	8.3 ± 0.4	6.7 ± 0.3	16.3 ± 0.8
F_PLAgMAH_01MCC	1.24	10.1 ± 0.4	8.1 ± 0.3	19.8 ± 0.8
F_PLA_03MCC	1.25	10.1 ± 0.4	8.1 ± 0.3	19.8 ± 0.8
F_PLAgMAH_03MCC	1.25	11.45 ± 0.6	9.2 ± 0.5	22.5 ± 1.2
F_PLA_05MCC	1.26	16.6 ± 0.7	13.2 ± 0.6	32.6 ± 1.4
F_PLAgMAH_05MCC	1.26	52.5 ± 3.9	41.8 ± 3.1	103.2 ± 7.6
F_PLA_10MCC	1.27	34.3 ± 1.8	27.0 ± 1.4	67.4 ± 3.5
F_PLAgMAH_10MCC	1.27	> 300	> 235	> 590

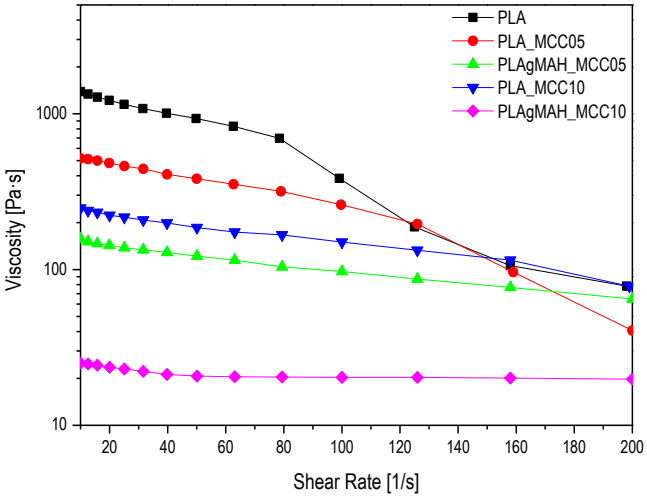

Figure 69. Viscosity in function of shear rate for microcomposite filaments.

In Figure 70a, the thermogravimetric curves for 3D printable filaments made of PLA, MCC and MAH are presented. It is possible to notice the absence of the first loss mass step previously seen in Figure 62a, due to the possible degradation of low molecular radicals during the extrusion process or the degradation of free MAH inside the material. The decomposition temperature is higher than neat PLA for all the samples and PLAgMAH samples show an higher degradation temperature at the same amount of MCC. The chemical bond between PLA matrix and MCC increased the interfacial adhesion and so the thermal degradation temperature increases consequently. [166]

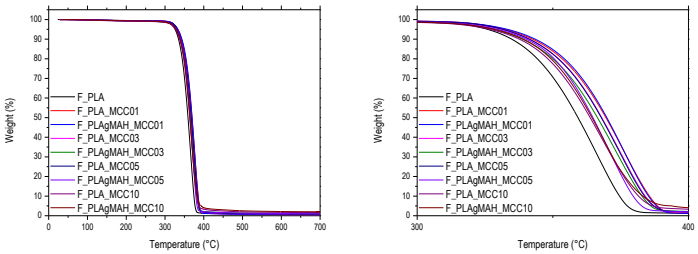

(a) (b)

Figure 70. Thermo degradative curves for 3D printable filaments (a), focus of picture (a) in the range of 300 - 400°C (b).

Thermal properties of the PLA, PLA / MCC and PLA grafted MAH /MCC composite filaments were determined using differential scanning calorimetry DSC. The glass transition temperature, the melting temperature and degree of crystallinity obtained from the DSC are reported in Table 16 while representative DSC curves are shown in Figure 71. The reference enthalpy of fusion of 100% crystalline PLA was taken equal to 93.6 J/g [141]. Crystalline microcellulose slightly modifies the thermal properties of PLA. Microcellulose appears to not affect the glass transition temperature of microcomposite filaments, however, the presence of maleic anhydride grafted on PLA slightly decreases it, due to its low melting temperature. Crystallization temperature (Tc) and crystallinity fraction (Xc) are affected by the introduction of microcellulose and maleic anhydride. In fact, MCC acts as a nucleating agent lowering the crystallization temperature. Maleic anhydride increases the crystallinity fraction with respect to the corresponding PLA-MCC composite filament. This could be caused by the increased mobility of the matrix chain so a better arrangement was possible [166].

Table 16. Glass transition temperature, crystallization temperature, melting temperature and crystallinity content for PLA and relative microcomposite filaments from DSC results of the first heating.

	Tg (°C)	Tc (°C)	Tm (°C)	Xc (%)
F_PLA	59.2	134.0	168.0	1.03
F_PLA_01MCC	59.4	120.5	167.2	1.68
F_PLAgMAH_01MCC	59.5	128.1	168.5	0.71
F_PLA_03MCC	59.5	113.4	170.4	0.86
F_PLAgMAH_03MCC	59.2	117.2	170.4	0.19
F_PLA_05MCC	59.1	113.6	170.3	1.09
F_PLAgMAH_05MCC	58.6	113.2	169.4	2.02
F_PLA_10MCC	59.0	108.2	169.7	2.92
F_PLAgMAH_10MCC	57.3	108.2	167.8	3.16

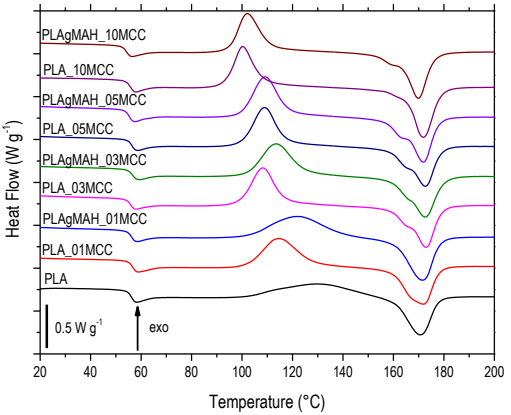

(a)

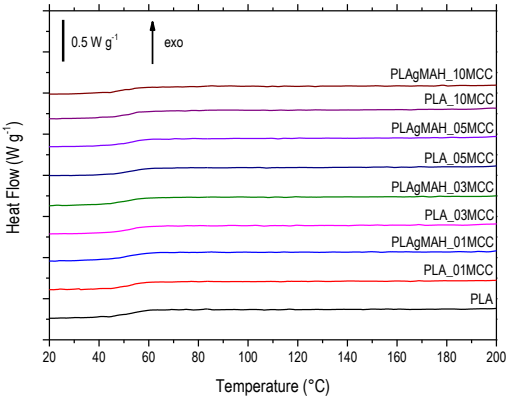

(b)

Figure 71. First heating (a) and cooling (b) DSC curves for PLA and relative microcomposite filaments.

The mechanical properties such as elastic modulus, tensile strength, elongation at break and the R-ratio (chapter 3.4.3) of neat PLA and its relative micro composite 3D printed samples were investigated by tensile test at room temperature, the results are summarized in Figure 72. 3D printed samples showed an increase in the elastic modulus when micro crystalline cellulose is added to the PLA matrix. This stiffening effect could be influenced not only by the higher rigidity of microcellulose with respect to neat PLA, but also by the increase of the crystallinity fraction as previously seen in DSC. The highest values of elastic modulus are found for PLA_01MCC, that had also the highest values of the R-ratio, suggesting that the quality of the 3D printed structure played an important role on the mechanical properties of FDM objects. Maleic anhydride improves the adhesion between the filler and the matrix thus raising the stiffness of micro composite samples. Same trend of the elastic modulus is found for the stress at break while the strain at break slightly decreases with the increasing amount of filler, no effect of the MAH is visible in this case.

R-factor, a possible indicator of the quality of 3D printed specimens, presents a maximum at 1wt% of MCC and then a decreasing trend for higher amount of cellulose due to possible clogging of the nozzle during printing that affect its overall quality.

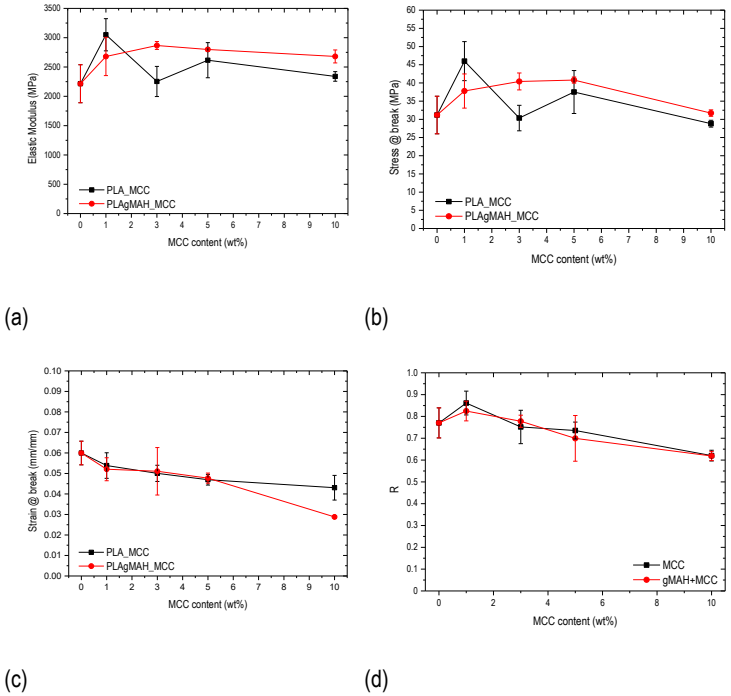

Figure 72. Elastic Modulus (a) stress (a) elongation (b) and energy at break for different kinds of 3D printed samples with increasing amount of MCC.

5.5. Conclusions

The aim of this work was to evaluate the potentiality of polylactic acid / microcrystalline cellulose composites in 3D printing Fused Deposition Modeling to improve the mechanical properties of produced objects and to lower their price.

At first, the effect of grafting maleic anhydride to PLA to improve the adhesion of the hydrophilic cellulose to the hydrophobic polyester chains was investigated. Grafting was done in melt reaction blending and dumbbell specimen obtained by compression molding. Infrared spectroscopy analysis confirmed the grafting of maleic anhydride on the PLA backbone. Electron scanning microscopy revealed that microcellulose was well dispersed in PLA and maleic anhydride was able to enhance the compatibility between filler and matrix resulting in a coherent interface between the two constituents. Thermal degradation of PLA was not affected by the presence of MAH, instead of glass transition temperature, crystallization temperature and melting temperature that were lowered by the increasing amount of MAH.

Storage modulus curves translated towards lower temperatures with the increase of maleic anhydride and evidenced a reduction of stiffness. Storage modulus at 25°C decreased from 3125 MPa of the neat PLA to 2662 MPa at a concentration of 10wt% of MAH. At the same time, the peak of tan δ, that represented the glass transition temperature of the material, at 10wt% of MAH moved from 70°C to 48°C. Moreover, the damping efficiency of the material measured as the max of peak decreased from 2.3 for pure PLA to 0.9 after addition of 10wt% of MAH. Increasing the amount of maleic anhydride inside the PLA matrix had the effect to slightly decrease the stiffness of the material, while the stress at break was sensible reduced by the increasing in concentration not only of MAH but also of MCC.

Filaments were easily produced with a regular diameter of 1.75mm (standard deviation as low as 0.04 mm). Filaments of PLA with different concentration of MCC with and without maleic anhydride were used to feed a 3D printing machine to obtain dumbbell specimens. Tensile tests highlighted that microcellulose in low concentration is able to improve the stiffness (up to 38% and up to 30% with MAH) and the stress at break (up to 48% and up to 32% with MAH) of 3D printed specimens. The maximum in term of stiffness and strength is reached at 1wt% of MCC without MAH, the grafting of PLA with maleic anhydride allow to reach a higher content of cellulose inside the composite shifting the maximum benefits at higher content of MCC (in this case 5wt%).

Chapter VI

6. PLA and nanofibrillated cellulose

6.1. Introduction

With the development of cellulose chemistry and processing technology, the applications of cellulose materials are not limited to traditional fields as engineering materials in ligneous products, paper, and textile industries, but also used for advanced functional applications in the field of biomedical and smart health care, printed electronics, and responsive wearable textiles. With the advantage of sophisticated geometry fabrication and low-cost production, 3D printing technologies have been employed with many materials for a variety of applications.

Nanocellulose was found to be one of the most interesting reinforcing agent for producing green nanocomposites due to their size and the ability to chemically modify the surface and they could be used in a wide variety of applications; foams, adhesives and protective coatings [16-18, 173, 174]. Cellulose could also be used as a component for 3D printing filaments to enhance the mechanical strength of 3D printed products. The hydrophilicity and less thermal stability of cellulose micro/nanoparticles restrict the range of choice of polymer matrix and the processing methods of the composites. The dispersion, distribution, and the interfacial interaction of cellulose particle in thermoplastic composites are essential parts of research and development of the manufacturing process of cellulose enhanced 3D printing matrix.

In this paragraph an example will be given on the development of a nanocomposite material based on commercial polylactic acid (PLA) and nanofibrillated cellulose (NFC) in 3D printing Fused Deposition Modeling. Nanocellulose was obtained through ultrasonication disruption as discussed in 3.2.2. Solution mixing was chosen to obtain a good dispersion of cellulose inside the polymer matrix and to overcome any possible thermal degradation problem related with melt mixing. The effect on 3D printable material in form of filaments and 3D printed specimen after the addition of a low amount of nanocellulose was studied.

6.2. Experimental

6.2.1. Filament preparation

Solution mixing was adopted to produce masterbatch material for the subsequent extrusion. Freeze dried NFC was dispersed in chloroform (0.1g NFC / 10ml CHCl3) and ultrasonicated with a Hielscher UP400S Ultrasonicator (Teltow, Germany) for 5 minutes at 400W in an ice bath to prevent overheating.

PLA was dissolved in chloroform (1g PLA / 25ml $CHCl_3$) and mechanically stirred at 45°C until complete dissolution was reached. The two solutions were then mixed together at 45°C for 3 hours. After a mild sonication in an ultrasonication bath to remove the air bubbles, the solution was poured in a Petri dish and it remained at room temperature for 12 hours and in a ventilated oven at 50°C for 3 hours to permit the evaporation of the solvent. The obtained composite, with a concentration of 3wt% of NFC, was grinded with and without neat PLA to prepare a coarse powder with a final composition of 1wt% and 3wt% of NFC. These powders were used to feed a single screw extruder provided by FriulFiliere (Buia, Italy) with a die diameter of 3mm and filaments of neat PLA and different concentration of NFC were extruded. The temperature profile of the extruder went from 100°C in the feed zone to 150°C in the die.

6.2.2. 3D printing by FDM

A desktop 3D printer provided by Sharebot (Italy), based on Fused Deposition Modeling, was used to print dumbbell specimens with filaments of PLA with increasing amount of NFC. A careful monitoring of the temperatures was required to avoid warping phenomena and the detachment of the printed object from the building plate due to thermal stresses related with the crystallization of the material after the extrusion from the nozzle of the 3D printer. The bed plate was set at 75°C and covered with double-sided tape to increase the adhesion. The temperature of the nozzle was adjusted at 200°C to print the first layer of the specimen and then was decreased to 180°C in the last layer to provide a gradient of temperature inside the object that limited the warping phenomena.

6.2.3. Sample designation

All nanocomposites were designated indicating the type of sample (filament or 3D print) if necessary, the matrix, the type of filler and its amount. 3D_PLA_1NFC refers to the 3D printed sample containing 1wt% of fibrillated nanocellulose.

6.3. Results and discussion

The cryogenic fracture surfaces at increasing magnification of a 3D printed specimen made of PLA and PLA with 1wt% of fibrillated nanocellulose are presented in Figure 73. (Fracture surface of printed specimen loaded with 3wt% of NFC are very similar with the one with 1wt%, so pictures are not reported for sake of simplicity). In the low magnification images (Figure 73a and Figure 73c), it is possible to distinguish clearly the single filaments inside the printed specimen that compose the object and a lower adhesion between layers was found for the specimen loaded with NFC. The lower adhesion and the lower number of contact points between filaments of subsequent layers will led to a decrease in the stiffness of the specimen due to an enhancement of the mobility of single wires. Inside the PLA matrix (Figure 73e) it was possible to discover rounded micro-metric aggregates due to the re-aggregation of the cellulose nanofibers in the freeze-drying process and during the redispersion in chloroform due to its higher superficial energy that are not present in the neat PLA specimen (Figure 73b). These particles owned a very poor interaction with the matrix as highlighted by the absence of a clear interphase. The presence of aggregates increased with the increasing concentration of NFC; this could be responsible of a deterioration of the failure properties of the prepared nanocomposite at the highest concentration. Increasing the magnification (Figure 73f), it is possible to observe a net of nanocellulose filament with diameter around 100nm and few microns in length without any preferential orientation. These filaments possessed a good adhesion with the matrix as evidenced by a large plastic deformation (Figure 73g-h).

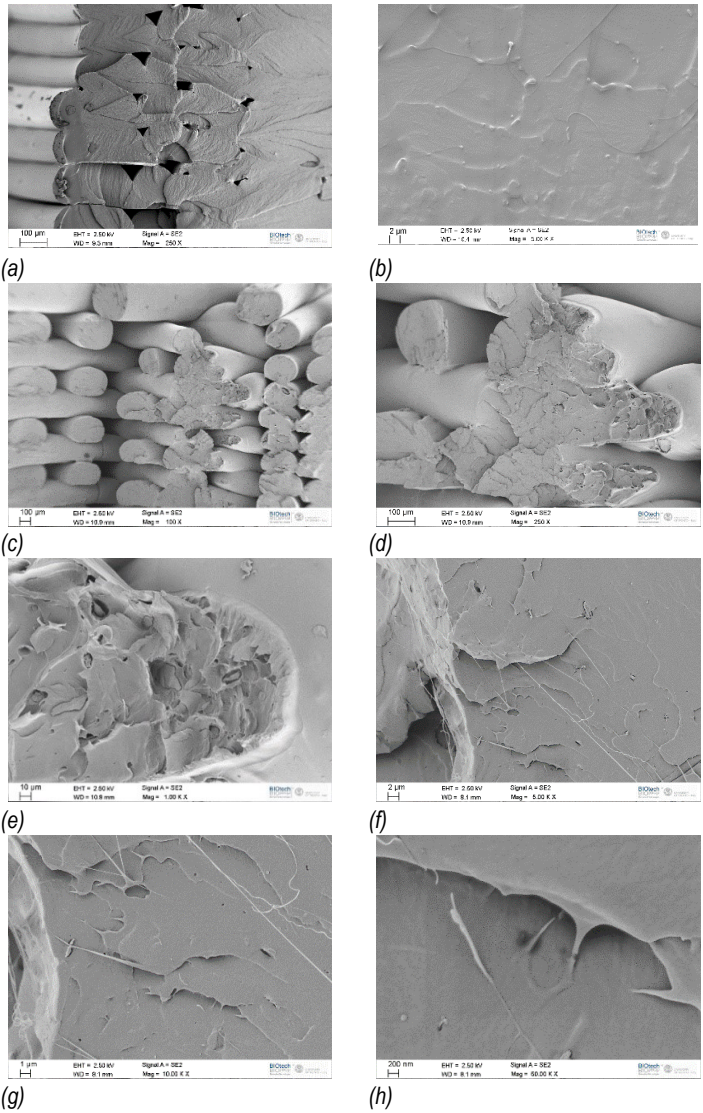

Figure 73. SEM pictures of the cryogenic fracture surface of 3D printed PLA (a-b) and PLA with 1wt% of nanofibrillated cellulose at different magnification (c-h)

The flow behavior of the composite in the molten state is important to characterize the processing properties of the polymer melt and is usually reported by the flow curve relationship between viscosity and shear rate. Figure 74 shows results of the apparent viscosity as a function of the shear rate for the neat PLA and PLA_3NFC composites at a test temperature of 190 °C. Neat PLA and PLA_3NFC exhibited a shear thinning behavior, however the increase in viscosity with the addition of nanofillers could be detrimental for the subsequent step of 3D printing.

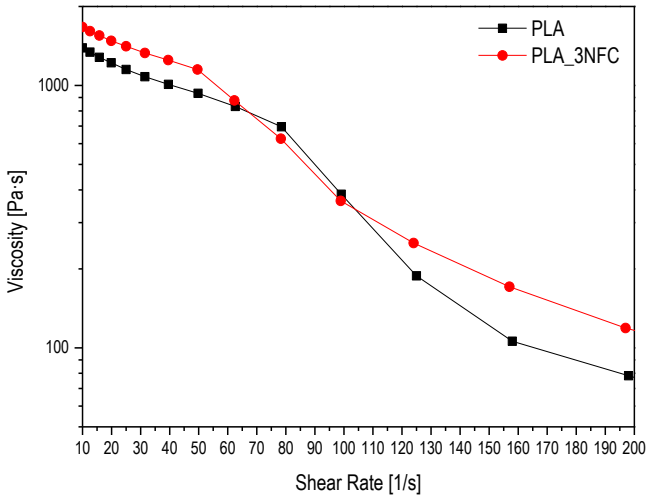

Figure 74. Apparent viscosity versur shear rate for neat PLA and PLA_3NFC filaments.

Thermogravimetric tests were carried out on filaments to investigate the thermal stability of the material with the introduction of nanocellulose. From the TGA thermograms reported in Figure 75, all the samples are characterized by a single degradation step that started approximately at 300°C. Nanocellulose had the positive to increase the thermal stability of PLA, as reported in previous studies [60, 175, 176], shifting the curves towards higher temperatures, in particular it was possible to observe an increase in the maximum loss rate temperature from 348°C of the neat PLA to 370°C of PLA with 3wt% of NFC.

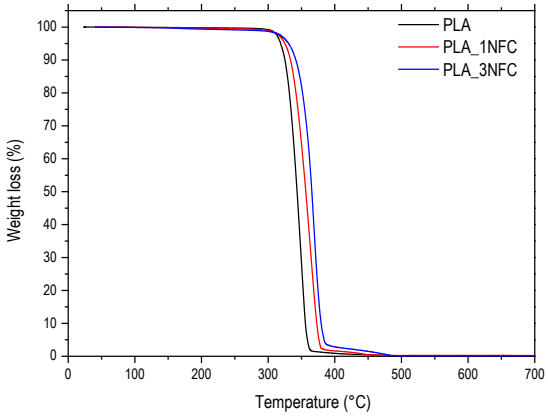

(a)

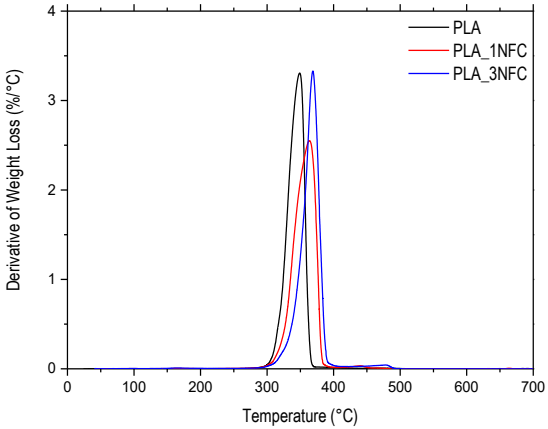

(b)

Figure 75. Thermogravimetric curves (a) and relative derivates (b) for filaments of neat PLA and PLA/NFC composite.

Glass transition temperature, crystallization temperature, melting temperature and degree of crystallinity were examined through differential scanning calorimetry for different samples of filaments. The obtained curves for the first heating, cooling and second heating are reported in Figure 76 while the results in Table 17. The reference enthalpy of fusion of 100% crystalline PLA was taken equal to 93.6 J/g [141]. Glass transition is a complex property which is related to several factors including intermolecular interactions, steric effects, the chain flexibility, the molecular weight, the branching and the cross-linking density. Glass transition temperature as expected was not affected by the presence of nanocellulose due to the low chemical interaction and similar results could be found in literature [177, 178]. With a Tg close to room temperature, physical aging occurred, and its relaxation peak can be seen as an endothermic peak just above the glass transition on the first heating DSC curve. The cold crystallization peak seems slightly shifted to lower temperatures with the addition of cellulose nanofibers as compared to neat PLA suggesting that NFC acted as nucleating agents for PLA [179]. Melting temperature of the PLA crystallites is identified at around 174°C for all the samples. From this fact, it is possible to state that nanocellulose is not affecting the crystalline structure of PLA in terms of size and perfection of the crystalline lamellae of PLA [180]. The degree of crystallinity is increasing with the concentration of NFC, from 1.4% for the neat PLA to 7.9% of PLA with 3wt% of NFC according with the first heating scan. In the second heat scan, it is still possible to notice the nucleating effect of NFC but with lower values. This confirms the previous observations related to the role of cellulose nanofibers as nucleating agents [178, 181].

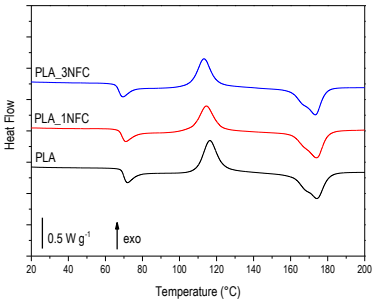

(a)

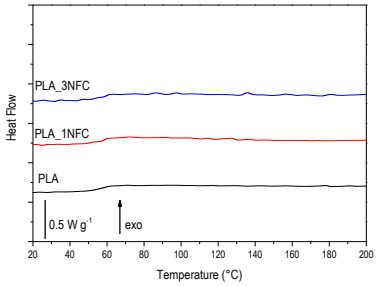

(b)

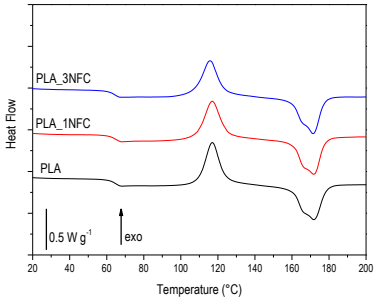

(c)

Figure 76. Differential scanning calorimetry curves of first heating (a), cooling (b) and second heating (c) cycle for neat PLA and PLA nanocomposite filaments.

Table 17. Glass transition temperature, crystallization temperature, melting temperature and crystallinity content for filament samples made of PLA and relative nanocomposite from DSC.

	1st heating				2nd heating			
	Tg (°C)	Tc (°C)	Tm (°C)	Xc (%)	Tg (°C)	Tc (°C)	Tm (°C)	Xc (%)
PLA	68.9	116.4	174.1	1.4	64.5	117.1	171.7	0.5
PLA_1NFC	68.7	114.6	174.1	2.8	64.3	116.9	171.7	0.6
PLA_3NFC	67.3	115.8	173.4	7.9	63.7	115.8	171.6	2.9

The water uptake tests allowed the determination of the moisture sorption behavior of neat PLA and nanocomposite filaments with various amounts of NFC, the relative curves of moisture absorption are shown in Figure 77. Water uptake curves showed a typical Fickian behavior for all formulations, with an initial part reporting a linear relationship between the humidity sorption and the square root of the time. Similar behavior is widely reported in literature on the hydro-thermal aging of polymer composites [182]. Time required to reach the equilibrium was 48 hours for all the samples despite the amount of NFC in the material. The moisture content after 10 days is slightly reduced by the presence of the nanofiller while the diffusion coefficient, calculated from the beginning of the experiment till the reaching of the stationary condition, is probably increased due to capillarity water diffusion and the flow of water vapor through micro-cracks, voids and other defects, including the filler-matrix interface [183].

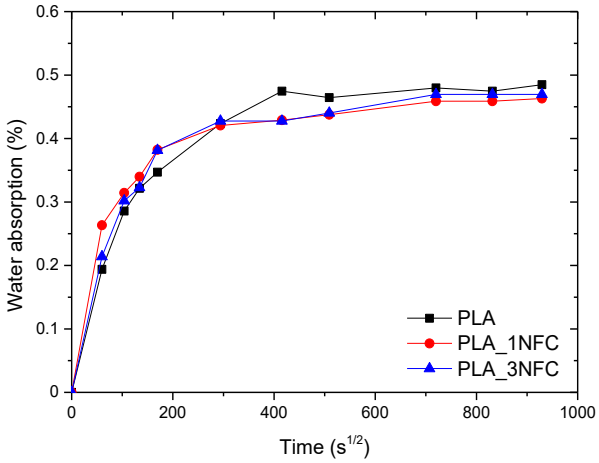

Figure 77. Water absorption against square root of time for PLA and PLA/NFC filaments at room temperature.

Table 18. Results resume from water absorption test on filaments of PLA and PLA/NFC.

	Time to equilibrium (h)	Max moisture sorption (%)	Diffusion coefficient (10^4*$s^{-1/2}$)
PLA	48	0.48	20 ± 3
PLA_1NFC	48	0.43	21 ± 4
PLA_3NFC	48	0.45	22 ± 3

In Figure 78, the isothermal creep compliance curves for 3D printed samples are shown. A reduction of the creep compliance with the increase of filler content confirmed an improvement of the dimensional stability. A decrease of the creep compliance at 3600 s of 8.5% for 3D printed samples could be observed after the introduction of 3wt% of NFC. The higher values of creep compliance for sample with 3 wt% of NFC are related with the higher porosity of the sample according to Table 21. The creep behavior of these materials was well fitted by a power law model as confirmed by an R-square higher than 0.999. In Table 19 are resumed the values of the fitting parameters. The weak compatibility between hydrophobic polymer matrix and hydrophilic nanofiller resulted in a decrease of the elastic instantaneous response of the material to the applied load (De). Reduction of the creep compliance is manly associated with the reduction of parameter k, that tunes the time-dependent response of the material, it resulted a decrease of 94% for a concentration of 3wt% of NFC. However, this drastically reduction is followed by an increase of the exponential parameter of the response that it mitigates the reduction in the total creep compliance.

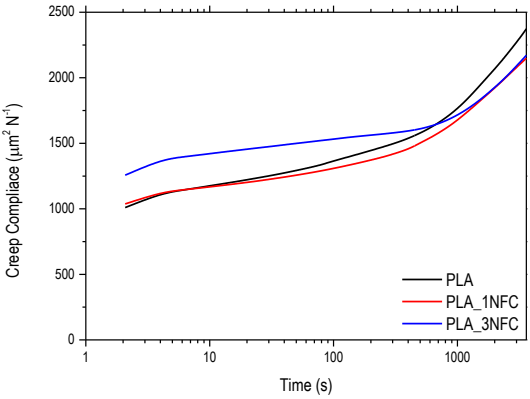

Figure 78. Creep compliance curves for 3D printed samples.

Table 19. Fitting values of the experimental data from creep compliance test.

	De ($\mu m^2/N$)	k ($\mu m^2/N$)	n
PLA	933 ± 13	135 ± 10	0.251 ± 0.009
PLA_1NFC	997 ± 4	92 ± 3	0.264 ± 0.004
PLA_3NFC	1278 ± 30	8 ± 2	0.563 ± 0.028

To study the effect of NFC on the elastic modulus, tensile strength and strain at break of neat PLA and relative nanocomposite, these properties are investigated for both filaments and 3D-printed samples. Results are summarized in Table 20 and Table 21, while the representative stress-strain curves are reported in Figure 79 and Figure 80 respectively.

Filaments displayed an increase in the elastic modulus with a maximum for 1wt% of NFC. An increase of 21.5% and 11% in the value of the elastic modulus was measured for 1wt% and 3wt% of NFC respectively. Ultimate mechanical properties slightly decreased due to the weak interaction between the matrix and the filler as confirmed by SEM analysis and the aggregation in micrometric bundles of cellulose.

Table 20. Mechanical properties of nanocomposite filaments with different contents of NFC.

	Elastic Modulus (MPa)	Stress at break (MPa)	Strain at break (mm/mm)
F_PLA	3224 ± 986	56.9 ± 4.0	0.048 ± 0.015
F_PLA_1NFC	3918 ± 1022	55.4 ± 1.3	0.044 ± 0.019
F_PLA_3NFC	3576 ± 914	52.8 ± 5.2	0.040 ± 0.006

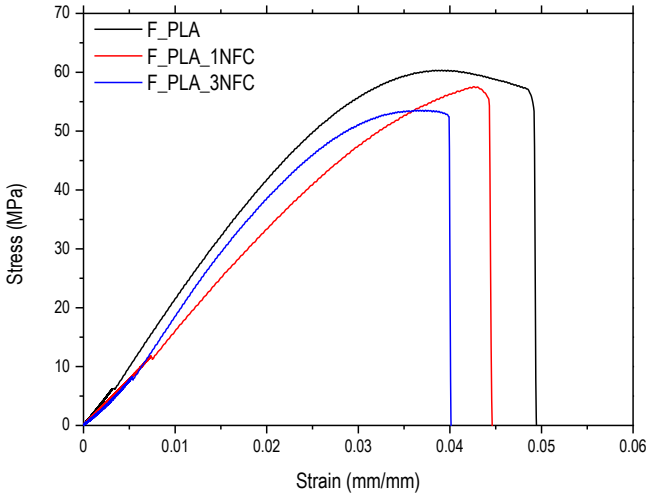

Figure 79. Representative stress- strain curves for filament samples.

The values of R-factor, an indicator of the quality of 3D printed specimen (Paragraph 3.4.3), decreased with the increase of nanocellulose content. This can be attributed to a growing difficulty of the printing process due to a possible increase of viscosity, as reported in similar studies [184, 185]. Stiffness of the material decreased with the increase of NFC content due to a poor adhesion of subsequent layers as highlighted by SEM observations. However, despite the decrease of R, it was possible to notice a slightly increase of the properties at break for the 3D printed samples with 1wt% of NFC. This effect could be attributed to the presence of different types of failure mechanisms at the interface between the polymer matrix and the nanofillers.

Table 21. Mechanical properties of 3D printed nanocomposite with different contents of NFC.

	R	E (MPa)	Stress at break (MPa)	Strain at break (mm/mm)
3D_PLA	0.73 ± 0.05	2505 ± 248	39.7 ± 4.9	0.042 ± 0.006
3D_PLA_1NFC	0.64 ± 0.12	2045 ± 6716	40.7 ± 3.1	0.045 ± 0.002
3D_PLA_3NFC	0.61 ± 0.11	1651 ± 424	29.8 ± 6.8	0.041 ± 0.005

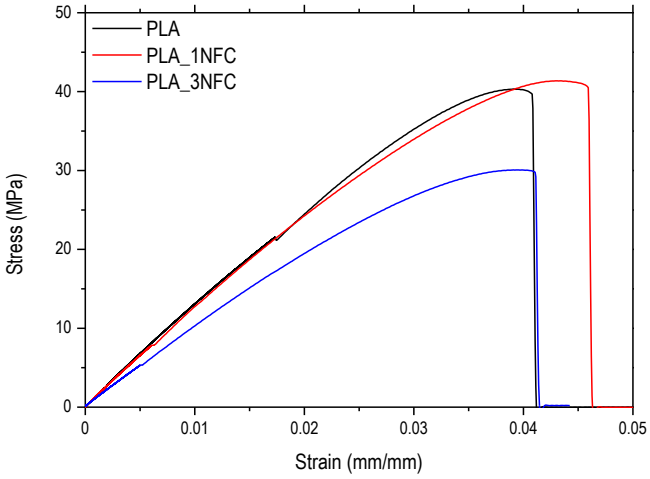

Figure 80. Representative stress- strain curves for 3D printed samples.

6.4. Conclusions

In this chapter, a biodegradable and renewable nanocomposite material based on PLA and fibrillated nanocellulose was studied to be used in Fused Deposition Modeling process. Micro cellulose was treated with high intensity ultrasounds to obtain cellulose in form of nanometric fibrils. PLA was mixed together with NFC in solution to reach a homogeneous dispersion. Filaments with different concentrations of NFC were produced with a single screw extruder and used to feed our desktop 3D printer.

The microstructure of 3D printed specimen was studied by SEM and the intra-layer adhesion is worsened by the presence of nano-fibrillated cellulose. Micrometric aggregates are detected inside the matrix with a poor adhesion to the matrix. Long fibers with a diameter around 100 nm are detectable at high magnification and appeared to randomly distribute with a good adhesion as suggested by a high degree of plastic deformation near the nanometric fibers. TGA highlighted a single step thermal degradation for PLA that was increased by the presence of NFC, an increase of 20°C in the thermal degradation maximum rate temperature was observed after loading with 3wt% of nanofibrillated cellulose. Differential scanning calorimetry highlighted the nucleating effect of nanocellulose measuring an increase of the crystallinity of around 3% at the highest concentration of nanocellulose. Water absorption test revealed that the moisture content was reduced by the presence of the nanofiller however the diffusion coefficient seemed to slightly increase probably due to capillarity water diffusion.

NFC reduced the time-dependent creep deformation of the 3D printed samples, and the creep compliance curves were well fitted by a power law model. Static tensile test displayed an increase in stiffness of the filament samples with increasing amount of nanocellulose. 3D printed samples evidenced a poor adhesion between subsequent layers according to SEM analysis and to decrease the apparent density as evaluated with the R-factor. Mechanical properties at break decreased for filament samples with the stress at break that went from 56.9 MPa for the neat polymer to 52.8 of 3D_PLA_3NFC.

Chapter VII

7. Polylactic acid - lauryl functionalized nanocellulose nanocomposites

Part of this chapter has been published in:

Rigotti, D.; Checchetto, R.; Tarter, S.; Caretti, Rizzuto, M.; D.; Fambri, L.; Pegoretti, A.

"Polylactic acid - lauryl functionalized nanocellulose nanocomposites: microstructural, thermo-mechanical and gas transport properties",

Express Polymer Letters

Checchetto, R.; Rigotti, D.; Pegoretti, A.; Miotello A.

"Chloroform desorption from poly(lactic acid) nanocomposites: a thermal desorption spectroscopy study",

Pure and Applied Chemistry

7.1. Introduction

Poly(lactic acid) (PLA) is one of the most interesting polymers in the field of bio-based, biodegradable plastic. In fact, due to its good mechanical properties, good workability, and excellent barrier properties it is a good candidate for the replacement of PS (polystyrene), PP (polypropylene), and ABS (acrylonitrile butadiene styrene) in several applications. However, PLA presents some weak points like low ductility, poor toughness, low glass transition temperature, high sensitivity to moisture, that limit its usage in some applications. The use of natural or synthetic fibers is well contemplated to obtain specific characteristics and major improvements of the final properties [12]. Natural fibers offer several advantages over synthetic fibers due to their "green" nature encompassing both renewability and biodegradability. This makes natural fibers good candidates as fillers in composite biopolymers. In particular, great attention was paid to the preparation of bio-composites made by PLA and different types of natural fibers such as flax [186-189], kenaf [190-192], jute [193-195], hemp [196], palm fibers [197]. However, some drawbacks should be solved for the further expansion of these bio-composite, such as limited mechanical durability, excess water absorption and poor thermal properties [198]. Natural fibers consist of repeated crystalline structure made by the aggregation of cellulose chains. The isolation of these ordered blocks of molecules led to a new group of micro and nano fibers with enhanced properties [130]. Nanocellulose fibers have attracted significant interest in the scientific community over the past 20 years due to outstanding mechanical properties [13, 14], high specific surface area and interesting optical characteristics [15]. Great attention is paid to the isolation of nanofibers from cellulosic material and different methods are known to obtain this type of fibers such as acid hydrolysis [132], mechanical treatment [60, 134, 199] and bacterial nanocellulose [200].

A large number of publications have been published on polylactides reinforced with nanocellulose. These composites are characterized by good mechanical strength and increased thermal and barrier properties. However, to extend their industrial applications, the compatibility between the hydrophilic surface of the cellulose and the hydrophobic polymer matrices need to be improved in order to enhance the dispersion and to increase the stress transfer towards the matrix. Different kinds of surface functionalization were adopted to improve the adhesion between the hydrophilic surface of the cellulose and the hydrophobic behavior of PLA to improve the adhesion properties. Salajkova et al. proposed an interesting and environmentally friendly procedure to obtain hydrophobic cellulose nanocrystals with the aid of quaternary ammonium salts, the treated nanocellulose was easily dispersed in non-polar solvent

[201]. Coastal plants were used as a source of nanocellulose by Fortunati et al., nanocellulose obtained from the acid hydrolysis of Poseidonia oceanica plant wastes was added to neat PLA with the aid of a surfactant. Mechanical properties were studied and was evidenced the plasticizing effect of the surfactant leading the possibility of tuning the mechanical properties of the obtained film with different amount of functionalized and non-functionalized nanocellulose [202]. As demonstrated by Lu et al., amine functionalization of nanocellulose via silanization of the hydroxyl groups on the cellulose surface is an efficient way to improve the dispersion of nanofiller within the polymer matrix and to increase the mechanical properties of the relative composites [147]. Ring opening polymerization of poly(l-lactide) was employed to functionalized cellulose nanocrystals by Lizundia et al., neat PLA and the obtained functionalized nanocrystals were melt-mixed and a good adhesion between filler and the matrix was demonstrated by the improvement in the strain at break respect to the neat PLA film [175]. The main application of bioplastic is in the packaging industry, where cheap biodegradable materials with barrier properties against the permeation of gas, moisture, small molecules are progressively requested. In 2017, 60% of the total bioplastic market was represented by packaging, underlining the importance of bioplastic in this sector [203]. The application of polymers in food packaging has focused the research on the transport of small molecules through the polymers. The characterization of the barrier characteristic of a polymer is a key feature to determine the product-package shelf-life. The specific barrier properties of the package system are related to the product characteristics and the intended end-use application [204]. Cellulose fibers had been found to increase the barrier properties of thermoplastic biopolymer films against water [205], water vapor [206], air and oxygen [207]. The incorporation of functionalized nanocellulose with long chain aliphatic molecules [208] or with surfactants [209] in casted PLA films had been proved to better decrease the water vapor permeability in respect of pristine nanocellulose, due to an enhanced dispersion in the polymer matrix.

In this chapter, nanocomposites based on PLA filled with hydrophobic-modified nanocellulose were prepared. Nanocellulose was functionalized by grafting hydrophobic lauryl chains via radical polymerization to improve the compatibility with the PLA. This functionalization improved the dispersion of nanocellulose in non-polar solvent. PLA-LNC nanocomposites were obtained through a solvent cast method. The thermo-mechanical properties of the casted films with different concentration of nanocellulose were evaluated and the barrier effect against different gases was investigated. This work represented a first effort into the development of 3D printable

nanocomposite material, but an efficient way to obtain large amount of chemically modified nanocellulose is a necessary step to move from lab to manufacturing scale.

7.2. Experimental

7.2.1. Preparation of nanocellulose

In a 250 ml flask containing 5 g of cotton wool (99% of cellulose), 150 ml of 40% sulfuric acid were added and the mixture was stirred for 1 hour at 50°C. The resulting solid was neutralized with a sodium carbonate solution and further washed with tetrahydrofuran and finally dried under vacuum.

7.2.2. Synthesis of lauryl functionalized nanocellulose

Accordingly, to Figure 81, in a 100 ml flask nanocellulose (1g) and lauryl chloride (11.5 ml) were suspended in toluene (15 ml) and pyridine (4.1 ml). The mixture was heated at 80°C for 5 hours and precipitated by the addition of ethanol (400 ml). The product was further washed with ethanol in order to completely eliminate the pyridine and the excess of lauryl chloride. The obtained LNC was dried under vacuum.

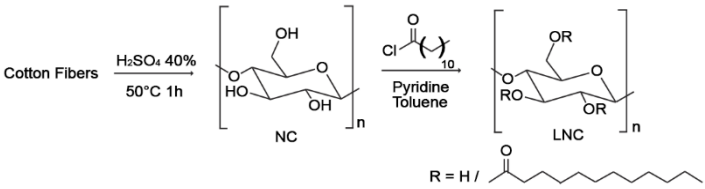

Figure 81. Synthesis of lauryl substituted nanocellulose (LNC)

7.2.3. Preparation of nanocomposite films

Biopolymer nanocomposites were prepared by solution mixing and casting. PLA was completely dissolved in chloroform (1 g PLA/ 25 ml $CHCl_3$) under magnetic stirring at 40°C. Functionalized nano-cellulose was dispersed in chloroform (0.1 g LNC/ 10 ml $CHCl_3$) using ultra-sonicator Hielscher 400S equipped with a sonotrode with 1 mm diameter at a power of 200 W for at least 10 minutes in an ice bath. PLA and LNC solutions were then mixed together with a magnetic stirrer for 3 hours to obtain solutions with different LNC filler content ranging from 0 to 20 wt%.. Bubbles were removed in an ultrasonic bath for 5 minutes. These solutions were then casted in a Petri dish and the solvent was let to evaporate first at room temperature for 24 hours and then for 4 hours in a ventilated oven at 40° C.

7.2.4. Sample designation

Nanocomposite films were designated indicating the type of matrix, the type of filler and its amount. For instance, a film of PLA filled with 5 wt% of lauryl functionalized nanocellulose is indicated as PLA_05LNC.

7.3. Results and discussion

7.3.1. Morphology analysis

TEM observations were done in order to investigate the morphology of the functionalized nanocellulose at nanometric scale. LNC appeared as elongated particles with a length around 500 nm and a width between 50 and 100 nm as shown in Figure 82a. Furthermore, electron diffraction pattern of LNC confirmed its crystalline structure after functionalization (Figure 82b).

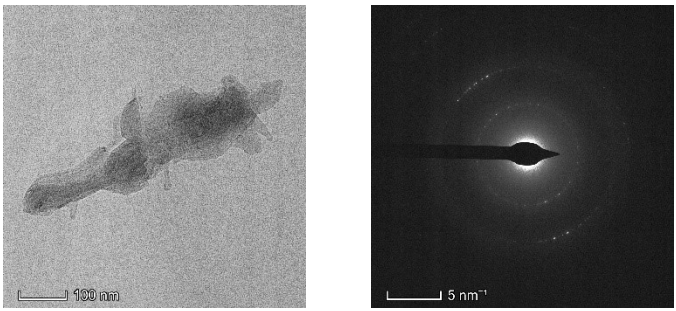

(a) (b)

Figure 82. TEM image of lauryl functionalized nanocellulose (a) and its relative diffraction pattern.

Morphological features of the cryo-fractured sections of neat PLA and lauryl functionalized nanocellulose composite films were investigated by FESEM and the images are shown in Figure 83. The fracture surface of the neat PLA sample (Figure 83a) shows a smooth and uniform surface without specific features. Increasing the amount of nanocellulose inside the matrix, the fracture surface changes from smooth to corrugated (Figure 83b-c). In fact, the fractured surface appears corrugated with cavities of non-uniform size and shape. Rounded aggregates start to form at a LNC content of 5wt% (Figure 83d). At 5wt% of LNC on the fracture surface it is possible to appreciate a significant amount of plastic deformation given by a homogenous distribution of the filler and a good combination of the alkyl chains on the interphase between the nanocellulose and the filler. As the LNC content increases, the precipitation process produces aggregates having an ovoidal shape and larger dimensions (see Figure 83e referring to nanocomposite samples with 10 wt% of LNC). Nanocellulose aggregates, in the 1 to 2 micrometer range, were hosted in cavities

with similar size. When the filler content increases, the size of the LNC aggregates also increases, as documented in Figure 83f that refers to the nanocomposites 20 wt% of LNC.

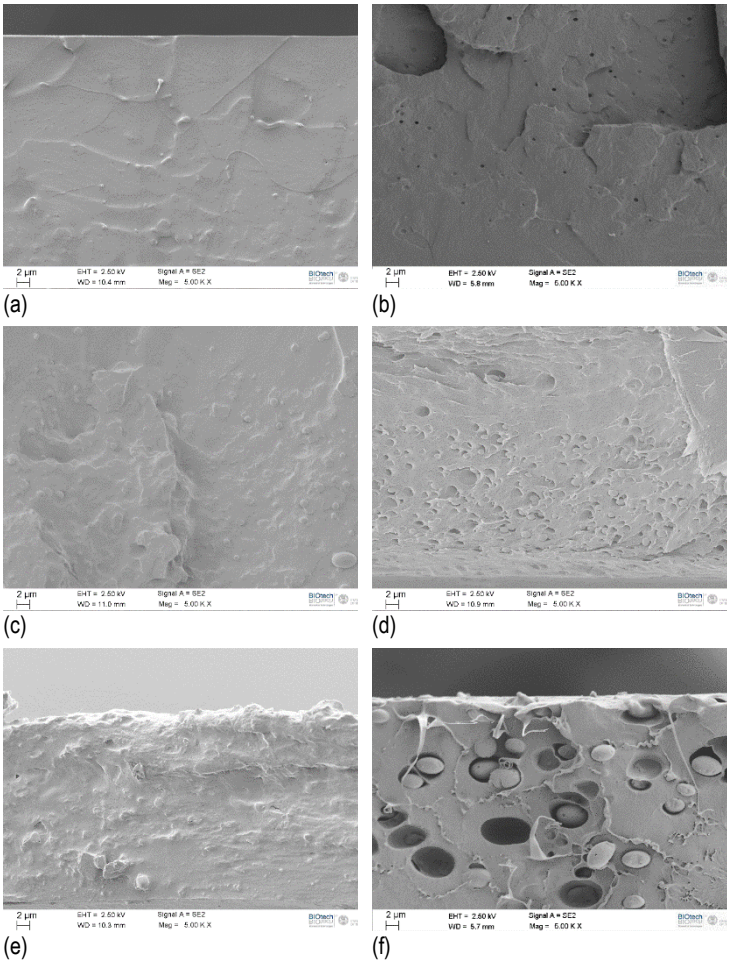

Figure 83. SEM images of the cryofractured surface of neat PLA (a), 1%LNC (b), 3%LNC (c), 5%LNC (d), 10%LNC (e) and 20%LNC (f).

7.3.2. Thermal properties

Resistance to thermal degradation of PLA nanocomposite films was evaluated through thermogravimetric analysis. Thermogravimetric curves and their relative derivative curves are shown in Figure 84. A first mass loss, centered at 100°C, can be identified for all the composition and it is related to the evaporation of the absorbed water and residual chloroform entrapped inside the material. Thermal Desorption Spectroscopy spectra on these film samples reveal that the release of residual $CHCl_3$ solvent molecules occurs when the PLA matrix is in its rubbery phase. The addition of filler particles introduces supplementary trapping sites where dispersed $CHCl_3$ molecules are hosted [210]. Neat PLA film degrade in a single step process starting at 270°C and the maximum degradation rate is located at 365°C. This degradation step is not affected by the presence of LNC.

Thermal properties of the neat PLA and PLA-LNC composites were determined using differential scanning calorimetry (DSC) and curves for second heating and cooling scans are reported in Figure 85. The glass transition temperature, the melting temperature and degree of crystallinity obtained from the DSC are reported in Table 22. The introduction of functionalized nanocellulose in the matrix slightly increases the glass transition temperature from 57.5°C of the neat PLA to 62.5°C for a filler concentration of 20wt%. The crystallinity fraction decreases as the nanocellulose content increases and the crystallization peak at 120°C for the neat PLA decreases when LNC is introduced in the matrix. Nanocellulose seems to only marginally influence the melting behavior of PLA: the melting peak slightly increases from 165.9°C for the neat PLA to 168.8 at 20wt% of LNC.

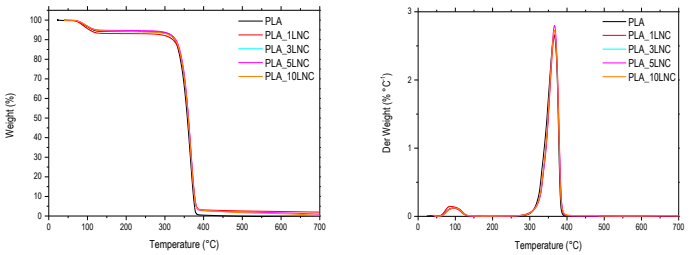

(a) (b)

Figure 84. Thermogravimetric curves (a) and their relative derivative curves (b) for neat PLA films and nanocomposite.

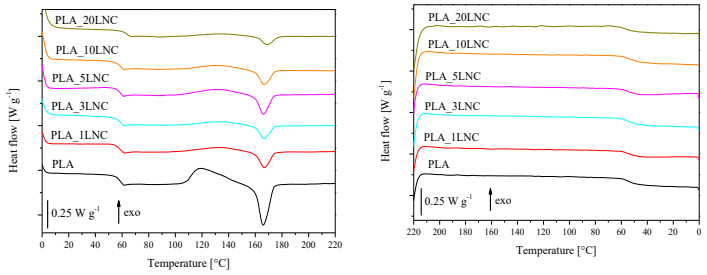

(a) (b)

Figure 85. DSC curves on second heating (a) and cooling (b) for neat PLA and nanocomposite films.

Table 22. Glass transition temperature (Tg), melting temperature (Tm) crystallization (ΔHc) and melting (ΔHm) enthalpy of PLA and PLA-LNC nanocomposites, as obtained from DSC curves of the second heating scan and crystallinity content (Xc).

	T_g (°C)	T_m (°C)	ΔH_c (J g^{-1})	ΔH_m (J g^{-1})	Tg c (°C)	X_c (%)
PLA	57	165.9	24.4	27.0	53	2.8
PLA_1LNC	58	166.7	7.5	10.4	54	3.1
PLA_3LNC	58	166.5	6.0	7.7	56	1.9
PLA_5LNC	58	166.1	10.2	11.5	55	1.5
PLA_10LNC	58	166.7	7.8	9.3	56	1.8
PLA_20LNC	62	168.8	11.9	12.4	56	0.7

7.3.3. Optical and chemical analysis

Transparency is a desirable feature for different kind of applications especially for packaging. The solution casting method used in this work allowed to obtain thin films with thickness of 50 μm. All composition resulted mostly transparent allowing seeing through the film, even those formulations with the highest amount of nanocellulose. These results were confirmed by the determination of the optical properties in the range 400–700 nm (Figure 86a). PLA with 1 wt% of LNC is the most transparent film with light transmission slightly higher than neat PLA due to the lower crystallinity according to the DSC. Light absorption increases with the nanofiller amount leading to a worsening of the transparency of the films. Light transmission in the UV range (250-400nm) is drastically reduced for all the composition and depends on the nanofiller amount [176].

The absorption A at a selected wavelength was determined on the basis of Lambert–Beer's law [211]:

$$A_{film} = \log(100/T) = \varepsilon_c * c * l \qquad \text{(Eq 8)}$$

where T is the experimental transmittance in percentage, ε_c is the absorption coefficient of the composites expressed in c^{-1} mm^{-1}, c is the solute concentration (in this case c = 1), and l is the optical path (film thickness).

In order to determine the specific absorbivity of LNC (E_{LNC}), the normalized Absorbance ($A_{PLA/LNC}$) of materials referred to 1 mm was calculated according to Eq 9 [212].

$$A_{PLA/LNC} = A_{film} \times 1000/d = A_{PLA} + E_{LNC} X_{LNC} IR \quad \text{(Eq. 9)}$$

where d is the film thickness expressed in micron, Afilm is the film absorption (from Eq. VII-1), APLA is the absorption of PLA, ELNC is absorbivity of LNC, X_{LNC} is the concentration of LNC expressed in percentage by wt%, IR is reference optical path (1 mm).

The values were calculated for two wavelengths in the visible spectra at 400 nm and 700 nm, as reported in Table 23, after evaluating the correspondent absorption of PLA, A_{PLA400} = 2.56 and A_{PLA700} = 1.21, respectively. The specific absorbivity E_{LNC} was determined directly for each single composition (except for 1% LNC) as reported in Table 23. The values E_{LNC} at 400 nm were found higher than those at 700 nm, indicating a better transparency in the red zone of the spectrum. The higher the crystallinity of the films, the higher the absorbivity coefficient, and the lower the transparency with an almost linear proportionality between adsorption and film crystallinity.

Moreover, due to the almost linear relationship between absorption and composition in the validity limit of Lambert-Beer law up to10 % of concentration, after linear fitting $E_{LNC\ 400}$ = 0.564 + 0.074 (R^2 = 0.94) and $E_{LNC\ 700}$ = 0.281 + 0.024 (R^2 = 0.97) were calculated.

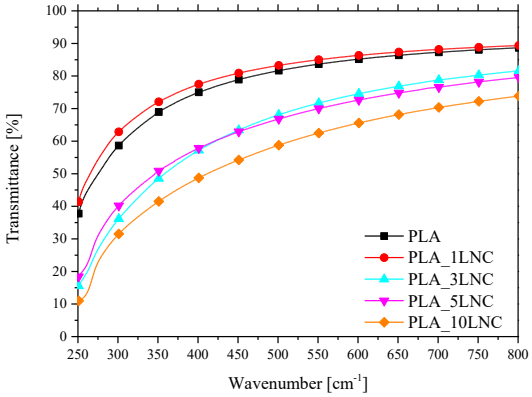

(a)

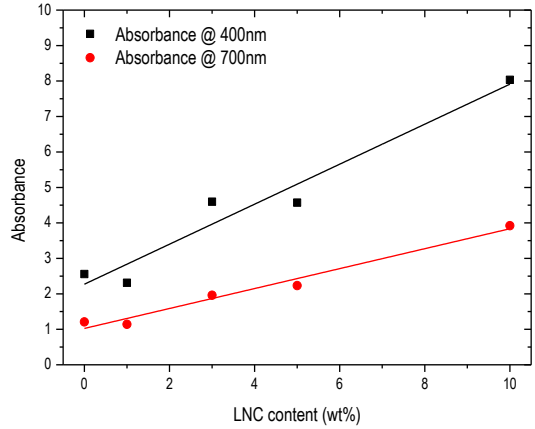

(b)

Figure 86. UV-vis spectra for neat PLA and nanocomposite films (a) and calculated absorbance of PLA-LNC composites as function of the composition (referred to 1 mm thickness) (b)

Table 23. Absorbance of film (Afilm) and specific absorbivity E_{LNC} (referred to 1 mm) of PLA-LNC nanocomposites determined at 400 nm and 700 nm.

.	Thickness L (micron)	$A_{film400}$ at 400 nm	$A_{film700}$ at 700 nm	E_{LNC} at 400 nm	E_{LNC} at 700 nm
PLA	49	0,125	0,059	//	//
PLA_1LNC	48	0,111	0,055	n.m.	n.m.
PLA_3LNC	53	0,244	0,104	0,68	0,25
PLA_5LNC	52	0,238	0,116	0,40	0,21
PLA_10LNC	39	0,313	0,153	0,55	0,28

n.m. not measurable

Chemical aspects related to the polymer–nanofiller interactions play an important role in the final properties of the composite materials. FTIR analysis of the PLA / LNC films was performed to study the relations between PLA and functionalized nanocellulose, the resulting FTIR spectra are reported in Figure 87a. The FTIR analysis shows an increase in the deep of the peak at 1750 cm^{-1} related to the stretching of the carbonyl group with the increasing amount of nanofiller due to the increasing amount of carbonyl groups attached to nanocellulose during the esterification with lauryl chloride [175, 213].

Peaks at 2996 and 2947 cm^{-1} associated with the antisymmetric and symmetric stretching vibrations of CH_3 of saturated hydrocarbons can be identified in the neat polymer identify, while for increasing amounts of LNC peaks at 2924 and 2855 cm^{-1} related to the stretching vibration of aliphatic carbon (-CH-) in the lauryl chain (Figure 87b) [214] can be recognized. The lack of any absorption peak near 3600 cm^{-1} indicated a good substitution of OH groups on the surface of cellulose.

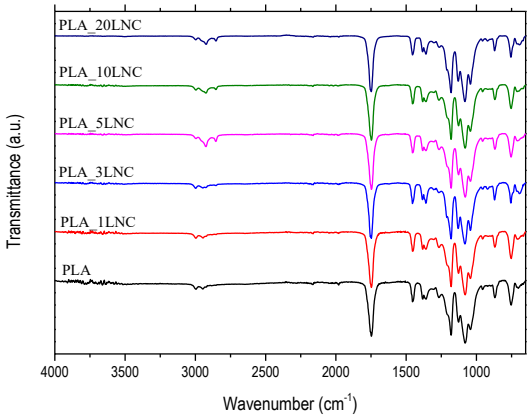

(a)

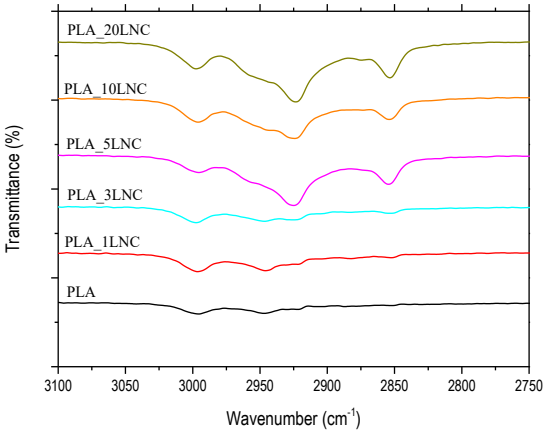

(b)

Figure 87. FT-IR spectra for neat PLA and PLA_LNC films (a), focus on the stretching aliphatic CH zone (b).

7.3.4. Mechanical properties

The effect of the incorporation of the functionalized nanocellulose on the dynamic-mechanical properties of PLA film are presented in Figure 89 and in Figure 89. A progressive decrease of the storage modulus (E') with an increasing amount of nanocellulose can be observed: in fact, E' at room temperature (25°C) decreases from 2405 MPa for the neat polymer to 1242 MPa for the 20wt% of LNC. This trend reverses at temperature above the glass transition temperature where the neat PLA displays the lowest value compared to composite. The increase of LNC content had only a marginal effect on the tan delta peak temperature. However, the peak value decreases with the introduction of the filler reducing the damping behavior, because the filler decreases the mobility of the rubbery phase. The minimum value of composite with 1% of LCN could be attributed to the relative higher crystallinity. Above Tg, storage modulus is nonlinear, due to a combined effect of LNC, as shown in Figure 89a. In particular at 70°C, all nanocomposites exhibited higher modulus than PLA matrix. The maximum value of PLA_1LNC is depending on a combined effect of the higher crystallinity (about 3 %) and the stiffening effect of LNC in PLA.

A progressive decrease in the storage modulus (E') with the increasing amount of nanocellulose is observed. This behavior is directly dependent on the functionalizing chains that could be interpreted according to Kelnar et al [215], as a kind of soft interface between nanocellulose and the glassy PLA matrix. E' at 25°C linearly decreases with a double slope tendency from 2405 MPa for the neat polymer to 1750 MPa and to 1242 MPa for the nanocomposite containing 5 and 20 wt. % of LNC, respectively. This trend reverses above the glass transition temperature where the neat PLA presents the lowest value of E' among the tested composites. The increase of LNC content has only a marginal effect on the $tan\,\delta$ peak temperature. Concurrently, the $\tan\,\delta$ peak value of PLA (0.29) decreases with the introduction of LNC which is reducing the damping behavior, because the filler decreases the mobility of the rubbery phase that is forming during the transition. The minimum value of damping peak (0.21) is shown in Figure 89b from the composite with 1% of LCN that could be attributed to the relative higher crystallinity (Table 22). On the other hand, the trend of storage modulus above Tg is not linear, due to a combined effect of PLA matrix and LNC filler. In particular at 70°C, all nanocomposites exhibited a higher modulus than PLA matrix (Figure 6a). The maximum value for PLA nanocomposite

with 1 wt. % LNC (190 MPa) is influenced by a combined effect of the higher crystallinity (about 3 %) and the stiffening effect of LNC in rubbery PLA. At higher filler content between 3 and 20%, the main role is played by LNC, and it determines a storage modulus in the range 80-100 MPa. Similar effects of the filler on PLA above Tg have been also documented by Spinella (63) and Suyanegara [216] for cellulose nanocrystals and microfibrillar cellulose, respectively.

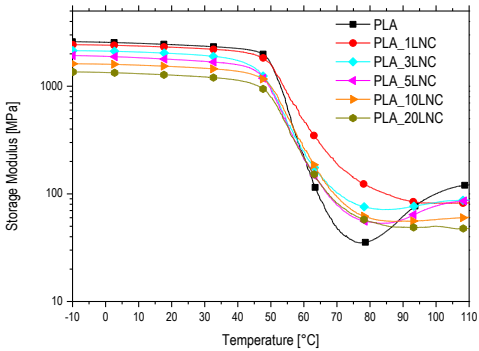

(a)

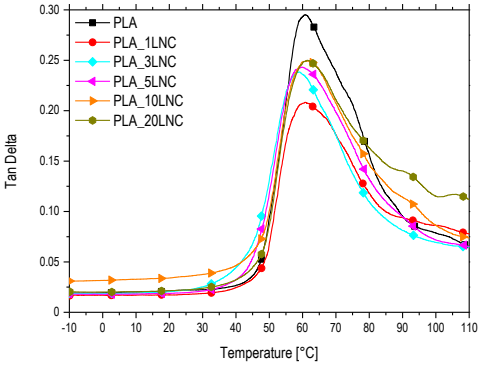

(b)

Figure 88. Storage modulus (a) and tan delta (b) curves for PLA and PLA-LNC blend films

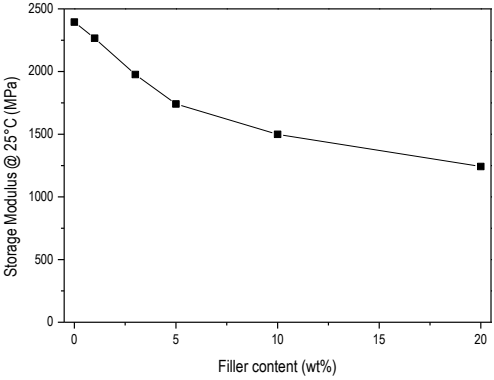

(c)

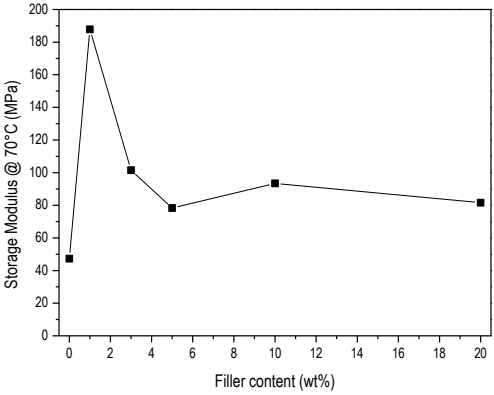

(d)

Figure 89. Effect of LCN filler on storage modulus at 25°C (c) and 70°C (d).

Uniaxial mechanical properties such as elastic modulus, ultimate tensile strength (UTS) and strain at break of PLA and nanocomposite films were evaluated trough tensile test and the results are summarized in Table 24, while the representative stress-strain curves are reported in Figure 90. The mechanical behavior of the obtained films was investigated using the DMA Q800 instrument in tensile configuration at room temperature to understand how the mechanical properties, specifically the elastic modulus (E),ultimate tensile stress (UTS), the strength (σ_B) and the strain at break (ε_B), are affected by the content of the LNC filler particles in the PLA matrix. At least three specimens for each sample were tested using a crosshead speed of 100 μm/min. This machine was used due to its high sensitivity to force and displacement.

Increasing the amount of lauryl functionalized nanocellulose inside the PLA matrix had the effect to decrease the stiffness of the tested films and it was in accordance with the DMA data regarding the decrease of the storage modulus (Figure 89a). This behavior could be related to the low stiffness of the short aliphatic chains attached to the surface of the cellulose. As shown in Figure 90, films with 3 and 5wt% of LNC exhibited the greatest strain at break, indicating a strong interfacial adhesion between the filler and the PLA matrix. This effect was confirmed also from SEM observation, in particular for the 5wt% of LNC as shown in Figure 83d, where it was possible to appreciate a large amount of plastic deformation on the fracture surface. For higher amount of nanocellulose, the presence of aggregates inside the matrix weakened the films leading to lower values of UTS and strain at break.

Table 24. Mechanical properties of nanocomposite films with different contents of LNC.

	Elastic Modulus (MPa)	UTS (MPa)	Strain at break (mm/mm)
PLA	1771 ± 98	38.8 ± 1.2	0.69 ± 0.19
PLA_1LNC	1740 ± 144	44.9 ± 2.5	0.26 ± 0.11
PLA_3LNC	1137 ± 96	25.5 ± 0.9	>1
PLA_5LNC	1065 ± 64	28.1 ± 3.6	>1
PLA_10LNC	1009 ± 62	20.7± 2.2	0.28 ± 0.14
PLA_20LNC	953 ± 26	18.3 ± 2.1	0.32 ± 0.10

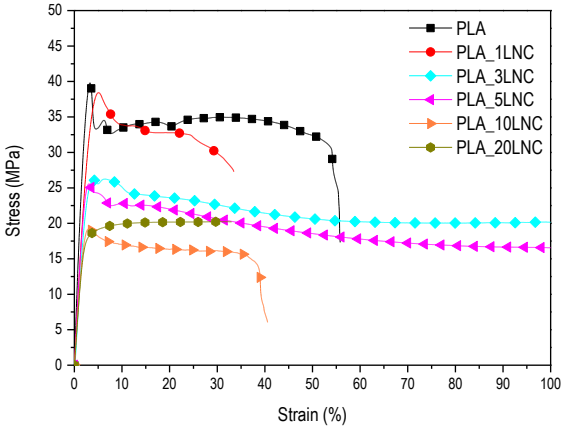

Figure 90. Representative stress – strain curves for PLA and PLA_LNC nanocomposite films.

Geometrical stability is worsened with the introduction of the nanofiller. In fact, creep compliance value measured at 3600 seconds rise from 0.9 GPa^{-1} of the film made of neat PLA to 2.56 GPa^{-1} of the sample with 20 wt% of LNC. It is likely that the addition of the short alkyl chains on the surface of nanocellulose enhanced the molecular mobility of the composite, thus decreasing the creep stability (Figure 91).

The results from the fitting of experimental creep data are reported in Table 25. The elevated R-square values indicate that the Findley equation reasonably represents the experimental data. The increase of the creep compliance due to the addition of functionalized nanocellulose is associated to a slight increase of the D_e value and a large intensification of the k coefficient, that tunes the time-dependent response to the applied stress. With the introduction of 1wt% of LNC, k increases by 5 orders of magnitude, from $4.1x10^{-7}$ to $5.7x10^{-2}$ GPa^{-1} s^{-n}.

Table 25. Results from creep compliance test and relative fitting values of the experimental data.

	D_{3600s} (GPa^{-1})	D_{el} (GPa^{-1})	Dve_{3600s} (GPa^{-1})	D_e (GPa^{-1})	k ($GPa^{-1}\,s^{-n}$)	n
PLA	0.900	0.671	0.229	0.705 ± 0.002	$4.1x10^{-7} \pm 4x10^{-8}$	1.60 ± 0.12
PLA_1LNC	1.271	0.574	0.697	0.484 ± 0.027	0.057 ± 0.013	0.32 ± 0.02
PLA_3LNC	2.441	0.860	1.580	0.654 ± 0.98	0.074 ± 0.039	0.38 ± 0.06
PLA_5LNC	2.564	1.206	1.357	0.995 ± 0.142	0.062 ± 0.057	0.38 ± 0.10
PLA_10LNC	2.431	1.053	1.378	0.811 ± 0.134	0.082 ± 0.059	0.35 ± 0.08
PLA_20LNC	2.560	1.736	0.823	1.601 ± 0.027	0.168 ± 0.019	0.21 ± 0.01

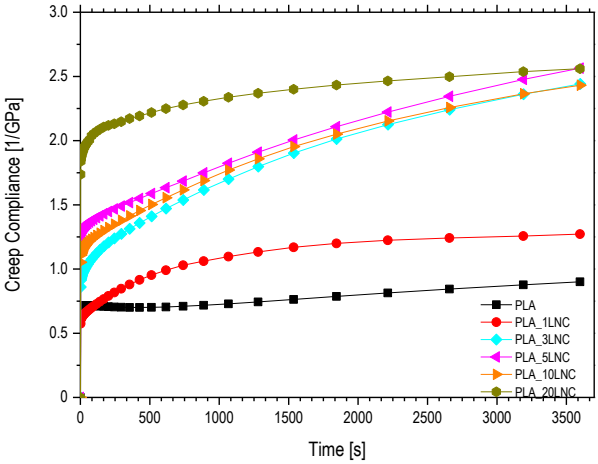

Figure 91. Representative creep curves for PLA and PLA_LNC films.

7.3.5. Gas barrier properties

Gas barrier properties were evaluated for film samples of PLA and nanocomposites 1, 3, 6.5, 8, 10, 12 and 15 wt % of LNC. Before gas transport tests, film samples were kept in high vacuum conditions inside the experimental apparatus for at least 12 hours [217]. Gas transport were tested against deuterium (D_2), nitrogen (N_2), and carbon dioxide (CO_2). Experiments were carried out at a constant temperature of 310 $\pm$ 1 K by gas phase permeation technique using planar film specimens shaped in form of thin disc with diameter d = 13.5 $\pm$ 0.1 mm and thickness of about 50 μm, which was measured before the transport test by using a micrometer caliper. For a more accurate description of the gas barrier evaluation procedure see Appendix 7.5.

The gas permeability as a function of the LNC filler content is reported in Figure 92. The gas permeability of the pure PLA matrix decreases adding LNC filler particles and reaches its minimum value at 6.5 wt. %: here gas permeability was a factor 3 about lower than that of the pure PLA membrane samples. For filler contents larger than 6.5 wt. %, the nanocomposite permeability increases and reaches values comparable to that of pure PLA matrix at filler concentration close to 15 wt. %. This trend is observed with all the investigated gases thus indicating that the addition of the LNC filler particles changes the gas transport properties in a non-selective way.

The observed variation of the gas permeability values in dependence on the filler content, are not accompanied by similar variation of the gas diffusivity D, as shown by Figure 92. These negligible variations of the penetrant diffusivity after the addition of the gas impermeable filler could be when the does not influence the chemical-physical properties of the polymer matrix: note, in fact, that DSC analysis indicated no relevant variation of the T_g and T_m values.

From Figure 92 and the SEM micrographs in Figure 83, it is possible to conclude that the variation of permeability values with filler addition are correlated with the LNC dispersion and aggregation process in the PLA matrix. In fact, the gas permeability reduces by the filler addition as long as LNC is dispersed or formed small clusters with size in the sub- micrometer range. On the other hand, the gas permeability increases when the addition of filler at LNC content larger than 6.5 wt. % due to LNC precipitation forming aggregates with size in the few micrometer range, in conformity to analogous literature interpretations [218].

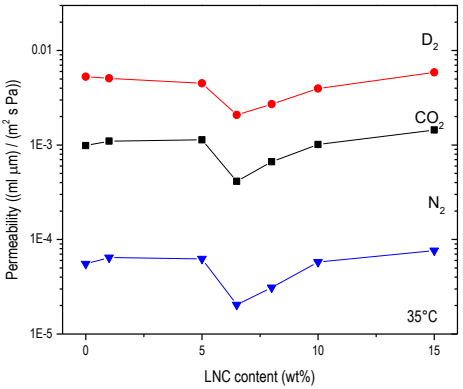

(a)

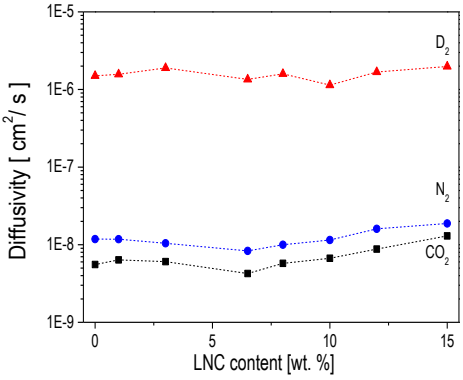

(b)

Figure 92. Permeability (a) and diffusivity (b) values at 35°C of the examined PLA-LNC nanocomposites as a function of the LNC filler content.

7.4. Conclusions

Biopolymer nanocomposites consisting of a poly (lactic acid) (PLA) matrix containing nano-cellulose filler particles (NC) functionalized by grafting hydrophobic lauryl chain (LNC) via esterification reaction were prepared. The mechanical and gas transport properties of biopolymer with different filler concentration were studied by Dynamical Mechanical Analysis (DMA) and gas phase permeation technique, respectively. Results were correlated to structural and physical information obtained by Scanning Electron Microscopy (SEM), Differential Scanning Calorimetry (DSC) and Fourier Transform Infra-Red spectroscopy (FTIR).

Microscopy observations highlighted that till 5 wt%, the functionalized nanocellulose was well dispersed in form of sub-micrometric cluster, for higher concentration the filler started to precipitate in micrometric aggregates. Nanocellulose particles, as well as their aggregation, did not chemically interact with the polymer matrix of PLA as resulted from FTIR and TGA analysis, also the glass transition temperature and the crystalline fraction remained untouched as confirmed by DSC analysis. The storage modulus E' and the stiffness of the nanocomposites decreased when tested at room temperature with the increasing of LNC fraction due to the introduction of short alkyl chains in the matrix. Lauryl groups caused the increase of the creep compliance values and in particular of the time-dependent response of the material to constant loads. Nanocomposites with 3 wt% and 5 wt% showed the greatest strain at break and the largest amount of plastic deformation on the fractured cross-section surface suggesting strong interfacial adhesion between the PLA and filler particles when dispersed in the polymer matrix. For larger amount of nanocellulose, the presence of the LNC aggregates weakened the nanocomposite leading to lower values of maximum stress (UTS) and strain at break.

The gas barrier properties of the PLA matrix for D_2, CO_2 and N_2 improved increasing the concentration of LNC up to a critical concentration of 6.5 wt% where the gas permeability of the nanocomposite was 70 % lower than that of the PLA matrix. For higher amount of nanocellulose, micrometer- sized LNC aggregates started to form in the PLA matrix and the gas permeability of the nanocomposite increased. The present biopolymer nanocomposites evidenced great potential for application in packaging technology when the preparation procedure ensured a high dispersion degree of the filler particles.

7.5. Appendix: Gas transport properties evaluation

Gas transport properties were studied by the following procedure [217, 219]. At time $t = 0$, one side of the film, called High Pressure Side (*HPS*), was exposed to the test gas kept at a fixed pressure $P_{HPS} = 40$ kPa, while the other side, called low pressure side (*LPS*), was kept in high vacuum conditions. The gas permeation process consists of the transfer of gas molecules from the *HPS* through the film layer. Gas molecules permeate through the film of surface area $A = \frac{1}{4}\pi d^2$ at a rate $Q(t) = A\, j_{exp}(t)$ where $j_{exp}(t)$ is the permeation flux. In the analysis chamber the permeated molecules form a rarefied gas in thermal equilibrium with the chamber walls at temperature T_{cham}. The partial pressure $P_{LPS}^{gas}(t)$ of the test gas varies, as a function of time t, according to the following relation [220]:

$$Q(t) = \frac{1}{R\,T_{cham}}\left[V\frac{dP_{LPS}^{gas}(t)}{dt} + S_p P_{LPS}^{gas}(t)\right] \quad \text{(Eq 10)}$$

where R is the universal gas constant, V is the volume of the analysis chamber and S_p the pumping speed of the vacuum system. In the present experimental approach, the permeation test is carried out under continuous pumping of the analysis chamber and with the condition $\frac{S_p}{V} \gg \frac{1}{P_{LPS}}\frac{dP_{LPS}(t)}{dt}$. Consequently, the permeation flux $j_{exp}(t)$ is directly proportional to the instantaneous value of the partial pressure of the probe gas

$$Q(t) = A\, j_{exp}(t) = S_p P_{LPS}^{gas}(t) \quad \text{(Eq 11)}$$

During the permeation experiments $P_{LPS}^{gas}(t)$ is measured, as a function of time, by a quadrupole mass spectrometer (QMS, QMG 420 Balzers) equipped with Secondary Electron Multiplier and grid- type ion source. The obtained $P_{LPS}^{gas}(t)$ data were converted into permeation flux curves $j_{exp}(t)$ through the relation:

$$j_{exp}(t) = \frac{1}{A}\,\frac{1}{R\,T_{cham}}\,S_p P_{LPS}^{gas}(t) \qquad \text{(Eq 12)}$$

Edge effects, in the present work, can be neglected because the dimensions of the specimen film are much greater than the thickness, so the transport process can be analysed assuming a one-dimensional geometry of the membrane.

Gas transport through polymer membranes is controlled by three steps, according to the solution-diffusion models [221]:

- The absorption of penetrant molecules in the surface layers of the High-Pressure Side (HPS) of the membrane. Gas concentration here immediately reaches the equilibrium value c_{HPS} which is given by the Henry law: $c_{HPS} = c(x = 0, t) = \Pi\, P_{HPS}$, where $x = 0$ represents the coordinate of the HPS of the membrane along the flux direction and Π is the equilibrium gas solubility in the membrane layers.
- The diffusion of the absorbed molecules from the *HPS* (at $x = 0$) to the *LPS* (at $x = L$) with a concentration gradient. According to the first Fick law the gas flux $j(x,t)$ is given by the relation $j(x,t) = -D\,\frac{\partial c(x,t)}{\partial x}$, where $c(x,t)$ is the gas concentration at time t in the membrane layers at depth x below the HPS and D is the gas diffusivity in the membrane layers.
- The desorption of the molecules from the *LPS* surface layers. The gas concentration in the LPS side of the membrane, c_{LPS}, is also given by the Henry law: $c_{LPS} = c(x = L, t) = \Pi\, P_{LPS}^{gas}$.

The $c(x,t)$ quantity is obtained solving the Fick's second equation $\frac{\partial c(x,t)}{\partial t} = D\,\frac{\partial^2 c(x,t)}{\partial x^2}$ with the previous boundary conditions in $x = 0$ and $x = L$ and permits to calculate the gas permeation flux $j(t)$ by the relation $j(t) = j(x = L, t) = -D\,\frac{\partial c(x=L,t)}{\partial x}$. This diffusion problem admits for $j(t)$ the following analytical solution [222]: $j(t) = \frac{D\,\Pi}{L}(P_{HPS} - P_{LPS})\left[1 + 2\sum_{n=1}^{\infty}(-1)^n\, exp\,\frac{-D\,n^2\,\pi^2\,t}{L^2}\right]$.

Because $P_{LPS}^{gas} \ll P_{HPS}$ then the following approximation holds:

$$j(t) = \frac{D\,\Pi}{L} P_{HPS} \left[1 + 2\sum_{n=1}^{\infty}(-1)^n \, exp\, \frac{-D\,n^2\,\pi^2\,t}{L^2}\right] \qquad \text{(Eq 13)}$$

The permeation process (Eq 12) is characterized, after an initial transient condition, by a stationary transport conditions where the permeation flux $j(t)$ assumes the constant value: $j(t \to \infty) = J = \frac{D\,\Pi}{L}\, P_{HPS} = \frac{\emptyset}{L}\, P_{HPS}$, where $\emptyset = D\,\Pi$ is called the gas permeability.

Equation 13 is used to fit the experimental $j_{exp}(t)$ curves and obtain the $\emptyset$ and D gas transport parameters. In Figures 10(a), 10(b) and 10(c) the $j_{exp}(t)$ curves obtained with the D_2, N_2 and CO_2 test gas, are respectively presented.

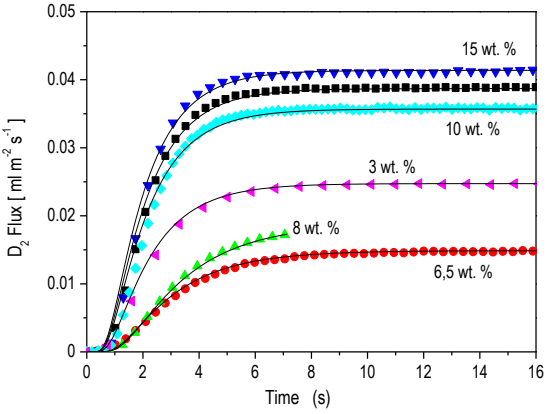

(a)

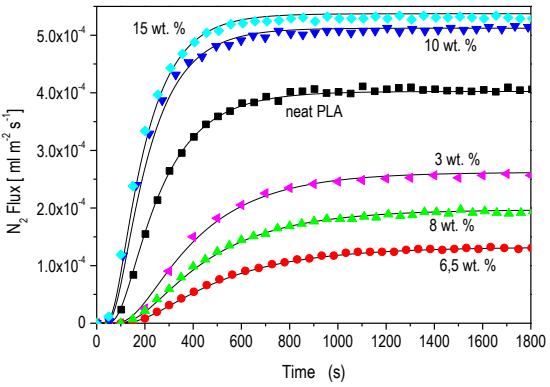

(b)

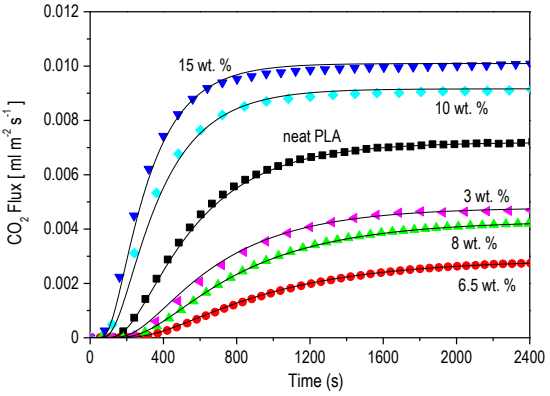

(c)

Figure 93. Permeation curves through film of PLA and LNC nanocomposites at T = 310 ± 2 K and P_{HPS} = 40 kPa for D_2 (a), N_2 (b) and CO_2 (c). Lines fits of data according to Eq 13.

From permeation curves in Figure 93 of the three test gases it is possible to observe that:

- the gas transport process in the pure PLA sample as well as in all nanocomposites reaches stationary transport conditions in much shorter interval times using D_2 (about 4-5 s) than CO_2 and N_2 (≈about 500-700 s), as direct dependence on the molecule size;
- CO_2 and N_2 present comparable duration of the transient regime, but different transport rates in stationary transport condition;
- with all gases the permeation flux J in stationary transport conditions varies with the filler content with same trend. In fact, J decreases increasing the filler content up to 6.5 wt. % and then monotonically increases at higher filler content. The $j_{exp}(t)$ curves do not show major variations of the lasting of the transient transport conditions changing the filler content.

The values of the D and $\emptyset$ gas transport parameters were obtained fitting of the experimental $j_{exp}(t)$ curves by Eq. VII-6, see continuous lines in Figure 93. Results are presented, as a function of the LNC filler content, in Figure 93a and Figure 93b for gas permeability and diffusivity, respectively.

According to literature models describing the gas transport properties of Mixed Matrix Membranes (MMM), the gas transport properties of a polymer matrix are influenced by the addition of gas impermeable fillers that gives rise to variations of the physical-chemical properties of the polymer layers at the filler-matrix interface, these changes produce variations of the interface permeability values [218, 223-228]. When chemical-physical variations of the polymer layers at the matrix-filler occur then the gas permeability of a l_{int} thick interface regions around the filler particles is significantly altered. Polymer chains here can be rigidified in comparison with the bulk polymer chains as consequence of the polymer-particle interfacial adhesion [225-228].

In this rigidified region the permeability $\emptyset_{int}$ is reduced with respect to that of the continuous polymeric phase $\emptyset_{PLA}$ by a quantity β called "chain immobilization factor": $\emptyset_{int} = \emptyset_{PLA}/\beta$. The filler may, on the contrary, increase the gas permeability of the filler-matrix interface layers $\emptyset_{int}$ because its presence disrupts the polymer chain packing and increase the free volume or because poor polymer-filler adhesion causes the formation of interface nano-cavities [225-228]. Literature models quantitatively

describe the effects of the modified interface layers on the gas permeability of the pure matrix modelling the dispersed filler particles with $\emptyset_{\mathrm{d}}$ permeability and the surrounding modified polymer layer with $\emptyset_{\mathrm{int}}$ permeability as a dispersed "pseudo-phase" with effective permeability:

$$\emptyset_{\mathrm{eff}} = \emptyset_{\mathrm{int}} \frac{\emptyset_{\mathrm{d}}+2\emptyset_{\mathrm{int}}-2\varphi_{\mathrm{s}}(\emptyset_{\mathrm{int}}-\emptyset_{\mathrm{d}})}{\emptyset_{\mathrm{d}}+2\emptyset_{\mathrm{int}}+\varphi_{\mathrm{s}}(\emptyset_{\mathrm{int}}-\emptyset_{\mathrm{d}})} \qquad \text{(Eq 14)}$$

where φ_{s} is the volume fraction of the filler in the "pseudo-phase" that depends both on the thickness of the interface layer as well as on the geometry of the filler particle. When the filler particles can be described as long cylinders with length much longer than their diameter $2r_d$ then:

$$\varphi_{\mathrm{s}} = \frac{{r_d}^2}{(r_d+l_{int})^2} \qquad \text{(Eq 15)}$$

And the effective permeability of the nanocomposite film $\emptyset_{\mathrm{NC}}$ can be the calculated by the relation:

$$\emptyset_{\mathrm{NC}}=\emptyset_{\mathrm{PLA}} \frac{\emptyset_{\mathrm{eff}}+2\emptyset_{\mathrm{M}}-2\,\varphi_{\mathrm{pp}}(\emptyset_{\mathrm{M}}-\emptyset_{\mathrm{eff}})}{\emptyset_{\mathrm{eff}}+2\emptyset_{\mathrm{M}}+\,\varphi_{\mathrm{pp}}(\emptyset_{\mathrm{M}}-\emptyset_{\mathrm{eff}})} \qquad \text{(Eq 16)}$$

where φ_{pp} is the volume fraction of the dispersed "pseudo-phase" in the nanocomposite.

Experimental permeability data for filler content lower than 6.5 wt. % can be reproduced assuming that in these nanocomposites polymer stiffening occurs, Figure 94a shows the calculated $\emptyset_{\mathrm{NC}}/\emptyset_{\mathrm{PLA}}$ values (solid symbols) and obtained lines from the experimental permeability data as a function of the vol. % filler content, c_{LNC}. It is possible to conclude that for filler content lower than 6.5 wt. % the observed permeability reduction is due to the formation of a strongly rigidified interface region with thickness $l_{int} = 8 \div 10$ nm around filler particles. This rigidifying effect could be attributed to the presence of the lauryl chains functional groups at the filler surface, the compatibility between the PLA matrix and the lauryl chains reduces the free volume in the 10 nm thick interface region. Note that mechanical analysis evidence that nanocomposites with 3 and 5 wt. % of LNC exhibited the greatest strain at break, indicating a strong interfacial adhesion between the filler and the PLA matrix also

confirmed by SEM observation which evidence a large amount of plastic deformation on the fractured cross-section surface.

Gas permeability starts to increase when the filler content is higher than 6.5 wt. % and at this concentration, structural analyses evidence that in these samples there is the formation of spherical aggregates with size in the few micrometer range. The permeability increase in these samples can be attributed to the formation of regions around these spherical aggregates with permeability values higher than those of the PLA matrix.

In Figure 94b, the filler content is expressed as the LNC excess with respect to the PLA_6.5LNC reference sample which implicitly assumes that all excess filler content forms the observed aggregates. Dashed lines are data fitting of the $\Phi_{NC}/\Phi_{NC}^{PLA+6.5\ wt.\%}$ obtained assuming that the excess LNC filler particles form spherical dispersed "pseudo-phase", that consists of the filler aggregate and the surrounding spherical shell with l_{int} thickness. Experimental $\Phi_{NC}/\Phi_{NC}^{PLA+6.5\ wt.\%}$ data can reproduced assuming, for each test gas, interface shell thickness with size comparable with that of the LNC aggregates, see l_{int} values in Figure 94b and interface permeability values ~ 100 Φ_{PLA}.

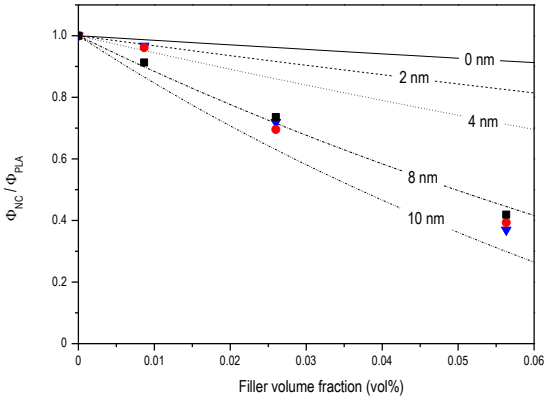

(a)

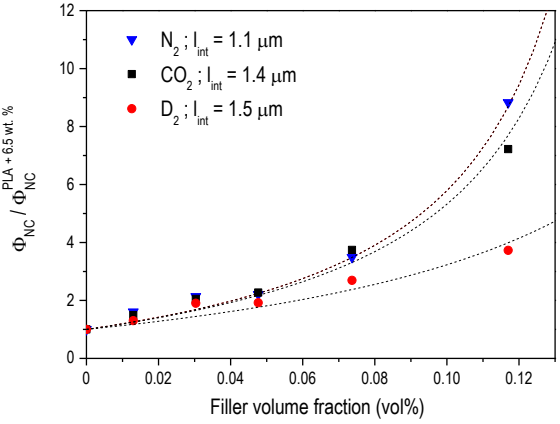

(b)

Figure 94. $\emptyset_{NC}/\emptyset_{PLA}$ values of LNC nanocomposite samples as a function of the LNC volume content up to 6.5 wt %, lines are obtained using Eqs and Eq 13 with $\beta = 5$ for different l_{int} values between 0 and 10 nm (a). $\Phi_{NC}/\Phi_{NC}^{PLA+6.5\ wt.\%}$ values for filler content from 6.5 to 15 wt. %. The filler content is expressed in volumetric units, as excess with respect to the filler content of the PLA + 6.5 wt. % reference sample. Lines are obtained using Eq 16 assuming interface shell thickness ~ 1 μm and effective interface gas permeability ~ 100 Φ_{PLA} (b).

Chapter VIII

8. Polyhydroxyalkanoates/nanocellulose composites for additive manufacturing

Part of this chapter has been published in:

Valentini, F.; Rigotti, D.; Dorigato, A.; Pegoretti, A.,

"Polyhydroxyalkanoates/nanocellulose composites for additive manufacturing",

Journal of Polymers and the Environment.

8.1. Introduction

The feasibility of processing a biopolymer both biodegradable and from renewable resources through additive manufacturing technologies is the key point of this chapter. A rising interest on the possibility of 3D printing with polyhydroxyalkanoates (PHA) is emerging from industry due to the green features of these materials.

According to European Bioplastics Association bioplastics are used in an increasing number of applications, from packaging to agriculture, from consumer to electronics, from textile to automotive sectors. This growth is driven by the demand of new applications and innovative products. In fact, these biopolymers offer a number of additional advantages if compared to conventional plastics, such as no need to use fossil fuel derived chemicals, a reduced carbon footprint and additional waste management options [52]. Important bio-based polymers, such as PLA and starch blends that represented the 29% of the global production of bioplastics in 2017 according to European Bioplastic [229], are derived from biological materials and from edible biomasses. Nevertheless, biopolymer synthesis can enter in direct competition with the food production, and bioplastics industry is therefore looking for alternatives sources starting from non-edible biomass and biological systems [230].

Poly-hydroxy-alkanoates (PHA) are a huge family of thermoplastics biopolymers totally synthesized by microorganism as an intracellular storage product under particular growth conditions such as abundant carbon source, limited sources of oxygen, phosphorous or nitrogen. The carbon is assimilated and processed into hydroxyalkanoate units, polymerized and stored in the cell cytoplasm. The product of the process is a high molecular weight crystalline polyester that is maintained in an amorphous state in vivo [231]. PHA most promising application is in packaging field and in agricultural applications. It can be used to produce water resistant films, foils and coatings in alternative to aluminum, in medicine application for cardiovascular devices, in tissue engineering as bioresorbable scaffold [232]. Despite these good features, PHA is highly challenging to be processed due to secondary crystallization that led embrittlement [233] and a very sharp processing temperature window due to thermal degradation [234, 235]. Among the different processes, poor attention has been dedicated to additive manufacturing (AM) technologies using PHA based composites.

On the basis of these consideration, the aim of this part of the work was not only to prove that it is possible to use this kind of material in FDM, but also to develop nanocomposite materials able to maintain the characteristics of renewability and biodegradability. Filaments based on poly(3-hydroxybutyrate-co-3-hydroxyhexanoate) and fibrillated nanocellulose (NFC) were successfully printed until 3wt% of NFC. Development of these blends and the characterization of the most important physical and mechanical properties of PHBH and its relative nanocomposites produced through FDM process were discussed in this chapter.

8.2. Experimental

8.2.1. Filament preparation

Masterbatch material for the subsequent extrusion was obtained through solution mixing. Freeze dried NFC was dispersed in chloroform (0.1g NFC / 10ml $CHCl_3$) and ultrasonicated with a Hielscher UP400S Ultrasonicator (Teltow, Germany) for 5 minutes at 400W in an ice bath to prevent overheating. PHBH X151A was dissolved in chloroform (1g PHBH / 25ml $CHCl_3$) and mechanically stirred at 45°C until complete dissolution was reached. At the end, the two solutions were mixed together at 45°C for 3 hours. After a mild sonication in an ultrasonication bath to remove the air bubbles, the solution was poured in a petri dish and it remained at room temperature for 12 hours and in a ventilated oven at 50°C for 3 hours to permit the evaporation of the solvent. The obtained material, with a concentration of 3wt% of NFC, was grinded with and without neat PHBH to prepare a coarse powder with a final composition of 0.5wt%, 1wt% and 3wt% of NFC. These powders were used to feed a single screw extruder provided by Friul Filiere (Buoja, Italy) and filaments of neat PHBH and different concentration of NFC were extruded. The temperature profile of the extruder went from 100°C in the feed zone to 125°C just before the nozzle where it was raised to 150°C.

8.2.2. 3D printing by FDM

A desktop 3D printer provided by Sharebot (Italy), based on Fused Deposition Modeling, was used to print dumbbell specimens with filaments of PHBH X151A with increasing amount of NFC. A careful monitoring of the temperatures was required to avoid warping phenomena and the detachment of the printed object from the building plate due to thermal stresses related with the crystallization of the material after the

extrusion from the nozzle of the 3D printer. The bed plate was set at 75°C and covered with double-sided tape to increase the adhesion. The temperature of the nozzle was adjusted at 200°C to print the first layer of the specimen and then was decreased to 180°C in the last layer to provide a gradient of temperature inside the object that limited the warping phenomena.

8.2.3. Sample designation

All nanocomposites were designated indicating the type of sample (filament or 3D print), the matrix, the type of filler and its amount. The adopted codes are summarized in the following table.

Table 26. Sample designation.

Sample name	Type	Filler weight percent wt. %
F_PHBH	Filament	0
F_PHBH_0.5NFC	Filament	0.5
F_PHBH_01NFC	Filament	1
F_PHBH_03NFC	Filament	3
3D_PHBH	3D print	0
3D_PHBH_0.5NFC	3D print	0.5
3D_PHBH_01NFC	3D print	1
3D_PHBH_03NFC	3D print	3

8.3. Poly(3-hydroxybutyrate-co-3-hydroxyhexanoate) X131A – X151A

Kaneka provided two grades of poly(3-hydroxybutyrate-co-3-hydroxyhexanoate (PHBH): X151A and X131A. In this chapter, the preliminary evaluation on these two polymers is presented.

The extrusion temperature profile was finely adjusted to compensate the higher melt viscosity of X131A with respect to X151A. The temperature of the head and the one of the die were raised by 10 °C.

Table 27. Temperature profile of the extruder during the production of PHBH filaments.

	T1 (°C)	T2 (°C)	T3 (°C)	T4 (°C)
X151A	100	105	125	150
X131A	100	105	135	160

During the 3D printing process of X131A, the temperatures were lowered by 10°C with respect to X151A to overcome the different rate of crystallization between the two materials. Temperature of the building bed was left at 75°C, just over the cold crystallization temperature to limit the thermal stresses in the material.

Table 28. Temperatures used in 3D printing of the two polymers.

	T1 (°C)	T2 (°C)	T bed (°C)
X151A	200	180	75
X131A	190	170	75

Solid State NMR was carried out to obtain chemical information about the composition of the two copolymers. From the spectra, reported in Figure 95, it was possible to recognize the signal referred to the presence of PHB and PHH. In the spectrum of X131A, the peaks caused by PHH had lower intensity than in the spectrum of X151A. The main peaks were assigned in Table 29 and the results in terms of composition were summarized in Table 30.

Table 29. Peak table for PHBH X131A and X151 according to NMR.

Chemical Shift (ppm)	Signal	PHB	PHH
170.0	C=O	X	X
68.9	O-C-H	X	X
43.3	CH2	X	
34.9	CH		X
21.7	CH3	X	
15.0	CH3		X

Table 30. Composition for PHBH X131A and X151 according to NMR.

	PHB (wt%)	PHH (wt%)
X131A	95 ± 2	5 ± 2
X151A	90 ± 2	10 ± 2

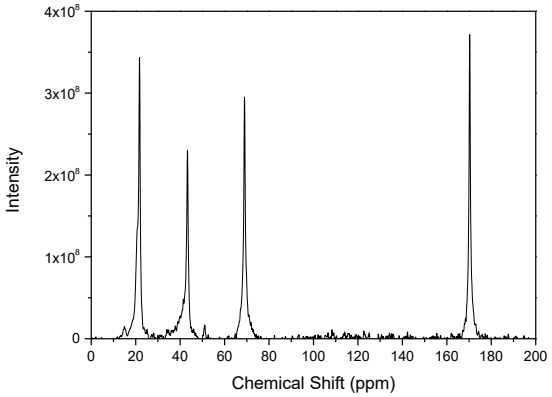

(a)

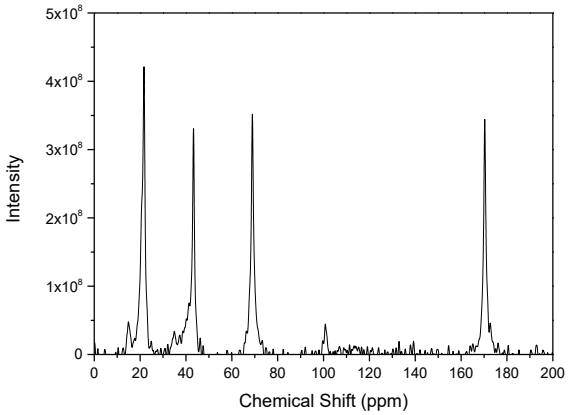

(b)

Figure 95. NMR spectra for PHBH X131A (a) and X151A (b).

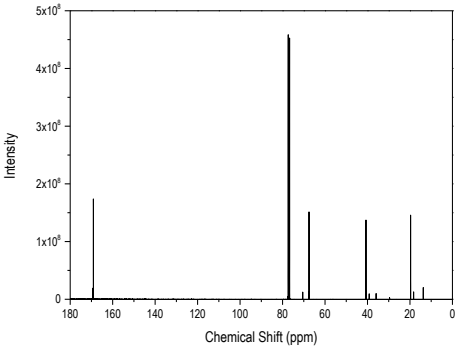

(a)

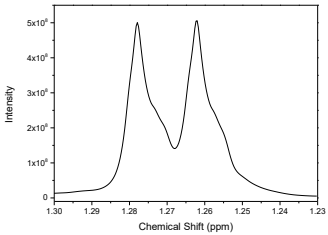

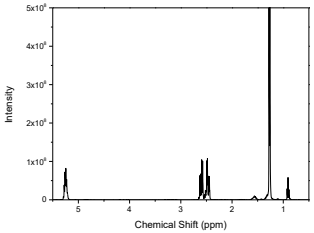

(b) (c)

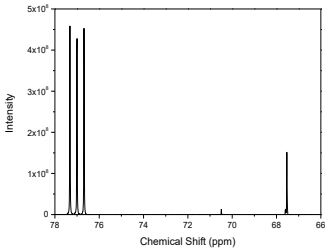

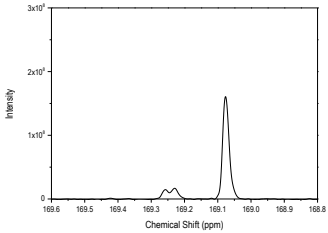

(d) (e)

Figure 96. ^{13}C MAS spectrum of X151A (a) and relative magnifications (b-e).

In order to understand the type of copolymer (block, random, blend), liquid NMR analysis was carried out on the X151A. NMR 13C spectrum and its magnification are reported in Figure 96. From the magnifications of the 13C spectrum (in particular Figure 96d and Figure 96e), it was possible to state that all the carbon resonances of PHBH were split into dial, triad or quadrupole. This reflected the sensitivity of the carbon nuclei to different chemical micro-environments of co-monomer sequences 3HB and 3HH and this was typical of a random copolymer [236].

Melt Flow Index test gave us same results for both materials, 7.4 ± 0.9 g/10min and 7.6 ± 0.4 g/10min for X131A and X151A respectively.

The degradation process of filaments, as shown in *Figure* 97, starts at about 250°C for both copolymers and reaches a maximum around 270°C. The two materials perform quite similarly and no signifcative differences can be highlighted.

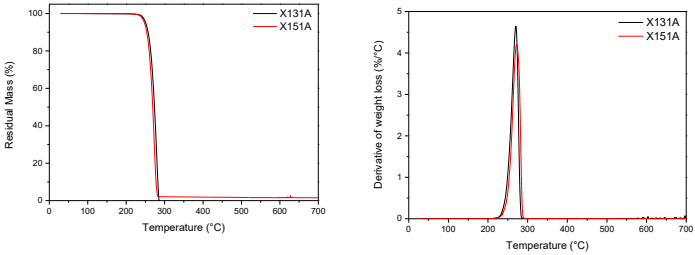

(a) (b)

Figure 97. Mass loss (a) and their differential curves (b) for X131A and X151A.

DSC measurements were performed on both copolymers to evaluate the main thermal properties. In Figure 98 it is possible to observe the different behavior of the two materials due to the different composition in term of weight fraction of PHH. It is evident that PHBH X151A is less prone to crystallize than X131A. After the first heating scan, a crystallinity fraction of 42% and 33% can be calculated for X131A and X151A, respectively. This difference made X151A a good candidate for 3D printing due to less problems of warping or detachment from the building plate due to thermal stresses.

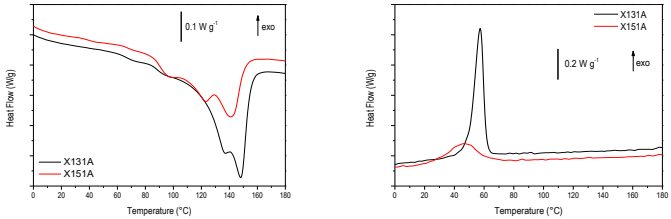

(a) (b)

Figure 98. First heating (a) and cooling (b) DSC curves for PHBH X131A and X151A.

Representative stress-strain curves of filaments and 3D printed specimen made of X131A and X151A are shown in Figure 99. A different mechanical behavior can be observed for the two materials. In particular, due to its higher content of 3HH copolymer and the lower crystallinity, X151A results more flexible and shows a higher deformation at break. These conditions made it more interesting for 3D printing application as packaging materials in alternative to the more rigid and brittle PLA.

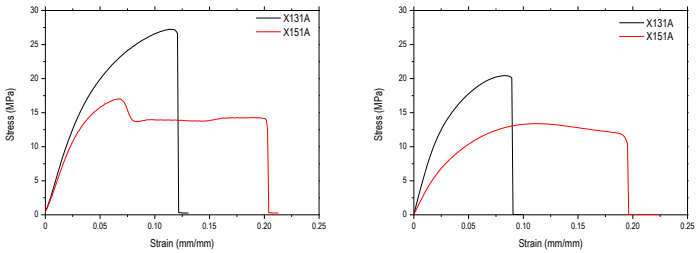

(a) (b)

Figure 99. Representative stress vs strain curves for filaments (a) and 3D printed dumbbell specimen of PHBH X131A and X151A.

8.4. Results and discussion

8.4.1. Morphology

The cryogenic fracture surfaces of neat PHBH and relative nanocomposite filaments are shown in Figure 100. Nanocellulose appeared homogeneously distributed inside the matrix without a specific preferential orientation. The presence of aggregates increased with the increasing concentration of NFC; this could be responsible of a decrease of the ultimate properties of the prepared nanocomposite at the highest concentration. A good filler-matrix interfacial adhesion could be observed over the whole range of investigated compositions.

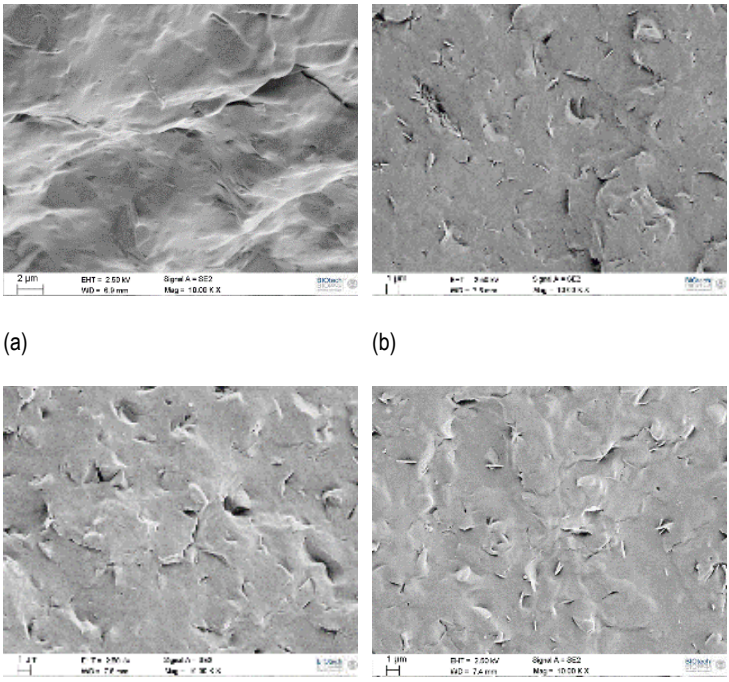

(a) (b)

(c) (d)

Figure 100. SEM picture of cryo fractured surface of PHBH filaments with the addition of (a) 0 wt%, (b) 0.5 wt%, (c) 1 wt% and (d) 3 wt% of NFC.

In Figure 101, lower magnification pictures of cryo-fracture surfaces of neat PHBH and nanocomposite 3D printed are presented to investigate the effects of NFC incorporation on the morphology of the printed structure. As revealed by micrographs reported in Figure 101, the deposited filaments appear with ellipsoidal section for the neat polymer and became more circular as the NFC content increases. The increase in viscosity induced by increasing concentration of NFC, that in turn make the printing process more difficult because less material passes through the nozzle, caused the above-mentioned behavior. In the cryogenic fracture surface of the 3D printed specimen made by neat PHBH, the contour between the filaments can be hardly identified, but it becomes more and more evident in the samples loaded with increasing amount of filler. At the highest concentrations of NFC, filaments can be clearly identified inside the printed part and low adhesion between subsequent layers can be expected.

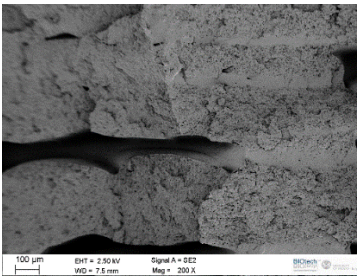

(a)

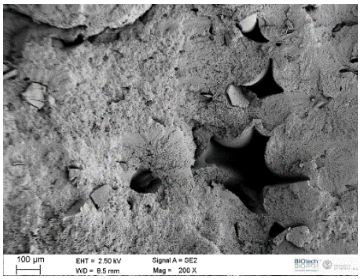

(b)

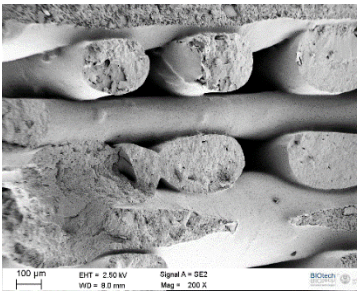

(c)

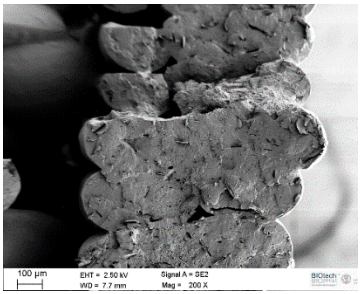

(d)

Figure 101. Low magnification SEM pictures of cryo fractured surface of PHBH 3D printed specimen with the addition of (a) 0 wt%, (b) 0.5 wt%, (c) 1 wt% and (d) 3 wt% of NFC.

8.4.2. Thermal properties

The study of the thermal degradation behavior of the nanocomposite materials was performed to assess their resistance to high temperature and to delineate the processing window for these materials. Therefore, thermogravimetric tests were carried out on PHBH / NFC filaments. From the TGA thermograms reported in Figure 102, all the samples were characterized by a single degradation step that started at 260°C, while the maximum mass loss rate occurred at 285°C. No particular effects were detected upon nanofiller addition.

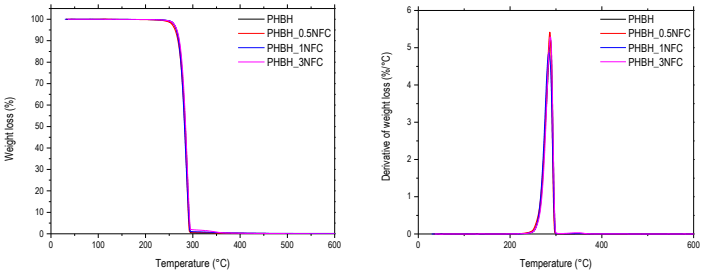

(a) (b)

Figure 102. Thermogravimetric curves (a) and derivative thermogravimetric curves for neat PVA and its nanocomposites filaments.

Thermal properties of the PHBH and PHBH / NFC composites were determined using differential scanning calorimetry (DSC). The glass transition temperature, the melting temperature and degree of crystallinity obtained from the DSC are reported in Table 31, while representative DSC curves are shown in Figure 103. The reference enthalpy of fusion of 100% crystalline PHBH was taken equal to 146 J/g [142]. Fibrillated nanocellulose is found to slightly modify the thermal properties of PHBH. In particular, it is possible to appreciate a slightly decrease of the glass transition temperature and the crystallization temperatures. Melting temperature (Tm) is not affected by the amount filler. NFC acted as a nucleating agent since the crystallinity fraction (Xc_h) is slightly increased by the amount of NCF and this is particularly evident during the cooling scan where the fraction of material crystallized (Xc_c) moved from 9.2% of neat PHBH to 15.2% of PHBH_03NFC.

This behavior is in accordance to other studies on PHA / cellulose fiber composite material and it is generally explained by considering that the motion of the polymer chains can be modified by the presence of nanofibers [237-239].

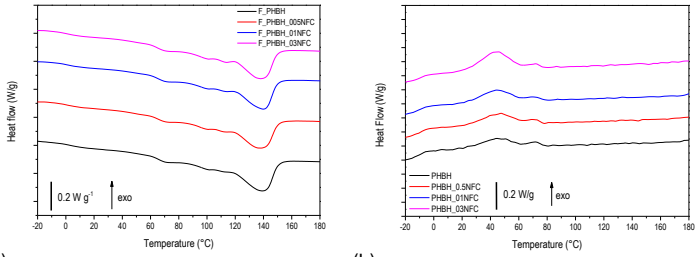

(a) (b)

Figure 103. First heating (a) and cooling (b) DSC curves for PHBH and relative nanocomposite filaments.

Table 31. Glass transition temperature, cold crystallization temperature, melting temperature, crystallinity fraction, crystallization temperature during cooling and crystallinity fraction after the cooling scan for PHBH and relative nanocomposite as measured by DSC first heating scan.

	Tg (°C)	Tcc (°C)	Tm (°C)	Xc_h (%)	Tc (°C)	Xc_c (%)
F_PHBH	-2.8	49.2	140.3	25.9	44.6	9.2
F_PHBH_0.5NFC	-3.0	47.3	140.5	24.6	47.4	9.8
F_PHBH_01NFC	-3.9	47.0	140.5	27.9	43.8	10.2
F_PHBH_03NFC	-3.2	46.3	140.4	26.8	46.1	15.2

8.4.3. Mechanical properties

The dynamic-mechanical properties of the PHBH / NFC composite materials were measured using DMA. This method gave crucial insights about the effect of the nanofiller and temperature interactions of the materials. In Figure 104 storage modulus, loss modulus and tan δ curves for filaments and 3D printed samples are reported. The macro structure of 3D printed specimen induces lower values for E' and E'' compared to the neat filaments because the real cross-section was not taken into account. It is possible to note that 3D printed samples manifest higher values of tan δ peak with respect to filaments. This could be possibly associated to the increase in damping performance of a cellular-like structure that it characterizes the additively manufactured component. Storage modulus of filaments increases with the increasing amount of NFC [239]. E' values drop firstly around the glass transition temperature and then a shoulder associated to the cold crystallization process can be noticed as described in DSC curves for these kinds of composites. The highest value of the loss modulus of PHBH and its nanocomposites occurs slightly above the glass transition temperature for both filaments and 3D printed samples.

Tan δ expressed as the ratio of E'' on E' is an estimation of the energy dissipated during the cyclic testing. The tan δ peaks are found in same temperature range of the E'' peaks. A decrease of the tan δ peak values is clearly identified for 3D printed samples and, according to literature [239], it can be associated to the reduced energy losses in the interfacial regions This reduction in damping properties with the addition of filler agreed upon with the results from DSC and the reduced movement of the polymer chains after the introduction of NFC.

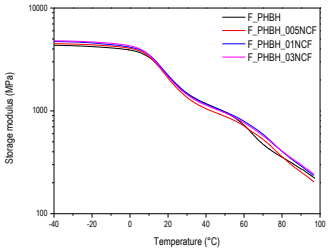

(a)

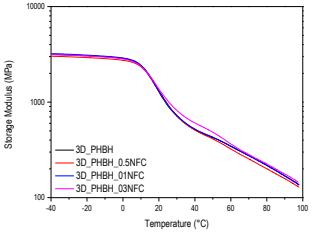

(b)

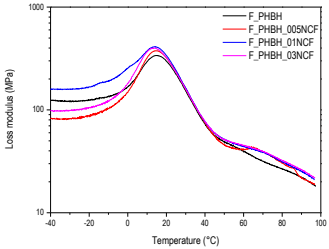

(c)

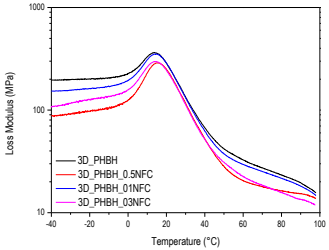

(d)

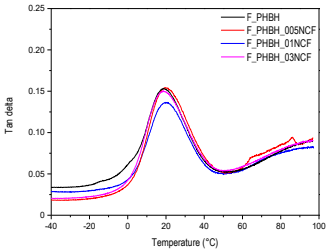

(e)

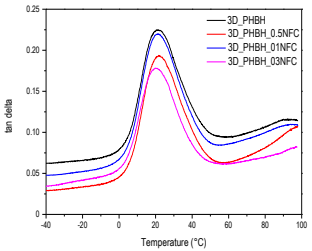

(f)

Figure 104. Storage modulus (a – b), loss modulus (c – d) and tan δ (e – f) curves for filaments and 3D printed samples respectively.

The mechanical properties such as elastic modulus, tensile strength, elongation at break and tensile energy at break (TEB) of neat PHBH and PHBH nanocomposites were investigated by tensile test at room temperature on both filaments and 3D printed samples, the results are summarized in Table 32. An appreciable increment of the elastic modulus (40% with respect to the neat PHBH) is measured for filament sample containing 0.5wt% of nanocellulose. This sample showed also the highest tensile strength. For higher NFC contents, the stress at break decreases but remains higher than the ones of the neat matrix. This behavior can be related with a better dispersion of nanofiller at very low concentration (0.5wt%).

Table 32. Mechanical properties of filaments and 3D printed samples.

	Elastic (MPa)	Stress at (MPa)	Strain at (%)	TEB (J mm^{-2})
F_PHBH	897 ±157	14.8 ± 4.2	10.4 ± 3.0	1.6 ± 0.5
F_PHBH_0.5NFC	1259 ± 221	16.8 ± 3.5	9.5 ± 1.1	1.6 ± 0.2
F_PHBH_01NFC	1051 ± 269	15.7 ± 1.5	10.9 ± 0.9	1.6 ± 0.3
F_PHBH_03NFC	1014 ± 214	15.9 ± 2.1	10.2 ± 2.3	1.4 ± 0.4
3D_PHBH	931 ± 150	12.6 ± 2.6	10.7 ± 1.8	1.2 ± 0.1
3D_PHBH_0.5NFC	807 ± 74	14.0 ± 1.7	12.2 ± 1.8	1.7 ± 0.3
3D_PHBH_01NFC	770 ± 44	13.5 ± 0.9	9.5 ± 1.0	1.1 ± 0.1
3D_PHBH_03NFC	681 ± 112	9.3 ± 2.0	9.3 ± 1.5	0.8 ± 0.1

After 0.5 wt% of NFC, the stiffness of 3D printed samples decreases as the filler content increases. This effect can be caused by the worsening of adhesion between layers inside the specimen with the increasing amount of nanofiller as it is possible to notice in Figure 101. This conclusion is supported by the little variation of the density of the printed specimen with R-factor in a narrow range as highlighted in Figure 105a. The highest stress at break can be found for the concentration of 0.5 wt% for both filaments and 3D printed samples. These specimens also show the highest strain at break and tensile energy at break values.

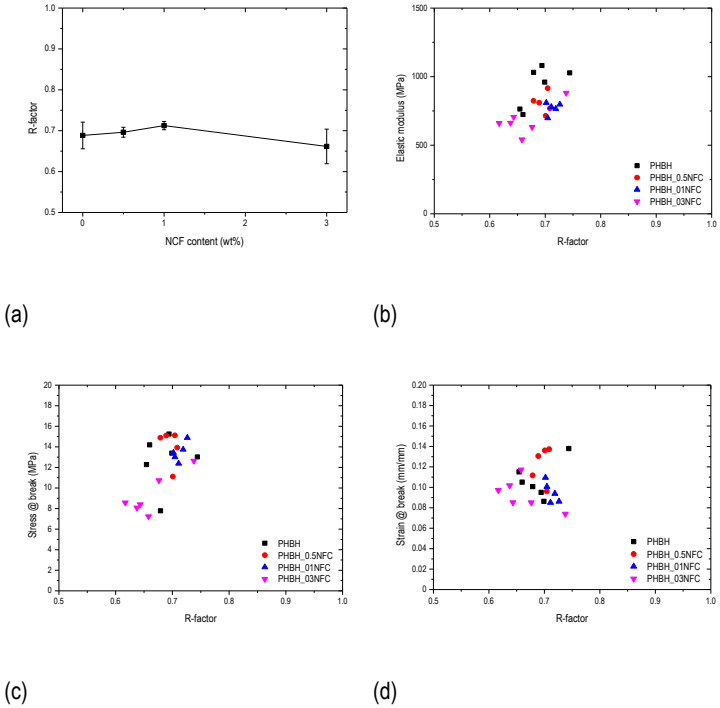

Figure 105. R-factor as a function of the NFC content (a) and the main mechanical parameters versus R-factor for all the tested 3D printed specimen. R-factor = 1 means bulk material without porosity.

The isothermal creep compliance curves for filaments (a) and 3D printed samples (b) are reported in Figure 106. A proportional reduction of the creep compliance with the increase of filler content indicates an improvement of the dimensional stability. After the introduction of 3wt% of NFC, a 41% decrease of the creep compliance at 3600 s is measured on the filaments while a 17% decrease is observed for 3D printed samples. The time-dependent creep compliance curves of these materials can be well fitted by a power law model (R-square values higher than 0.99). The values of the fitting parameters are summarized in Table 33.

The higher values of the creep compliance for 3D printed samples with respect to the filaments (28% higher for 3D printed PHBH in respect of PHBH filament) could be mainly associated to higher values of the elastic creep component D_e. This different behavior between filaments and 3D printed samples could be explained by the different macrostructure of printed specimen compared to filaments. For as concern the decrease of the creep compliance due to the addition of nanofibrillated cellulose, D_e component decreases by 24% for filaments and 19% for 3D printed samples after the addition of 3wt% on NFC. However, the main role in the reduction of creep compliance by the NFC is associated with the decrease of parameter k, which account for the time-dependent response to the applied stress. For samples containing 3wt% of NFC a drop of 55% and 40% for filament and 3D printed sample can be respectively observed. These observation matched with the increase in stiffness previously reported.

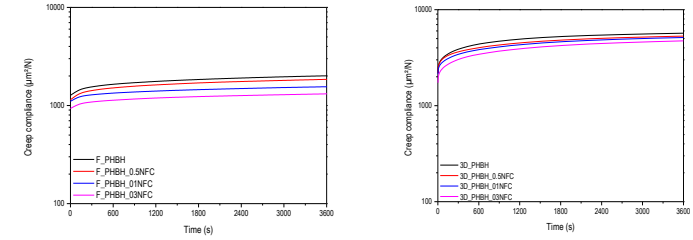

(a) (b)

Figure 106. Creep compliance curves for PHBH filament (a) 3D printed samples (b).

Table 33. Fitting parameters of Findley's model on the creep behavior of filament and 3D printed samples nano-composite.

	De ($\mu m^2/N$)	k ($\mu m^2/N$)	n
F_PHBH	1212 ± 8	201 ± 4	0.335 ± 0.002
F_PHBH_0.5NFC	1095 ± 6	197 ± 4	0.327 ± 0.002
F_PHBH_01NFC	1046 ± 25	122 ± 11	0.355 ± 0.011
F_PHBH_03NFC	927 ± 6	92 ± 3	0.349 ± 0.005
3D_PHBH	2061 ± 27	260 ± 18	0.333 ± 0.010
3D_PHBH_0.5NFC	2026 ± 30	289 ± 15	0.301 ± 0.006
3D_PHBH_01NFC	1902 ± 41	239 ± 18	0.324 ± 0.008
3D_PHBH_03NFC	1684 ± 12	158 ± 7	0.369 ± 0.007

Chapter IX

9. Final remarks and future perspectives

Three types of commercially available polymers, polyvinyl alcohol (PVA), polylactic acid (PLA) and poly(3-hydroxybutyrate-co-3-hydroxyhexanoate) (PHBH) were studied in this research upon the addition of different types of cellulosic materials: microcrystalline cellulose (MCC), nanocrystalline cellulose (CNC), nanofibrillated cellulose (NFC) and lauryl functionalized nanocellulose (LNC). Micro and nanocomposite materials were prepared with the aid of different mixing techniques. The obtained composites were the starting point to produce filaments to feed a 3D printer based on Fused Deposition Modeling technology. A deeply characterization on the thermo-mechanical properties at different processing stage was carried out in order to understand the effect of the filler at different concentration upon addition to the matrices.

The results of the research are graphically resumed in Table 34, where the maximum amount of the specific filler in the specific polymer matrix that it was possible to print with FDM, the working temperatures of the printer and the trend of the main thermo-mechanical parameters upon the introduction of the selected filler are presented.

Table 34. Schematic resume of the trend upon the addition of the selected filler in the polymeric matrix presented in this work.

		Max filler	T_{3D}	T_B	T_g	T_c	X_C	T_m	E	σ_B	ε_B	D_e	Optimal filler
PVA	MCC	5	230	40	↑	↔	↓	↑	↑	↑	↓	↓	5
	CNC	10	230	40	↔	↔	↓	↑	↑	↑	↓	↓	5
PLA	MCC	10	220	40	↔	↓	↑	↑	↑	↑	↓	n.t.	1
	MAH-MCC	10	220	40	↓	↓	↑	↑	↑	↑	↓	n.t.	5
	LNC	20	n.p.	n.p.	↔	↑	↓	↑	↓	↑	↑	↑	6.5
	NCF	3	200-180	75	↔	↓	↑	↔	↓	↑	↑	↑	1
PHBH	NCF	3	200-180	75	↔	↓	↓	↔	↑	↑	↓	↓	1

Max filler: maximum amount of filler used in this work in weight percent
T_{3D}: temperature of the nozzle during printing in °C
T_B: temperature of the bed during printing in °C
T_g: glass transition temperature
T_C: crystallization temperature on cooling
X_C: crystallinity fraction
T_m: melting temperature
E: elastic modulus
σ_B: stress at break
ε_B: strain at break
D_e: creep compliance at 1 hour
Optimal filler: optimal concentration of filler in the selected matrix in weight percent according with thermomechanical results
n.p.: not processed
n.t.: not tested

Nanocellulose was obtained starting from microcrystalline cellulose with two different techniques. Crystalline nanocellulose was successfully prepared by using acid hydrolysis method. Nanocellulose obtained with this method appeared as rod-like particles with an average size of about 200 to 500 nm in length and around 5-10 nm in diameter as observed by AFM. Ultrasonication offers a possible more ecosustainable way to extract nanocellulose without the use of dangerous chemicals. Acid hydrolysis leads to the isolation of cellulose's nanocrystals from microcellulose with mechanical properties higher than the nanofibrillated one and smaller dimensions. However, the use of sulfuric acid left the cellulose less resistant to higher temperature compared to the ultrasonication treatments limiting its use in some manufacturing process like melt mixing and extrusion where the melting temperature of the polymer must be reached. In this work, nanocellulose was obtained in an aqueous suspension, and its use in hydrophobic materials required that it be dried prior to incorporation in non-water-soluble polymers such as PLA or PHB. It was highlighted the partial reaggregation upon the removal of water and this issue has to be resolved to exploit the full potential of fibrillated NC in this kind of applications.

- For as concern the addition of micro and nano cellulose to PVA, it was measured a significant improvement of the mechanical properties in both filaments and 3D printed samples. CNC was efficient to limit the rubber-like behavior of PVA leading to a possible extension in the field of application for this material.

- The reinforcement effect of nanocellulose in polyesters thermoplastic matrices was more effective at low concentrations (0.5 - 1 wt%) due to the re-aggregations of NCF upon water removal. The stiffening effect of cellulose in hydrophobic polymer matrices was relatively lower respect to PVA due to limited chemical interaction between hydrophilic filler and hydrophobic matrices. The increase in elastic modulus upon the addition of cellulose was also followed by an increase of creep resistance. Modifying the chemistry of the filler and the matrix was taken in account during this research. Maleic anhydride is a common solution to improve adhesion in thermoplastic polymers and its use in PLA improved the filler-matrix interface. Maleic anhydride, even if is biodegradable, is derived from oil and the exposure to maleic anhydride may cause irritation to the respiratory tract, eyes, exposed mucosa and skin. Renewable and less

hazardous compatibilizers may be used to substitute MAH and itaconic acid is selected as an alternative compatibilizer in subsequent researches. A decrease in stiffness was observed with the addition of lauryl functionalized nanocellulose to PLA due to the presence of a soft interphase as evidenced also by gas permeability tests. The results on films only of PLA-LNC seemed promising to be applied even in 3D printing due to the increase in the mechanical properties.

- Mechanical testing of 3D printed samples underlined the lack of standard for this kind of technologies. In this research, ISO527, a generic standard for thermoplastic material, was adopted with constant building parameters through all the research. Some building geometries resulted to be not suitable for providing reliable results. Some infill geometries showed a rupture in geometrical defects (orientation 0°/0°) or through the detachment of some part of the specimen (orientation 0°/90°). Great results in terms of reproducibility of the tests and a fracture located correctly inside the gauge length were found for the infill orientation ± 45°. Nevertheless, the building geometries, that worked well for the polymer matrices presented in this research, were hard to be manufactured with other polymers and brought to meaningless results [240], so building parameters must be chosen correctly for each type of polymer.

- 3D printed specimen resulted to be highly affected by defects introduced during the printing inside the specimen, but it was highlighted that their magnitude can be evaluated through the measurement of the apparent density. The ratio between the apparent and the theoretical density, R-factor, helped to discern the results from mechanical tests between material properties and quality of 3D printed specimen. Components made by FDM could be affected by many different errors such as no adhesion to bed plate, under extrusion, over extrusion, gaps inside the layers, overheating, layer shifting, layer separation, clogging of the extruder, inconsistent extrusion, warping, dimensional accuracy and so on. All the mentioned problems could be randomly present inside the specimen and so it became very difficult to model the mechanical properties at a millimetric scale [241]. However, in some cases it's possible to observe a trend between the apparent density and the stiffness or the stress at break.

These latter points are now deeply under investigation to propose a valid model to forecast the mechanical properties of 3D printed materials.

All the three different biodegradable polymer matrices have been processed with the appropriate kind of cellulose. These composites resulted to be an interesting material to be used with 3D printer in order to produce reinforced objects from natural resources. For each system, biodegradable polymer and cellulose filler, an optimal composition in weight percent has been determined.

Publications on peer reviewed journals

- Cataldi A., Rigotti D., Nguyen V. D. H., Pegoretti A.: "Polyvinyl alcohol reinforced with crystalline nanocellulose for 3D printing application" in Materials Today Communications, Vol. 15, p. 236-244, (2018).
- Valentini F., Dorigato A., Rigotti D., Pegoretti A.: “Polyhydroxyalkanoates / nanocellulose composites for additive manufacturing” in Journal of Polymers and the Environment, (2019).
- Rigotti D., Checchetto R., Tarter S., Caretti D., Rizzuto M., Fambri L., Pegoretti A.: “Polylactic acid - lauryl functionalized nanocellulose nanocomposites: microstructural, thermo-mechanical and gas transport properties” in Express Polymer Letters. (2019).
- Checchetto, R., Rigotti, D., Pegoretti, A., Miotello A.: “Chloroform desorption from poly(lactic acid) nanocomposites: a thermal desorption spectroscopy study” in Pure and Applied Chemistry (2019).

Acknowledgements

I would like to gratefully thank my advisors Prof. Alessandro Pegoretti and Prof. Luca Fambri for giving me the opportunity to live this experience in the Laboratories of Polymers and Composites. Their guidance helped me in all the time of research, I could not have imagined having better advisors and mentors for my Ph.D. I kindly thank all professors, technicians and colleagues working at the department of Industrial Engineering (University of Trento) for their support on some experimental analysis. Thanks are due as well *to Prof. Devid Maniglio, Prof. Riccardo Checchetto, Prof. Daniele Caretti, Prof. Rani Elhajjar, Dr. Gloria Ischia, Dr. Alexia Conci and Mr. Lorenzo Moschini. Obviously, special acknowledgments are due to the technicians, Claudia Gavazza and Alfredo Casagranda for their special help. My sincere thanks also go to Prof. Andrea Dorigato for its valuable advice during these years and Dr. Annalisa Cataldi for helping me start this adventure. I thank my fellow labmates, Haroon, Prumnea, Giulia and Francesco for the great time we spent working together and for all the fun we have had in the last three years. My special gratitude is given to my parents Assunta and Valentino, for their precious support throughout these years. Last but not the least, I would like to thank my grandfather Eduino, who follows me reaching this goal from above.*

References

[1] Vroman I., L. Tighzert, *Biodegradable Polymers*. Materials, **2009**. 2(2): p. 307-344.

[2] Satyanarayana K.G., G.G.C. Arizaga, F. Wypych, *Biodegradable composites based on lignocellulosic fibers—An overview*. Progress in Polymer Science, **2009**. 34(9): p. 982-1021.

[3] Ford S., M. Despeisse, *Additive manufacturing and sustainability: an exploratory study of the advantages and challenges*. Journal of Cleaner Production, **2016**. 137: p. 1573-1587.

[4] DellaSala D.A., *The Carbon Cycle and Global Change: Too Much of a Good Thing* in *Reference Module in Earth Systems and Environmental Sciences*. **2013**, Elsevier.

[5] Ebi K.L., *Climate Change and Health A2 - Nriagu, J.O* in *Encyclopedia of Environmental Health*. **2011**, Elsevier: Burlington. p. 680-689.

[6] DellaSala D.A., *Global Change* in *Reference Module in Earth Systems and Environmental Sciences*. **2013**, Elsevier.

[7] Gebler M., A.J.M. Schoot Uiterkamp, C. Visser, *A global sustainability perspective on 3D printing technologies*. Energy Policy, **2014**. 74: p. 158-167.

[8] Cesaretti G., E. Dini, X. De Kestelier, V. Colla, L. Pambaguian, *Building components for an outpost on the Lunar soil by means of a novel 3D printing technology*. Acta Astronautica, **2014**. 93: p. 430-450.

[9] Wong J.Y., A.C. Pfahnl, *3D Printing of Surgical Instruments for Long-Duration Space Missions*. Aviation, Space, and Environmental Medicine, **2014**. 85(7): p. 758-763.

[10] Kading B., J. Straub, *Utilizing in-situ resources and 3D printing structures for a manned Mars mission*. Acta Astronautica, **2015**. 107: p. 317-326.

[11] Li W., Q. Wu, X. Zhao, Z. Huang, J. Cao, J. Li, S. Liu, *Enhanced thermal and mechanical properties of PVA composites formed with filamentous nanocellulose fibrils*. Carbohydrate Polymers, **2014**. 113: p. 403-410.

[12] Murariu M., P. Dubois, *PLA composites: From production to properties*. Advanced drug delivery reviews, **2016**. 107: p. 17-46.

[13] Tashiro K., M. Kobayashi, *Theoretical evaluation of three-dimensional elastic constants of native and regenerated celluloses: role of hydrogen bonds*. Polymer, **1991**. 32(8): p. 1516-1526.

[14] Eichhorn S.J., A. Dufresne, M. Aranguren, N.E. Marcovich, J.R. Capadona, S.J. Rowan, C. Weder, W. Thielemans, M. Roman, S. Renneckar, W. Gindl, S. Veigel, J. Keckes, H. Yano, K. Abe, M. Nogi, A.N. Nakagaito, A. Mangalam, J. Simonsen, A.S. Benight, A. Bismarck, L.A. Berglund, T. Peijs, *Review: current international research into cellulose*

nanofibres and nanocomposites. Journal of Materials Science, **2009**. 45(1): p. 1-33.

[15] Lagerwall J.P.F., C. Schütz, M. Salajkova, J. Noh, J. Hyun Park, G. Scalia, L. Bergström, *Cellulose nanocrystal-based materials: from liquid crystal self-assembly and glass formation to multifunctional thin films*. NPG Asia Materials, **2014**. 6(1): p. 80.

[16] Fernandes E.M., R.A. Pires, J.F. Mano, R.L. Reis, *Bionanocomposites from lignocellulosic resources: Properties, applications and future trends for their use in the biomedical field*. Progress in Polymer Science, **2013**. 38(10-11): p. 1415-1441.

[17] Abdul Khalil H.P.S., A.H. Bhat, A.F. Ireana Yusra, *Green composites from sustainable cellulose nanofibrils: A review*. Carbohydrate Polymers, **2012**. 87(2): p. 963-979.

[18] Bandyopadhyay-Ghosh S., S.B. Ghosh, M. Sain, *The use of biobased nanofibres in composites* in *Biofiber Reinforcements in Composite Materials*, F. Omar and S. Mohini Editors. **2015**, Woodhead Publishing. p. 571-647.

[19] Berman B., *3-D printing: The new industrial revolution*. Business Horizons, **2012**. 55(2): p. 155-162.

[20] El-Sonbati A.Z., *Thermoplastic Elastomers*. **2012**, Rijeka, Croatia: InTech.

[21] Drobny J.G., *Handbook of Thermoplastic Elastomers*. **2007**: Matthew Deans.

[22] Dorigato A., V. Moretti, S. Dul, S. Unterberger, A. Pegoretti, *Electrically conductive nanocomposites for fused deposition modelling*. Synthetic Metals, **2017**. 226: p. 7-14.

[23] Dul S., L. Fambri, A. Pegoretti, *Fused deposition modeling with ABS-graphene nanocomposites*. Composites Part A: Applied Science and Manufacturing, **2016**. 85: p. 181-191.

[24] Dul S., L. Fambri, A. Pegoretti, *Filaments production and fused deposition modelling of ABS/carbon nanotubes composites*. Nanomaterials, **2018**. 8(1).

[25] Steve Wilkinson N.C., *3D Printing and Sustainable Product Development* in *Green Information Technology*, M. Kaufmann Editor. **2015**.

[26] Wilkinson S., N. Cope, *3D Printing and Sustainable Product Development* in *Green Information Technology*, M. Dastbaz, C. Pattinson, and B. Akhgar Editors. **2015**. p. 161-183.

[27] Christian Weller R.K., Frank T. Piller, *Economic implications of 3D printing: Market structure models in light of additive manufacturing revisited*. Int. J. Production Economics, **2015**. 164: p. 43-56.

[28] Malte Gebler A.J.M.S.U., Cindy Visser, *A global sustainability perspective on 3D printing technologies*. Energy Policy, **2014**. 74: p. 158-167.

[29] L.M. Galantucci F.L., G. Percoco, *Experimental study aiming to enhance the surface finish of fused deposition modeled parts*. Manufacturing Technology, **2009**. 58: p. 189–192.
[30] Campbell T., C. Williams, O. Ivanova, B. Garrett, *Could 3D Printing Change the World?* Strategic Foresight Report, **2011**.
[31] Huang Y., M.C. Leu, J. Mazumder, A. Donmez, *Additive Manufacturing: Current State, Future Potential, Gaps and Needs, and Recommendations*. Journal of Manufacturing Science and Engineering, **2015**. 137(1): p. 1-10.
[32] Baumann F., D. Roller, *Survey on Additive Manufacturing, Cloud 3D Printing and Services*. **2017**.
[33] Forster A.M., *Materials testing standards for additive manufacturing of polymer materials: State of the art and standards applicability*. NIST Interagency/Internal Report (NISTIR), **2015**. (8059): p. 67-123.
[34] Hoskins T.J., K.D. Dearn, S.N. Kukureka, *Mechanical performance of PEEK produced by additive manufacturing*. Polymer Testing, **2018**. 70: p. 511-519.
[35] Haleem A., M. Javaid, *Polyether ether ketone (PEEK) and its manufacturing of customised 3D printed dentistry parts using additive manufacturing*. Clinical Epidemiology and Global Health, **2019**.
[36] De Leon A.C., Q. Chen, N.B. Palaganas, J.O. Palaganas, J. Manapat, R.C. Advincula, *High performance polymer nanocomposites for additive manufacturing applications*. Reactive and Functional Polymers, **2016**. 103: p. 141-155.
[37] Materials A.S.f.T.a., *ASTM F42 – Additive Manufacturing.* **2010**.
[38] International A., *ASTM F2792-10 Standard Terminology for Additive Manufacturing Technologies.* **2010**.
[39] Serrano A., A.M. Borreguero, I. Garrido, J.F. Rodríguez, M. Carmona, *The role of microstructure on the mechanical properties of polyurethane foams containing thermoregulating microcapsules*. Polymer Testing, **2017**. 60: p. 274-282.
[40] Lee J.-Y., J. An, C.K. Chua, *Fundamentals and applications of 3D printing for novel materials*. Applied Materials Today, **2017**. 7: p. 120-133.
[41] International A., *ASTM D6866-16:Standard Test Methods for Determining the Biobased Content of Solid, Liquid, and Gaseous Samples Using Radiocarbon Analysis.* **2016**.
[42] *Biopolymers: Reuse, recycling, and disposal*. **2013**: Elsevier.
[43] International A., *ASTM 6400-12: Labeling of Plastics Designed to be Aerobically Composted in Municipal or Industrial Facilities.* **2012**.
[44] *Handbook of Biodegradable Polymers*. **2014**: Rapra Technology Limired.
[45] Bioplastic E., *http://www.european-bioplastics.org/*.
[46] Solaro R., A. Corti, E. Chiellini, *Biodegradation of poly(vinyl alcohol) with different molecular weights and degree of hydrolysis*. Polymers for Advanced Technologies, **2000**. 11(8-12): p. 873-878.

[47] Ojeda T., *Polymers and the Environment*. **2013**.
[48] Chiellini E., A. Corti, S. D'Antone, R. Solaro, *Biodegradation of poly (vinyl alcohol) based materials*. Progress in Polymer Science, **2003**. 28(6): p. 963-1014.
[49] Bolto B., T. Tran, M. Hoang, Z. Xie, *Crosslinked poly(vinyl alcohol) membranes*. Progress in Polymer Science, **2009**. 34(9): p. 969-981.
[50] Fink J.K., *Handbook of Engineering and Speciality Thermoplastics*. **2010**: Wiley.
[51] Olabisi O.E., Adewale, K. , *Handbook of Thermoplastics*. **2016**: Scrivener Publishing LLC.
[52] Ismail H., N. Zaaba, *Effects of Poly(vinyl alcohol) on the Performance of Sago Starch Plastic Films*. **2014**.
[53] Tager A.A., A.A. Anikeyeva, L.V. Adamova, V.M. Andreyeva, T.A. Kuz'mina, M.V. Tsilipotkina, *The effect of temperature on the water solubility of polyvinyl alcohol*. Polymer Science U.S.S.R., **1971**. 13(3): p. 751-758.
[54] Thomas P.S., J.P. Guerbois, G.F. Russell, B.J. Briscoe, *FTIR Study of the Thermal Degradation of Poly(vinyl Alcohol)*. Journal of Thermal Analysis and Calorimetry, **2001**. 64(2): p. 501-508.
[55] Peng Z., L.X. Kong, *A thermal degradation mechanism of polyvinyl alcohol/silica nanocomposites*. Polymer Degradation and Stability, **2007**. 92(6): p. 1061-1071.
[56] Peng Z., L.X. Kong, S.D. Li, *Thermal properties and morphology of a poly(vinyl alcohol)/silica nanocomposite prepared with a self-assembled monolayer technique*. Journal of Applied Polymer Science, **2005**. 96(4): p. 1436-1442.
[57] Li S.-D., Z. Peng, L.X. Kong, J.-P. Zhong, *Thermal Degradation Kinetics and Morphology of Natural Rubber/Silica Nanocomposites*. Journal of Nanoscience and Nanotechnology, **2006**. 6(2): p. 541-546.
[58] Gilman J.W., C.L. Jackson, A.B. Morgan, R. Harris, E. Manias, E.P. Giannelis, M. Wuthenow, D. Hilton, S.H. Phillips, *Flammability Properties of Polymer−Layered-Silicate Nanocomposites. Polypropylene and Polystyrene Nanocomposites*. Chemistry of Materials, **2000**. 12(7): p. 1866-1873.
[59] Lee S.-Y., D.J. Mohan, I.-A. Kang, G.-H. Doh, S. Lee, S.O. Han, *Nanocellulose reinforced PVA composite films: Effects of acid treatment and filler loading*. Fibers and Polymers, **2009**. 10(1): p. 77-82.
[60] Li W., X. Zhao, Z. Huang, S. Liu, *Nanocellulose fibrils isolated from BHKP using ultrasonication and their reinforcing properties in transparent poly (vinyl alcohol) films*. Journal of Polymer Research, **2013**. 20(8).
[61] Cano A.I., M. Cháfer, A. Chiralt, C. González-Martínez, *Biodegradation behavior of starch-PVA films as affected by the incorporation of different antimicrobials*. Polymer Degradation and Stability, **2016**. 132: p. 11-20.

[62] Corti A., R. Solaro, E. Chiellini, *Biodegradation of poly(vinyl alcohol) in selected mixed microbial culture and relevant culture filtrate*. Polymer Degradation and Stability, **2002**. 75(3): p. 447-458.
[63] Chiellini E., A. Corti, R. Solaro, *Biodegradation of poly(vinyl alcohol) based blown films under different environmental conditions*. Polymer Degradation and Stability, **1999**. 64(2): p. 305-312.
[64] R Chandra R.R., *Biodegradable polymers*. Progress in Polymer Science, **1998**. 23(7): p. 1273-1335.
[65] Cox S.C., J.A. Thornby, G.J. Gibbons, M.A. Williams, K.K. Mallick, *3D printing of porous hydroxyapatite scaffolds intended for use in bone tissue engineering applications*. Materials science & engineering. C, Materials for biological applications, **2015**. 47: p. 237-247.
[66] Goyanes A., A.B. Buanz, A.W. Basit, S. Gaisford, *Fused-filament 3D printing (3DP) for fabrication of tablets*. International journal of pharmaceutics, **2014**. 476(1-2): p. 88-92.
[67] Goyanes A., H. Chang, D. Sedough, G.B. Hatton, J. Wang, A. Buanz, S. Gaisford, A.W. Basit, *Fabrication of controlled-release budesonide tablets via desktop (FDM) 3D printing*. International journal of pharmaceutics, **2015**. 496(2): p. 414-420.
[68] Goyanes A., M. Kobayashi, R. Martínez-Pacheco, S. Gaisford, A.W. Basit, *Fused-filament 3D printing of drug products: Microstructure analysis and drug release characteristics of PVA-based caplets*. International Journal of Pharmaceutics, **2016**. 514(1): p. 290-295.
[69] Rafael Auras L.-T.L., Susan E. M. Selke, Hideto Tsuji, *Poly(lactic acid): Synthesis, Structures, Properties, Processing, and Applications*. **2010**: John Wiley & Sons.
[70] Ren J., *Biodegradable Poly(Lactic Acid): Synthesis, Modification, Processing and Applications*. **2010**, U.S.A: Springer.
[71] Alfonso Jimenez M.P., Roxana Ruseckaite, *Poly(lactic acid): Science and Technology Processing, Properties, Additives and Applications*. **2013**: RSC Publishing.
[72] Rodrigues C., L.P.S. Vandenberghe, A.L. Woiciechowski, J. de Oliveira, L.A.J. Letti, C.R. Soccol, *24 - Production and Application of Lactic Acid* in *Current Developments in Biotechnology and Bioengineering*, A. Pandey, S. Negi, and C.R. Soccol Editors. **2017**, Elsevier. p. 543-556.
[73] Maharana T., B. Mohanty, Y.S. Negi, *Melt–solid polycondensation of lactic acid and its biodegradability*. Progress in Polymer Science, **2009**. 34(1): p. 99-124.
[74] Moon S.I., C.W. Lee, M. Miyamoto, Y. Kimura, *Melt polycondensation of L-lactic acid with Sn(II) catalysts activated by various proton acids: A direct manufacturing route to high molecular weight Poly(L-lactic acid)*. Journal of Polymer Science Part A: Polymer Chemistry, **2000**. 38(9): p. 1673-1679.

[75] Mekonnen T., P. Mussone, H. Khalil, D. Bressler, *Progress in bio-based plastics and plasticizing modifications*. Journal of Materials Chemistry A, **2013**. 1(43): p. 13379-13398.

[76] Tokiwa Y., B.P. Calabia, *Biodegradability and biodegradation of poly(lactide)*. Applied Microbiology and Biotechnology, **2006**. 72(2): p. 244-251.

[77] Schliecker G., C. Schmidt, S. Fuchs, T. Kissel, *Characterization of a homologous series of d,l-lactic acid oligomers; a mechanistic study on the degradation kinetics in vitro*. Biomaterials, **2003**. 24(21): p. 3835-3844.

[78] Pranamuda H., Y. Tokiwa, H. Tanaka, *Polylactide degradation by an Amycolatopsis sp*. Applied and Environmental Microbiology, **1997**. 63(4): p. 1637-1640.

[79] Maurus P.B., C.C. Kaeding, *Bioabsorbable implant material review*. Operative Techniques in Sports Medicine, **2004**. 12(3): p. 158-160.

[80] Ramot Y., M. Haim-Zada, A.J. Domb, A. Nyska, *Biocompatibility and safety of PLA and its copolymers*. Advanced Drug Delivery Reviews, **2016**. 107: p. 153-162.

[81] Castro-Aguirre E., F. Iniguez-Franco, H. Samsudin, X. Fang, R. Auras, *Poly(lactic acid)-Mass production, processing, industrial applications, and end of life*. Advanced drug delivery reviews, **2016**. 107: p. 333-366.

[82] Wypych G., *PHB poly(3-hydroxybutyrate)* in *Handbook of Polymers (Second Edition)*, G. Wypych Editor. **2016**, ChemTec Publishing. p. 422-424.

[83] Al-Ashraf A., H. Ramachandran, K.H. Huong, S. Kannusamy, *Microbial-based polyhydroxyalkanoates: upstream and downstream processing*. **2015**: Smithers Rapra Technology Ltd.

[84] Balakrishnan Kunasundari K.S., *Isolation and recovery of microbial polyhydroxyalkanoates*. eXPRESS Polymer Letters, **2011**. 5(7): p. 620-634.

[85] Arikawa H., K. Matsumoto, T. Fujiki, *Polyhydroxyalkanoate production from sucrose by Cupriavidus necator strains harboring csc genes from Escherichia coli*. Applied Microbiology and Biotechnologies, **2017**. 101(20): p. 7497-7507.

[86] Desai V.Y.a.A., *Production of poly-3-hydroxybutyrate from lactose and whey by Methylobacterium sp. ZP24*. Letters in Applied Microbiology, **1998**. 26(6): p. 391-394.

[87] Balakrishna Pillai Aneesh J.K.A., Thulasi Kavitha and Kumarapillai Harikrishnan, *Production of Short Chain Length Polyhydroxyalkanoates by Bacillus megaterium PHB29 from Starch Feed Stock*. International Journal of Current Microbiology and Applied Sciences, **2016**. 5(7): p. 816-823.

[88] S. Obruca P.B., L. Marsalek, and I. Marovaa, *Use of Lignocellulosic Materials for PHA Production*. Chemical and Biochemical Engineering Quarterly, **2015**. 29(2): p. 135–144.

[89] M. Walsh K.O.C., R. Babu, T. Woods, and S. Kennya, *Plant Oils and Products of Their Hydrolysis as Substrates for Polyhydroxyalkanoate SynthesisHydrolysis as Substrates for Polyhydroxyalkanoate Synthesis*. Chemical and Biochemical Engineering Quarterly, **2015**. 29(2): p. 123–133.

[90] Silvana Povolo M.G.R., Federico Fontana, Marina Basaglia, Sergio Casella, *Production of Polyhydroxyalkanoates from Fatty Wastes*. Journal of Polymers and the Environment, **2012**. 20: p. 944–949.

[91] Jiang G., D.J. Hill, M. Kowalczuk, B. Johnston, G. Adamus, V. Irorere, I. Radecka, *Carbon Sources for Polyhydroxyalkanoates and an Integrated Biorefinery*. International Journal of Molecular Sciences, **2016**. 17(7).

[92] Koller M., H. Niebelschütz, G. Braunegg, *Strategies for recovery and purification of poly[(R)-3-hydroxyalkanoates] (PHA) biopolyesters from surrounding biomass*. Engineering in Life Sciences, **2013**. 13(6): p. 549-562.

[93] Ramsay J.A., E. Berger, R. Voyer, C. Chavarie, B.A. Ramsay, *Extraction of poly-3-hydroxybutyrate using chlorinated solvents*. Biotechnology Techniques, **1994**. 8(8): p. 589-594.

[94] Hampson J.W., R.D. Ashby, *Extraction of lipid-grown bacterial cells by supercritical fluid and organic solvent to obtain pure medium chain-length polyhydroxyalkanoates*. Journal of the American Oil Chemists' Society, **1999**. 76(11): p. 1371-1374.

[95] Hahn S.K., Y.K. Chang, B.S. Kim, K.M. Lee, H.N. Chang, *The recovery of poly(3-hydroxybutyrate) by using dispersions of sodium hypochlorite solution and chloroform*. Biotechnology Techniques, **1993**. 7(3): p. 209-212.

[96] Steinbüchel A., H.E. Valentin, *Diversity of bacterial polyhydroxyalkanoic acids*. FEMS Microbiology Letters, **1995**. 128(3): p. 219-228.

[97] E. Bugnicourt P.C., A. Lazzeri, V. Alvarez, *Polyhydroxyalkanoate (PHA): Review of synthesis, characteristics, processing and potential applications in packaging*. eXPRESS Polymer Letters, **2014**. 8(11): p. 791–808.

[98] Volova T.G., Boyandin, A. N., Vasiliev, A. D., Karpov, V. A., Prudnikova, S. V., Mishukova, O. V., Boyarskikh, U. A., Filipenko, M. L., Rudnev, V. P., Bá Xuân, Bùi, Việt Dũng, Vũ, Gitelson, I. I., *Biodegradation of polyhydroxyalkanoates (PHAs) in tropical coastal waters and identification of PHA-degrading bacteria*. Polymer Degradation and Stability, **2010**. 95(12): p. 2350-2359.

[99] Anatoly N. Boyandin S.V.P., Valery A. Karpov, Vladimir N. Ivonin, Ngọc Lanh Đỗ, Thị Hoài Nguyễn, Thị Mỹ Hiệp Lê, Nikolay L. Filichev, Alexander L. Levin, Maxim L. Filipenko, Tatiana G. Volova, Iosif I. Gitelson, *Microbial degradation of polyhydroxyalkanoates in tropical soils*. International Biodeterioration & Biodegradation, **2013**. 83: p. 77-84.

[100] Keiji Numata H.A., Tadahisa Iwata, *Biodegradability of Poly(hydroxyalkanoate) Materials*. Materials, **2009**. 2(3): p. 1104-1126.
[101] Milan Matavulj N.S., Hans Peter Molitoris, *Biodegradation of polyhydroxyalkanoate-based plastic (BIOPOL) under different environmental conditions I. Weightloss of substrate*. Hoppea - Denkschriften der Regensburgischen Botanischen Gesellschaft, **2000**. 61: p. 735-749.
[102] Shishatskaya E.I., T.G. Volova, A.P. Puzyr, O.A. Mogilnaya, S.N. Efremov, *Tissue response to the implantation of biodegradable polyhydroxyalkanoate sutures*. Journal of Materials Science: Materials in Medicine, **2004**. 15(6): p. 719-728.
[103] Volova T.G., A.A. Shumilova, E.D. Nikolaeva, A.K. Kirichenko, E.I. Shishatskaya, *Biotechnological wound dressings based on bacterial cellulose and degradable copolymer P(3HB/4HB)*. International Journal of Biological Macromolecules, **2019**.
[104] Iftikhar Ali N.J., *Polyhydroxyalkanoates: Current applications in the medical field*. Frontiers in Biology, **2016**. 11(1).
[105] Shishatskaya E.I., E.D. Nikolaeva, O.N. Vinogradova, T.G. Volova, *Experimental wound dressings of degradable PHA for skin defect repair*. Journal of Materials Science: Materials in Medicine, **2016**. 27(11): p. 165.
[106] *Tepha Medical Devices, www.tepha.com*. Available from: https://www.tepha.com/.
[107] Roy I., V.P. M, *Polyhydroxyalkanoate (PHA) Based Blends, Composites and Nanocomposites*. **2015**: RCS Publishing.
[108] Bucci D.Z., L.B.B. Tavares, I. Sell, *PHB packaging for the storage of food products*. Polymer Testing, **2005**. 24(5): p. 564-571.
[109] S. V. PrudnikovaA. N. Boyandin G.S.K.J.S., *Degradable Polyhydroxyalkanoates as Herbicide Carriers*. Journal of Polymers and the Environment, **2012**. 21(3): p. 675-682.
[110] *Mirel Bioplastics*. Available from: http://www.mirelplastics.com/.
[111] *plasticker.de*. Available from: http://plasticker.de/.
[112] David Roland-Holst R.T., Sam Heft-Neal, Bijan Bayrami, *Bioplastics in California Economic Assessment of Market Conditions for PHA/PHB Bioplastics Produced from Waste Methane*. **2013**.
[113] J. Choi S.Y.L., *Factors affecting the economics of polyhydroxyalkanoate production by bacterial fermentation*. Applied Microbiology and Biotechnology, **1999**. 51(1): p. 13-21.
[114] Koller M., G. Braunegg, *Advanced approaches to produce polyhydroxyalkanoate (PHA) biopolyesters in a sustainable and economic fashion*. Journal of Biotechnology, **2018**. 280(5): p. 89.
[115] Klemm D., B. Heublein, H.-P. Fink, A. Bohn, *Cellulose: Fascinating Biopolymer and Sustainable Raw Material*. Angewandte Chemie International Edition, **2005**. 44(22): p. 3358-3393.

[116] Kamide K., *Cellulose and Cellulose Derivatives*. **2005**: Elsevier.
[117] Bhattacharya D., L.T. Germinario, W.T. Winter, *Isolation, preparation and characterization of cellulose microfibers obtained from bagasse*. Carbohydrate Polymers, **2008**. 73(3): p. 371-377.
[118] Börjesson M., G. Westman, *Crystalline Nanocellulose — Preparation, Modification, and Properties* in *Cellulose, Fundamental Aspects and Current Trends*, M. Poletto Editor. **2015**, IntechOpen.
[119] Alberts B J.A., Lewis J, *Molecular Biology of the Cell*. **2002**: Garland Science.
[120] Page D.H., F. El-Hosseiny, *Mechanical properties of single wood pulp fibres*. Journal of Pulp and Paper Science, **1983**. 9(4): p. 99-100.
[121] Djafari Petroudy S.R., *3 - Physical and mechanical properties of natural fibers* in *Advanced High Strength Natural Fibre Composites in Construction*, M. Fan and F. Fu Editors. **2017**, Woodhead Publishing. p. 59-83.
[122] Nechyporchuk O., M.N. Belgacem, J. Bras, *Production of cellulose nanofibrils: A review of recent advances*. Industrial Crops and Products, **2016**. 93: p. 2-25.
[123] Boldizar A., C. Klason, J. Kubát, P. Näslund, P. Saha, *Prehydrolyzed Cellulose as Reinforcing Filler for Thermoplastics*. International Journal of Polymeric Materials and Polymeric Biomaterials, **1987**. 11(4): p. 229-262.
[124] Nechyporchuk O., N. Belgacem, F. Pignon, *Current Progress in Rheology of Cellulose Nanofibril Suspensions*. Biomacromolecules, **2016**. 17(7): p. 2311–2320.
[125] Rånby B.G., *Fibrous macromolecular systems. Cellulose and muscle. The colloidal properties of cellulose micelles*. Discussions of the Faraday Society, **1951**. 11: p. 158-164.
[126] Brinchi L., F. Cotana, E. Fortunati, J.M. Kenny, *Production of nanocrystalline cellulose from lignocellulosic biomass: technology and applications*. Carbohydrate polymers, **2013**. 94(1): p. 154-169.
[127] Morais J.P.S., M.d.F. Rosa, M.d.s.M. de Souza Filho, L.D. Nascimento, D.M. do Nascimento, A.R. Cassales, *Extraction and characterization of nanocellulose structures from raw cotton linter*. Carbohydrate Polymers, **2013**. 91(1): p. 229-235.
[128] Roman M., W.T. Winter, *Effect of Sulfate Groups from Sulfuric Acid Hydrolysis on the Thermal Degradation Behavior of Bacterial Cellulose*. Biomacromolecules, **2004**. 5(5): p. 1671-1677.
[129] Phanthong P., P. Reubroycharoen, X. Hao, G. Xu, A. Abudula, G. Guan, *Nanocellulose: Extraction and application*. Carbon Resources Conversion, **2018**. 1(1): p. 32-43.
[130] Dufresne A., *Nanocellulose: a new ageless bionanomaterial*. Materials Today, **2013**. 16(6): p. 220-227.

[131] Standau T., C. Zhao, S. Murillo Castellón, C. Bonten, V. Altstädt, *Chemical Modification and Foam Processing of Polylactide (PLA)*. Polymers, **2019**. 11(2): p. 306.

[132] Bondeson D., A. Mathew, K. Oksman, *Optimization of the isolation of nanocrystals from microcrystalline cellulose by acid hydrolysis*. Cellulose, **2006**. 13(2): p. 171-180.

[133] Adriana N. Frone D.M.P., Dan Donescu, Catalin I. Spataru,, R.T. Constantin Radovici, and Raluca Somoghi, *Preparation and characterization of PVA composites with cellulose nanofibers obtained by ultrasonication*. BioResources, **2011**. 6(1): p. 487-512.

[134] Chen W., H. Yu, Y. Liu, P. Chen, M. Zhang, Y. Hai, *Individualization of cellulose nanofibers from wood using high-intensity ultrasonication combined with chemical pretreatments*. Carbohydrate Polymers, **2011**. 83(4): p. 1804-1811.

[135] Cheng Q., S. Wang, T.G. Rials, *Poly(vinyl alcohol) nanocomposites reinforced with cellulose fibrils isolated by high intensity ultrasonication*. Composites Part A: Applied Science and Manufacturing, **2009**. 40(2): p. 218-224.

[136] Hu Z., R. Zhai, J. Li, Y. Zhang, J. Lin, *Preparation and Characterization of Nanofibrillated Cellulose from Bamboo Fiber via Ultrasonication Assisted by Repulsive Effect*. International Journal of Polymer Science, **2017**. 2017: p. 1-9.

[137] Xiao S., R. Gao, L. Gao, J. Li, *Poly(vinyl alcohol) films reinforced with nanofibrillated cellulose (NFC) isolated from corn husk by high intensity ultrasonication*. Carbohydrate polymers, **2016**. 136: p. 1027-1034.

[138] Oksman K., Y. Aitomäki, A.P. Mathew, G. Siqueira, Q. Zhou, S. Butylina, S. Tanpichai, X. Zhou, S. Hooshmand, *Review of the recent developments in cellulose nanocomposite processing*. Composites Part A: Applied Science and Manufacturing, **2016**. 83: p. 2-18.

[139] Roman M., W.T. Winter, *Effect of sulfate groups from sulfuric acid hydrolysis on the thermal degradation behavior of bacterial cellulose*. Biomacromolecules, **2004**. 5(5): p. 1671-1677.

[140] Bouchard J.D.a.R., *Polyvinyl alcohol*. Manufacture of Plastics, ed by W.M. Smith. Reinhold, New York and London, **1964**.

[141] Mukherjee T., M. Sani, N. Kao, R.K. Gupta, N. Quazi, S. Bhattacharya, *Improved dispersion of cellulose microcrystals in polylactic acid (PLA) based composites applying surface acetylation*. Chemical Engineering Science, **2013**. 101: p. 655-662.

[142] Salim Y., C.H. Chan, K. Sudesh, S.N. Gan, *Isothermal crystallisation kinetics of microbial poly(3-hydroxybutyrateco- 3-hydroxyhexanoate)*. International Journal of Pharmacy and Pharmaceutical Sciences, **2014**. 6(3-8).

[143] Kolařík J., A. Pegoretti, *Proposal of the Boltzmann-like superposition principle for nonlinear tensile creep of thermoplastics*. Polymer Testing, **2008**. 27(5): p. 596-606.
[144] Dorigato A., A. Pegoretti, *Biodegradable single-polymer composites from polyvinyl alcohol*. Colloid and Polymer Science, **2011**. 290(4): p. 359-370.
[145] Jonathan G., A. Karim, *3D printing in pharmaceutics: A new tool for designing customized drug delivery systems*. Int J Pharm, **2016**. 499(1-2): p. 376-394.
[146] Mandal A., D. Chakrabarty, *Characterization of nanocellulose reinforced semi-interpenetrating polymer network of poly(vinyl alcohol) & polyacrylamide composite films*. Carbohydr Polym, **2015**. 134: p. 240-250.
[147] Lu Y., M.C. Cueva, E. Lara-Curzio, S. Ozcan, *Improved mechanical properties of polylactide nanocomposites-reinforced with cellulose nanofibrils through interfacial engineering via amine-functionalization*. Carbohydr Polym, **2015**. 131: p. 208-217.
[148] Pereira A.L., D.M. do Nascimento, S. Souza Filho Mde, J.P. Morais, N.F. Vasconcelos, J.P. Feitosa, A.I. Brigida, F. Rosa Mde, *Improvement of polyvinyl alcohol properties by adding nanocrystalline cellulose isolated from banana pseudostems*. Carbohydr Polym, **2014**. 112: p. 165-172.
[149] Roohani M., Y. Habibi, N.M. Belgacem, G. Ebrahim, A.N. Karimi, A. Dufresne, *Cellulose whiskers reinforced polyvinyl alcohol copolymers nanocomposites*. European Polymer Journal, **2008**. 44(8): p. 2489-2498.
[150] Sun J., J. Shen, S. Chen, M. Cooper, H. Fu, D. Wu, Z. Yang, *Nanofiller Reinforced Biodegradable PLA/PHA Composites: Current Status and Future Trends*. Polymers, **2018**. 10(5): p. 505.
[151] Swaroop C., M. Shukla, *Nano-magnesium oxide reinforced polylactic acid biofilms for food packaging applications*. International Journal of Biological Macromolecules, **2018**. 113: p. 729-736.
[152] Oksman K., M. Skrifvars, J.F. Selin, *Natural fibres as reinforcement in polylactic acid (PLA) composites*. Composites Science and Technology, **2003**. 63(9): p. 1317-1324.
[153] Mathew A.P., K. Oksman, M. Sain, *Mechanical properties of biodegradable composites from poly lactic acid (PLA) and microcrystalline cellulose (MCC)*. Journal of Applied Polymer Science, **2005**. 97(5): p. 2014-2025.
[154] Rzayev Z., *Graft Copolymers of Maleic Anhydride and Its Isostructural Analogues: High Performance Engineering Materials*. International Review of Chemical Engineering, **2011**. 3(2): p. 153-215.
[155] Hwang S.W., S.B. Lee, C.K. Lee, J.Y. Lee, J.K. Shim, S.E.M. Selke, H. Soto-Valdez, L. Matuana, M. Rubino, R. Auras, *Grafting of maleic anhydride on poly(L-lactic acid). Effects on physical and mechanical properties*. Polymer Testing, **2012**. 31(2): p. 333-344.

[156] Issaadi K., A. Habi, Y. Grohens, I. Pillin, *Effect of the montmorillonite intercalant and anhydride maleic grafting on polylactic acid structure and properties*. Applied Clay Science, **2015**. 107: p. 62-69.

[157] Detyothin S., S.E.M. Selke, R. Narayan, M. Rubino, R. Auras, *Reactive functionalization of poly(lactic acid), PLA: Effects of the reactive modifier, initiator and processing conditions on the final grafted maleic anhydride content and molecular weight of PLA*. Polymer Degradation and Stability, **2013**. 98(12): p. 2697-2708.

[158] Ma P., L. Jiang, T. Ye, W. Dong, M. Chen, *Melt Free-Radical Grafting of Maleic Anhydride onto Biodegradable Poly(lactic acid) by Using Styrene as A Comonomer*. Polymers, **2014**. 6(5): p. 1528-1543.

[159] Kaynak C., Y. Meyva, *Use of maleic anhydride compatibilization to improve toughness and other properties of polylactide blended with thermoplastic elastomers*. Polymers for Advanced Technologies, **2014**. 25(12): p. 1622-1632.

[160] Petersson L., K. Oksman, A.P. Mathew, *Using maleic anhydride grafted poly(lactic acid) as a compatibilizer in poly(lactic acid)/layered-silicate nanocomposites*. Journal of Applied Polymer Science, **2006**. 102(2): p. 1852-1862.

[161] Tsou C.-H., W.-S. Hung, C.-S. Wu, J.-C. Chen, C.-Y. Huang, S.-H. Chiu, C.-Y. Tsou, W.-H. Yao, S.-M. Lin, C.-K. Chu, C.-C. Hu, K.-R. Lee, M.-C. Suen, *New Composition of Maleic-Anhydride-Grafted Poly(Lactic Acid)/Rice Husk with Methylenediphenyl Diisocyanate*. Materials Science, **2014**. 20(4).

[162] Zhu R., H. Liu, J. Zhang, *Compatibilizing Effects of Maleated Poly(lactic acid) (PLA) on Properties of PLA/Soy Protein Composites*. Industrial & Engineering Chemistry Research, **2012**. 51(22): p. 7786-7792.

[163] Nyambo C., A.K. Mohanty, M. Misra, *Effect of Maleated Compatibilizer on Performance of PLA/Wheat Straw-Based Green Composites*. Macromolecular Materials and Engineering, **2011**. 296(8): p. 710-718.

[164] Zhang J.F., X. Sun, *Physical characterization of coupled poly(lactic acid)/starch/maleic anhydride blends plasticized by acetyl triethyl citrate*. Macromolecular bioscience, **2004**. 4(11): p. 1053-1060.

[165] Zhang J.-F., X. Sun, *Mechanical Properties of Poly(lactic acid)/Starch Composites Compatibilized by Maleic Anhydride*. Biomacromolecules, **2004**. 5(4): p. 1446-1451.

[166] Yu T., N. Jiang, Y. Li, *Study on short ramie fiber/poly(lactic acid) composites compatibilized by maleic anhydride*. Composites Part A: Applied Science and Manufacturing, **2014**. 64: p. 139-146.

[167] Zhou L., H. He, M.-c. Li, S. Huang, C. Mei, Q. Wu, *Enhancing mechanical properties of poly(lactic acid) through its in-situ crosslinking with maleic anhydride-modified cellulose nanocrystals from cottonseed hulls*. Industrial Crops and Products, **2018**. 112: p. 449-459.

[168] Kulinski Z., E. Piorkowska, *Crystallization, structure and properties of plasticized poly(l-lactide)*. Polymer, **2005**. 46(23): p. 10290-10300.
[169] Barczewski M., O. Mysiukiewicz, *Rheological and Processing Properties of Poly(lactic acid) Composites Filled with Ground Chestnut Shell*. Polymer Korea, **2018**. 42: p. 267-274.
[170] Yamoum C., R. Magaraphan, *Effect of Carboxymethylcellulose on Plasticized Polylactide*. Advanced Materials Research, **2013**. 658: p. 19-24.
[171] Shenoy A.V., S. Chattopadhyay, V.M. Nadkarni, *From melt flow index to rheogram*. Rheologica Acta, **1983**. 22(1): p. 90-101.
[172] Brian N.T., *A review of melt extrusion additive manufacturing processes: I. Process design and modeling*. Rapid Prototyping Journal, **2014**. 20(3): p. 192-204.
[173] Cataldi A, L. Berglund, F. Deflorian, A. Pegoretti, *A comparison between micro- and nanocellulose filled composite adhesives for oil paintings restoration*. Nanocomposites, **2015**. 18(4): p. 1-9.
[174] Cataldi A., C. Esposito Corcione, M. Frigione, A. Pegoretti, *Photocurable resin/nanocellulose composite coatings for wood protection*. Progress in Organic Coatings, **2017**. 106: p. 128-136.
[175] Lizundia E., E. Fortunati, F. Dominici, J.L. Vilas, L.M. Leon, I. Armentano, L. Torre, J.M. Kenny, *PLLA-grafted cellulose nanocrystals: Role of the CNC content and grafting on the PLA bionanocomposite film properties*. Carbohydr Polym, **2016**. 142: p. 105-113.
[176] Arrieta M.P., E. Fortunati, F. Dominici, J. Lopez, J.M. Kenny, *Bionanocomposite films based on plasticized PLA-PHB/cellulose nanocrystal blends*. Carbohydr Polym, **2015**. 121: p. 265-275.
[177] Wang T., L.T. Drzal, *Cellulose-Nanofiber-Reinforced Poly(lactic acid) Composites Prepared by a Water-Based Approach*. ACS Applied Materials & Interfaces, **2012**. 4(10): p. 5079-5085.
[178] Khoo R.Z., H. Ismail, W.S. Chow, *Thermal and Morphological Properties of Poly (Lactic Acid)/Nanocellulose Nanocomposites*. Procedia Chemistry, **2016**. 19: p. 788-794.
[179] Du Y., T. Wu, N. Yan, M.T. Kortschot, R. Farnood, *Fabrication and characterization of fully biodegradable natural fiber-reinforced poly(lactic acid) composites*. Composites Part B: Engineering, **2014**. 56: p. 717-723.
[180] Viikna A., A. Krumme, E. Tarasova, D. Šumigin, *Influence of cellulose content on thermal properties of poly(lactic) acid/cellulose and low-density polyethylene/cellulose composites*. Proceedings of the Estonian Academy of Sciences, **2012**. 61(3): p. 237.
[181] Frone A.N., S. Berlioz, J.F. Chailan, D.M. Panaitescu, *Morphology and thermal properties of PLA-cellulose nanofibers composites*. Carbohydrate polymers, **2013**. 91(1): p. 377-384.

[182] Cataldi A., A. Dorigato, F. Deflorian, A. Pegoretti, *Thermo-mechanical properties of innovative microcrystalline cellulose filled composites for art protection and restoration*. Journal of Materials Science, **2013**. 49(5): p. 2035-2044.
[183] Cataldi A., A. Dorigato, F. Deflorian, A. Pegoretti, *Effect of the water sorption on the mechanical response of microcrystalline cellulose-based composites for art protection and restoration*. Journal of Applied Polymer Science, **2014**. 131(18).
[184] Gupta A., W. Simmons, G.T. Schueneman, D. Hylton, E.A. Mintz, *Rheological and Thermo-Mechanical Properties of Poly(lactic acid)/Lignin-Coated Cellulose Nanocrystal Composites*. ACS Sustainable Chemistry & Engineering, **2017**. 5(2): p. 1711-1720.
[185] Mukherjee T., N. Kao, R.K. Gupta, N. Quazi, S. Bhattacharya, *Evaluating the state of dispersion on cellulosic biopolymer by rheology*. Journal of Applied Polymer Science, **2016**. 133(12).
[186] Georgiopoulos P., E. Kontou, G. Georgousis, *Effect of silane treatment loading on the flexural properties of PLA/flax unidirectional composites*. Composites Communications, **2018**. 10: p. 6-10.
[187] Georgiopoulos P., A. Christopoulos, S. Koutsoumpis, E. Kontou, *The effect of surface treatment on the performance of flax/biodegradable composites*. Composites Part B: Engineering, **2016**. 106: p. 88-98.
[188] Rubio-López A., J. Artero-Guerrero, J. Pernas-Sánchez, C. Santiuste, *Compression after impact of flax/PLA biodegradable composites*. Polymer Testing, **2017**. 59: p. 127-135.
[189] Bax B., J. Müssig, *Impact and tensile properties of PLA/Cordenka and PLA/flax composites*. Composites Science and Technology, **2008**. 68(7-8): p. 1601-1607.
[190] Saba N., M.T. Paridah, M. Jawaid, *Mechanical properties of kenaf fibre reinforced polymer composite: A review*. Construction and Building Materials, **2015**. 76: p. 87-96.
[191] Nishino T., K. Hirao, M. Kotera, K. Nakamae, H. Inagaki, *Kenaf reinforced biodegradable composite*. Composites Science and Technology, **2003**. 63(9): p. 1281-1286.
[192] Akil H.M., M.F. Omar, A.A.M. Mazuki, S. Safiee, Z.A.M. Ishak, A. Abu Bakar, *Kenaf fiber reinforced composites: A review*. Materials & Design, **2011**. 32(8-9): p. 4107-4121.
[193] Assis F.S.d., A.C. Pereira, F.d.C.G. Filho, É.P. Lima, S.N. Monteiro, R.P. Weber, *Performance of jute non-woven mat reinforced polyester matrix composite in multilayered armor*. Journal of Materials Research and Technology, **2018**. 7(4): p. 535-540.
[194] Basak R., P.L. Choudhury, K.M. Pandey, *Effect of Temperature Variation on Surface Treatment of Short Jute Fiber-Reinforced Epoxy Composites*. Materials Today: Proceedings, **2018**. 5(1): p. 1271-1277.

[195] Lautenschläger M.I., L. Mayer, J. Gebauer, K.A. Weidenmann, F. Henning, P. Elsner, *Comparison of filler-dependent mechanical properties of jute fiber reinforced sheet and bulk molding compound*. Composite Structures, **2018**. 203: p. 960-967.

[196] Durante M., A. Formisano, L. Boccarusso, A. Langella, L. Carrino, *Creep behaviour of polylactic acid reinforced by woven hemp fabric*. Composites Part B: Engineering, **2017**. 124: p. 16-22.

[197] Ibrahim H., M. Farag, H. Megahed, S. Mehanny, *Characteristics of starch-based biodegradable composites reinforced with date palm and flax fibers*. Carbohydr Polym, **2014**. 101: p. 11-19.

[198] Väisänen T., O. Das, L. Tomppo, *A review on new bio-based constituents for natural fiber-polymer composites*. Journal of Cleaner Production, **2017**. 149: p. 582-596.

[199] Cherian B.M., A.L. Leão, S.F. de Souza, S. Thomas, L.A. Pothan, M. Kottaisamy, *Isolation of nanocellulose from pineapple leaf fibres by steam explosion*. Carbohydrate Polymers, **2010**. 81(3): p. 720-725.

[200] Dubey S., R.K. Sharma, P. Agarwal, J. Singh, N. Sinha, R.P. Singh, *From rotten grapes to industrial exploitation: Komagataeibacter europaeus SGP37, a micro-factory for macroscale production of bacterial nanocellulose*. International journal of biological macromolecules, **2017**. 96: p. 52-60.

[201] Salajková M., L.A. Berglund, Q. Zhou, *Hydrophobic cellulose nanocrystals modified with quaternary ammonium salts*. Journal of Materials Chemistry, **2012**. 22(37): p. 19798.

[202] Fortunati E., F. Luzi, D. Puglia, R. Petrucci, J.M. Kenny, L. Torre, *Processing of PLA nanocomposites with cellulose nanocrystals extracted from Posidonia oceanica waste: Innovative reuse of coastal plant*. Industrial Crops and Products, **2015**. 67: p. 439-447.

[203] Yang H.Z., L.L. Feng, C.Y. Wang, W. Zhao, X.G. Li, *Confinement effect of SiO2 framework on phase change of PEG in shape-stabilized PEG/SiO2 composites*. European Polymer Journal, **2012**. 48(4): p. 803-810.

[204] Siracusa V., P. Rocculi, S. Romani, M.D. Rosa, *Biodegradable polymers for food packaging: a review*. Trends in Food Science & Technology, **2008**. 19(12): p. 634-643.

[205] Sanchez-Garcia M.D., E. Gimenez, J.M. Lagaron, *Morphology and barrier properties of solvent cast composites of thermoplastic biopolymers and purified cellulose fibers*. Carbohydrate Polymers, **2008**. 71(2): p. 235-244.

[206] Khan A., R.A. Khan, S. Salmieri, C. Le Tien, B. Riedl, J. Bouchard, G. Chauve, V. Tan, M.R. Kamal, M. Lacroix, *Mechanical and barrier properties of nanocrystalline cellulose reinforced chitosan based nanocomposite films*. Carbohydr Polym, **2012**. 90(4): p. 1601-1608.

[207] Lavoine N., I. Desloges, A. Dufresne, J. Bras, *Microfibrillated cellulose - its barrier properties and applications in cellulosic materials: a review*. Carbohydr Polym, **2012**. 90(2): p. 735-764.
[208] Espino-Pérez E., J. Bras, V. Ducruet, A. Guinault, A. Dufresne, S. Domenek, *Influence of chemical surface modification of cellulose nanowhiskers on thermal, mechanical, and barrier properties of poly(lactide) based bionanocomposites*. European Polymer Journal, **2013**. 49(10): p. 3144-3154.
[209] Fortunati E., M. Peltzer, I. Armentano, L. Torre, A. Jimenez, J.M. Kenny, *Effects of modified cellulose nanocrystals on the barrier and migration properties of PLA nano-biocomposites*. Carbohydrate polymers, **2012**. 90(2): p. 948-956.
[210] Checchetto R., D. Rigotti, A. Pegoretti, A. Miotello, *Chloroform desorption from poly(lactic acid) nanocomposites: a thermal desorption spectroscopy study*. Pure and Applied Chemistry, **2019**. 0(0).
[211] Silverstein R., C. Bassler, *Spectrometric identification of organic compounds*. Magnetic Resonance in Chemistry, **1992**. 30(4): p. 364-364.
[212] Fambri L., A. Penati, J. Kolarik, *Modification of polycarbonate with miscible polyurethane elastomers*. Polymer, **1997**. 38(4): p. 835-843.
[213] Spinella S., G. Lo Re, B. Liu, J. Dorgan, Y. Habibi, P. Leclère, J.-M. Raquez, P. Dubois, R.A. Gross, *Polylactide/cellulose nanocrystal nanocomposites: Efficient routes for nanofiber modification and effects of nanofiber chemistry on PLA reinforcement*. Polymer, **2015**. 65: p. 9-17.
[214] Johari A.P., S.K. Kurmvanshi, S. Mohanty, S.K. Nayak, *Influence of surface modified cellulose microfibrils on the improved mechanical properties of poly (lactic acid)*. International journal of biological macromolecules, **2016**. 84: p. 329-339.
[215] Kelnar I., J. Kratochvíl, L. Kaprálková, A. Zhigunov, Z. Padovec, M. Růžička, M. Nevoralová, *Antagonistic effects on mechanical properties of microfibrillar composites with dual reinforcement: Explanation by FEA model of soft interface*. Journal of Applied Polymer Science, **2017**. 134(20).
[216] Suryanegara L., A. Nakagaito, H. Yano, *The effect of crystallization of PLA on the thermal and mechanical properties of microfibrillated cellulose-reinforced PLA composites*. Composites Science and Technology, **2009**. 69(7-8): p. 1187–1192.
[217] Checchetto R., P. Bettotti, R.S. Brusa, G. Carotenuto, W. Egger, C. Hugenschmidt, A. Miotello, *Anomalous molecular infiltration in graphene laminates*. Physical Chemistry Chemical Physics, **2018**. 20(38): p. 24671-24680.
[218] Bhatia A., R.K. Gupta, S.N. Bhattacharya, H.J. Choi, *Analysis of Gas Permeability Characteristics of Poly(Lactic Acid)/Poly(Butylene Succinate) Nanocomposites*. Journal of Nanomaterials, **2012**. 2012.

[219] Roilo D., C.A. Maestri, M. Scarpa, P. Bettotti, W. Egger, T. Koschine, R.S. Brusa, R. Checchetto, *Cellulose Nanofibrils Films: Molecular Diffusion through Elongated Sub-Nano Cavities*. The Journal of Physical Chemistry C, **2017**. 121(28): p. 15437-15447.
[220] Yarwood J., *The Physical Basis of Ultrahigh Vacuum*. Physics Bulletin, **1969**. 20(9): p. 383.
[221] Merkel T., I. Pinnau, R. Prabhakar, B. Freeman, *Gas and Vapor Transport Properties of Perfluoropolymers* in *Materials Science of Membranes for Gas and Vapor Separation*, Y. Yampolskii, I. Pinnau, and B. Freeman Editors. **2006**, John Wiley & Sons, Ltd. p. 251-270.
[222] Crank J., *The mathematics of diffusion*. **1986**: Oxford Science Publications.
[223] Nielsen L.E., *Models for the Permeability of Filled Polymer Systems AU*. Journal of Macromolecular Science: Part A - Chemistry, **1967**. 1(5): p. 929-942.
[224] Bharadwaj R.K., *Modeling the Barrier Properties of Polymer-Layered Silicate Nanocomposites*. Macromolecules, **2001**. 34(26): p. 9189-9192.
[225] Aroon M.A., A.F. Ismail, T. Matsuura, M.M. Montazer-Rahmati, *Performance studies of mixed matrix membranes for gas separation: A review*. Separation and Purification Technology, **2010**. 75(3): p. 229-242.
[226] Pal R., *Permeation models for mixed matrix membranes*. Journal of colloid and interface science, **2008**. 317(1): p. 191-198.
[227] Moore T.T., W.J. Koros, *Non-ideal effects in organic–inorganic materials for gas separation membranes*. Journal of Molecular Structure, **2005**. 739(1): p. 87-98.
[228] Rezakazemi M., A. Ebadi Amooghin, M. Mehdi Montazer-Rahmati, A. Ismail, T. Matsuura, *State-of-the-art membrane based CO2 separation using mixed matrix membranes (MMMs): An overview on current status and future directions*. Progress in Polymer Science, **2014**. 39(5): p. 817–861.
[229] Bioplastic E.; Available from: https://www.european-bioplastics.org/market/.
[230] Niaounakis M. **2013**, Oxford UK: William Andrew Publishing.
[231] Yeo J.C.C., J.K. Muiruri, W. Thitsartarn, Z. Li, C. He, *Recent advances in the development of biodegradable PHB-based toughening materials: Approaches, advantages and applications*. Materials Science and Engineering: C, **2017**.
[232] Philip S., T. Keshavarz, I. Roy, *Polyhydroxyalkanoates: biodegradable polymers with a range of applications*. Journal of Chemical Technology & Biotechnology, **2007**. 82(3): p. 233-247.
[233] Chen G.Q., *A microbial polyhydroxyalkanoates (PHA) based bio- and materials industry*. Chemical Society Reviews, **2009**. 38(8): p. 2434-2446.

[234] Grassie N., E.J. Murray, P.A. Holmes, *The thermal degradation of poly(-(d)-β-hydroxybutyric acid): Part 3—The reaction mechanism*. Polymer Degradation and Stability, **1984**. 6(3): p. 127-134.
[235] Ariffin H., H. Nishida, Y. Shirai, M.A. Hassan, *Determination of multiple thermal degradation mechanisms of poly(3-hydroxybutyrate)*. Polymer Degradation and Stability, **2008**. 93(8): p. 1433-1439.
[236] Tripathi L., L.-P. Wu, J. Chen, G.-Q. Chen, *Synthesis of Diblock copolymer poly-3-hydroxybutyrate -block-poly-3-hydroxyhexanoate [PHB-b-PHHx] by a β-oxidation weakened Pseudomonas putida KT2442*. Microbial Cell Factories, **2012**. 11(1): p. 44.
[237] Tănase E.E., M.E. Popa, M. Râpă, O. Popa, *PHB/Cellulose Fibers Based Materials: Physical, Mechanical and Barrier Properties*. Agriculture and Agricultural Science Procedia, **2015**. 6: p. 608-615.
[238] Yu H.-y., Z.-y. Qin, Z. Zhou, *Cellulose nanocrystals as green fillers to improve crystallization and hydrophilic property of poly(3-hydroxybutyrate-co-3-hydroxyvalerate)*. Progress in Natural Science: Materials International, **2011**. 21(6): p. 478-484.
[239] Singh S., A.K. Mohanty, T. Sugie, Y. Takai, H. Hamada, *Renewable resource based biocomposites from natural fiber and polyhydroxybutyrate-co-valerate (PHBV) bioplastic*. Composites Part A: Applied Science and Manufacturing, **2008**. 39(5): p. 875-886.
[240] Rigotti D., A. Dorigato, A. Pegoretti, *3D printable thermoplastic polyurethane blends with thermal energy storage/release capabilities*. Materials Today Communications, **2018**. 15: p. 228-235.
[241] Bhandari S., R. Lopez-Anido, *Finite element analysis of thermoplastic polymer extrusion 3D printed material for mechanical property prediction*. Additive Manufacturing, **2018**. 22: p. 187-196.